



저작자표시-비영리-변경금지 2.0 대한민국

이용자는 아래의 조건을 따르는 경우에 한하여 자유롭게

- 이 저작물을 복제, 배포, 전송, 전시, 공연 및 방송할 수 있습니다.

다음과 같은 조건을 따라야 합니다:



저작자표시. 귀하는 원저작자를 표시하여야 합니다.



비영리. 귀하는 이 저작물을 영리 목적으로 이용할 수 없습니다.



변경금지. 귀하는 이 저작물을 개작, 변형 또는 가공할 수 없습니다.

- 귀하는, 이 저작물의 재이용이나 배포의 경우, 이 저작물에 적용된 이용허락조건을 명확하게 나타내어야 합니다.
- 저작권자로부터 별도의 허가를 받으면 이러한 조건들은 적용되지 않습니다.

저작권법에 따른 이용자의 권리는 위의 내용에 의하여 영향을 받지 않습니다.

이것은 [이용허락규약\(Legal Code\)](#)을 이해하기 쉽게 요약한 것입니다.

[Disclaimer](#)

공학박사학위논문

비등방성 메타물질을 이용한 탄성과
원추 굴절

Conical Refraction of Elastic Waves by Engineered
Anisotropic Metamaterials

2017년 2월

서울대학교 대학원
기계항공공학부
안영관

ABSTRACT

Conical Refraction of Elastic Waves by Engineered Anisotropic Metamaterials

Young Kwan Ahn

School of Mechanical and Aerospace Engineering

The Graduate School

Seoul National University

Conical refraction is a phenomenon that occurs in biaxial anisotropic medium and can be used to adjust their unique wave propagation direction. The concept of conical refraction has been useful in the areas of electromagnetics and optics. However, in the ultrasonics field, vibrational wave propagation in elastic structures using conical refraction needs further research for understanding and finding applications.

Here, our study leads to the first proposal of an elastic metamaterial plate showing conical refraction and a fabricated elastic metamaterial capable of translocating a mechanical wave as if being teleported. An engineered metamaterial can provide an innovative approach to achieve translocation of an elastic stress wave. Our proposed metamaterial shows a high manufacturability because it is aluminum-based, which is the most widely utilized medium in recent industries, with a slit-

inserted holey structure. This study rigorously evaluates the operational performance of the metamaterial through numerical simulation and experiments. The metamaterial is designed with non-resonant unit cells valid for broadband frequency bandwidth. Furthermore, this study also demonstrates a method for transforming multi-directional wave propagation in the metamaterial, generated by conical refraction, into selective unidirectional wave propagation. In addition, the topology optimization is used to design new configuration of metamaterial unit cells for various deflection angles. Through findings from optimization results, the performance of the engineered metamaterial can be improved in terms of directional tunability. The proposed system in this study is expected to be applied in non-destructive testing of mechanical waves, ultrasonic imaging, and a novel type of cloaking.

Keywords: Metamaterials, Conical refraction, Anisotropy, Elastic waves,

Topology optimization

Student Number: 2010-20692

CONTENTS

ABSTRACT	i
CONTENTS.....	iii
LIST OF TABLES	vii
LIST OF FIGURES.....	viii

CHAPTER 1

INTRODUCTION.....	1
1.1 Phononic crystals and metamaterials	1
1.2 Motivation and research objectives.....	3
1.3 Outline of thesis	7

CHAPTER 2

FUNDAMENTAL PRINCIPLES OF WAVE PROPAGATION IN PERIODIC ELASTIC MEDIUM.....	9
2.1 Wave behaviors in periodic elastic structures.....	9
2.1.1 Dispersion curves	9
2.1.2 Equi-frequency contours	15
2.2 Brillouin zones in two-dimensional periodic structures.....	19
2.3 Wave propagation characteristics by changing the stiffness tensor.....	23

CHAPTER 3

ELASTIC WAVE TRANSLOCATION METAMATERIALS BY CONICAL

REFRACTION.....37

3.1 Overview 37

3.2 Design and realization of anisotropic metamaterials..... 39

3.2.1 Condition for conical double point in elastic medium 39

3.2.2 Engineered metamaterials 41

3.3 Numerical simulations for conical refraction of elastic waves 43

3.3.1 Wave propagation simulations 43

3.3.2 Adjusting the deflection angle by altering the anisotropy factor.... 45

3.4 Experimental demonstration of metamaterials..... 49

3.4.1 Experimental procedure 49

3.4.2 Short-time Fourier transform results 53

3.4.3 Wide operating frequency range of metamaterials..... 55

3.5 Selection of the travel path in engineered metamaterials..... 57

3.6 Summary 62

CHAPTER 4

IN-DEPTH ANALYSIS ON ENGINEERED METAMATERIALS80

4.1 Overview 80

4.2 The effect of metamaterial geometry perturbation..... 82

4.3 S-parameter retrieval method for the effective property 85

4.4 Phase information of transmitted elastic waves	87
4.5 Time transient analysis	89
4.5.1 Snapshot of wave propagation in the engineered metamaterial	89
4.5.2 Power transmission calculation	91
4.6 Detouring around the high-risk area.....	94
4.7 Summary	98

CHAPTER 5

TOPOLOGY OPTIMIZATION OF METAMATERIAL UNIT CELLS FOR ADJUSTING THE DEFLECTION ANGLE

5.1 Overview	119
5.2 Topology optimization of periodic structures in frequency domain.....	121
5.3 Topology optimization of periodic structures in wavenumber domain ...	124
5.3.1 Design proposal to control the deflection angle	124
5.3.2 Formulations for topology optimization.....	126
5.3.3 Optimal configurations of metamaterial unit cells	130
5.4 Summary	133

CHAPTER 6

CONCLUSIONS

APPENDIX A	
SUPERCELL ANALYSIS IN TOPOLOGY OPTIMIZATION OF PERIODIC	
STRUCTURES.....	146
A.1 Overview	146
A.2 Dispersion analysis in the 45°-rotated augmented supercell.....	148
A.3 Application in topology optimization of phononic crystals	155
A.4 Summary	159
REFERENCES.....	169
ABSTRACT (KOREAN).....	179

LIST OF TABLES

Table 3.1 Effective density and effective stiffness tensor of the elastic metamaterial for the frequency range from 60 kHz to 120 kHz.	63
Table 4.1 Parameter study for geometry size of the anisotropic elastic metamaterial unit cell. Especially for the lattice period along x direction.	99
Table 4.2 Parameter study for geometry size of the anisotropic elastic metamaterial unit cell. Especially for the lattice period along y direction.	100
Table 4.3 Parameter study for geometry size of the anisotropic elastic metamaterial unit cell. Especially for the slit width.	101
Table 4.4 Parameter study for geometry size of the anisotropic elastic metamaterial unit cell. Especially for the slit height.	102
Table 4.5 Parameter study for geometry size of the anisotropic elastic metamaterial unit cell. Especially for the distance between adjacent slits in the x direction.	103

LIST OF FIGURES

Figure 2.1 Dispersion curve of a periodic structure having aluminum host and tungsten inclusion. Configuration of unit cell (left). Dispersion curve (right).....27

Figure 2.2 Equi-frequency contours of a periodic structure having aluminum host and tungsten inclusion. Configuration of unit cell (left). EFCs at three different frequencies in the first Brillouin zone (middle). EFC at 64 kHz in the whole wavevector domain (right).28

Figure 2.3 (a) Direct lattice of the two-dimensional periodic structures consisting of square unit cells having period p . (b) Reciprocal lattice and Brillouin zones.....29

Figure 2.4 EFC shape and S_0 wave propagating simulation for the aluminum medium.....30

Figure 2.5 EFC shape and S_0 wave propagating simulation for the effective medium of which stiffness property C_{11} is greater than C_{66} about 10 times.....31

Figure 2.6 EFC shape and S_0 wave propagating simulation for the effective medium of which stiffness property C_{11} is greater than C_{66} about 2.5 times.....32

Figure 2.7 EFC shape and S_0 wave propagating simulation for the effective medium of which stiffness property C_{11} is greater than C_{66} about 1.4 times.....33

Figure 2.8 EFC shape and S_0 wave propagating simulation for the effective medium of which stiffness property C_{11} is greater than C_{66} about 1.1 times.....34

Figure 2.9 EFC shape and S_0 wave propagating simulation for the effective medium of which stiffness property C_{11} is equal to C_{66}35

Figure 2.10 EFC shape and S_0 wave propagating simulation for the effective medium of which stiffness property C_{11} is a little less than C_{66}36

Figure 3.1 The engineered anisotropic metamaterial unit cell and the elastic stress wave propagation along the metamaterial plates. (a) Unit cell dimensions of the structured anisotropic metamaterial plate. (b) Translocation of normal incident elastic waves, both upward and downward. The center of behind the metamaterial where the elastic stress waves cannot reach is designated as safety zone.64

Figure 3.2 Dispersion curve and equi-frequency contours for the engineered metamaterial plate. (a) Dispersion curve along ΓX direction for the proposed metamaterial. (b) Equi-frequency contours at 60, 90 and 120 kHz for elastic metamaterial plate.65

Figure 3.3 (a) Simulation model for 90 kHz longitudinal wave incident case. (b,c) Normalized von Mises stress field distribution for (b) the engineered metamaterial and (c) effective medium. (d) Simulation model for 90 kHz transverse wave incident case. (e,f) Normalized von Mises stress field distribution for (e) the engineered metamaterial and (f) effective medium.66

Figure 3.4 Adjusting the deflection angle by changing the effective elasticity tensor. Normalized von Mises stress field distribution for 90 kHz longitudinal wave incident case (White dashed box: the region for the effective medium of (a) $C_{12} = 1.994 \times 10^9$ Pa and (b) $C_{12} = 9.994 \times 10^9$ Pa).67

Figure 3.5 Experimental set-up for evaluating the performance of the structured elastic metamaterial plate. (a) Schematic diagram of experimental measurement system (left) and zoomed-in view of the fabricated metamaterial (right). (b) Actual set-up of the experiment. (c) Generated 90 kHz input Garbor pulse signal and measured signal at point #5 and #9.68

Figure 3.6 Experimental set-up for wave generation and measurement system. (a) Schematic diagram of experimental measurement system. (b) Experiment equipment: function generator, power amplifier, pre-amplifier, oscilloscope.....69

Figure 3.7 Geometric dimension of the manufactured plate.70

Figure 3.8 Experimental raw data at the measuring points from #1 to #9. This data is for the case of S_0 wave transmitter and S_0 wave receiver.71

Figure 3.9 Experimental raw data at the measuring points from #10 to #17. This data is for the case of S_0 wave transmitter and S_0 wave receiver.72

Figure 3.10 Experimental raw data at the measuring points from #1 to #9. This data is for the case of S_0 wave transmitter and SH_0 wave receiver.73

Figure 3.11 Experimental raw data at the measuring points from #10 to #17. This data is for the case of S_0 wave transmitter and SH_0 wave receiver.74

Figure 3.12 Short-time Fourier transform results using experimental data. (a,b) Case for 90 kHz longitudinal wave transmitter and (a) longitudinal wave or (b) transverse wave receiver. (c,d) Case for 90 kHz transverse wave transmitter and (c)

longitudinal wave or (d) transverse wave receiver.75

Figure 3.13 Short-time Fourier transform results using experimental data. (a) Cases for 60 kHz longitudinal wave transmitter and longitudinal wave receiver (left) or 60 kHz longitudinal wave transmitter and transverse wave receiver (right). (b) Cases for 60 kHz transverse wave transmitter and longitudinal wave receiver (left) or 60 kHz transverse wave transmitter and transverse wave receiver (right).76

Figure 3.14 Short-time Fourier transform results using experimental data. (a) Cases for 120 kHz longitudinal wave transmitter and longitudinal wave receiver (left) or 120 kHz longitudinal wave transmitter and transverse wave receiver (right). (b) Cases for 120 kHz transverse wave transmitter and longitudinal wave receiver (left) or 120 kHz transverse wave transmitter and transverse wave receiver (right).77

Figure 3.15 Wave path choice by tuning the phase of two transmitters. (a) Simulation result for simultaneous excitation of transmitters for 90 kHz longitudinal wave and transverse wave. (b,c) Experimental STFT results for the situation in a. (d) Simulation result for simultaneous excitation of transmitters for 90 kHz longitudinal wave and transverse wave. Setting is identical with a except for transmitter for transverse wave set-up to have an opposite phase to the one in a. (e,f) Experimental STFT results for the situation in d.78

Figure 3.16 Defense of safety zone against normal incident elastic stress waves with and without the engineered anisotropic metamaterials. (a) Numerical simulation result when transverse wave incident normally on safety zone. (b) Additional two metamaterials having the horizontal length L_{MM} are placed in front and back of the safety zone with a distance of L_c79

Figure 4.1 Dispersion curve of proposed anisotropic metamaterial along k_x (ΓX), k_y (ΓY) and 45° (ΓM) axis.	104
Figure 4.2 Simulation model for calculating transmission and reflection coefficients (upper panel). EFC estimations by using measured scattering parameters or retrieved effective properties at 100 kHz (lower panel).	105
Figure 4.3 Validation of retrieved effective parameters by the comparison of scattering parameters at 100 kHz.	106
Figure 4.4 Graph for effective density and effective stiffness tensor obtained by S-parameter retrieval method in the frequency range from 50 kHz to 120 kHz.	107
Figure 4.5 Phase information by numerical simulation and experimental signals. (a,b) Numerical phase information along the vertical line at the 200 mm behind of the metamaterial. (c,d) Experimentally measured signal at point #5 (blue and red solid) and point #13 (cyan and magenta dashed).	108
Figure 4.6 Time transient analysis for effective medium of proposed anisotropic elastic metamaterial. (a) Gabor pulse of longitudinal waves propagates along both negative and positive x directions and incident on metamaterial. (b,c) Normalized power density for (b) longitudinal wave and (c) transverse wave component at the time 64.5, 124.5, 174.5 and 214.5 μ s.	109
Figure 4.7 Time transient analysis for effective medium of proposed anisotropic elastic metamaterial. (a) Gabor pulse of transverse waves propagates along both	

negative and positive x directions and incident on metamaterial. (b,c) Normalized power density for (b) longitudinal wave and (c) transverse wave component at the time 64.5, 124.5, 174.5 and 214.5 μs 110

Figure 4.8 Schematic diagram of detouring around the high-risk area by using anisotropic elastic metamaterials. 111

Figure 4.9 Numerical simulation results of S_0 wave excitation to verify the detouring of high-risk area. 112

Figure 4.10 Numerical simulation results of SH_0 wave excitation to verify the detouring of high-risk area. 113

Figure 4.11 Numerical simulation results when 90 kHz SH_0 wave incidents directly on the object whose size is 0.1 m and 0.05 m for width and height respectively..... 114

Figure 4.12 Numerical simulation results when 90 kHz SH_0 wave incidents on the engineered elastic metamaterial. It makes a detour around object whose size is 0.1 m and 0.05 m for width and height respectively. 115

Figure 4.13 Numerical simulation results when 90 kHz SH_0 wave incidents on the engineered elastic metamaterial. The horizontal length of the safety zone is set to be larger value. 116

Figure 4.14 Numerical simulation results when 90 kHz SH_0 wave incidents directly on the object whose size is 0.1 m and 0.2 m for width and height

respectively..... 117

Figure 4.15 Numerical simulation results when 90 kHz SH_0 wave incidents on the engineered elastic metamaterial. It makes a detour around object whose size is 0.1 m and 0.2 m for width and height respectively. 118

Figure 5.1 (a) The proposed anisotropic metamaterial unit cell and its EFC. (b) EFCs of effective medium having $C_{12} = 0.1994 \times 10^{10}$ Pa or $C_{12} = 0.8994 \times 10^{10}$ Pa..... 134

Figure 5.2 Normal and shear stress field distribution when the 90 kHz SH_0 wave incidents on the effective medium whose C_{12} has the value of 0.5994×10^{10} Pa. 135

Figure 5.3 Normal and shear stress field distribution when the 90 kHz SH_0 wave incidents on the effective medium whose C_{12} has the value of 0.1994×10^{10} Pa. 136

Figure 5.4 Normal and shear stress field distribution when the 90 kHz SH_0 wave incidents on the effective medium whose C_{12} has the value of 0.8994×10^{10} Pa. 137

Figure 5.5 Design proposals for topology optimization: Design #1 is for the case that the deflection angle is 43.7° , and Design #2 is for the case that the deflection angle is 31.1° 138

Figure 5.6 Topology optimization results of design #1. The unit cell configuration and EFC at 0, 20, 80, 150 and final iterations. 139

Figure 5.7 Iteration history of the objective function and four constraints for the design #1. 140

Figure 5.8 Topology optimization results of design #2. The unit cell configuration and EFC at 0, 30, 100, 200 and final iterations. 141

Figure 5.9 Iteration history of the objective function and four constraints for the design #2. 142

Figure A.1 (a) The two-dimensional phononic crystal consisting of an aluminum host and tungsten inclusions. (b) The original unit cell C and the dispersion curves with respect to C . (c) The 45°-rotated augmented supercell C_{S-45° and the dispersion curves with respect to C_{S-45° 160

Figure A.2 (a) The reciprocal lattices and (b) the 1st Brillouin Zones (BZs) corresponding to the original unit cell C and the 45°-rotated augmented supercell C_{S-45° . The 1st BZs are marked as Z of C and Z_{S-45° of C_{S-45° 161

Figure A.3 The illustration of a folding mechanism of Z_{S-45° onto Z 162

Figure A.4 (a) The illustration of a folding process, especially when the MX line of Z is folded onto the $\Gamma_S M_S$ line of Z_{S-45° . (b) Comparison of the dispersion

curves along the $\Gamma_S M_S$ line for Z_{S-45° and the ΓX & MX lines for Z ..163

Figure A.5 (a) The illustration of a folding process, especially when that the ΓM line of Z is folded onto the $\Gamma_S X_S$ line of Z_{S-45° . (b) Comparison of the dispersion curves along the $\Gamma_S X_S$ line for Z_{S-45° and the ΓM line for Z ..164

Figure A.6 The numerical simulation to verify whether the modes at *A*, *B*, *C* and *D* in Fig. A.4(b) can propagate or not through a two-dimensional PC analyzed with respect to the 45°-rotated augmented supercell. (a) Simulation model. The velocity-field plots at the (b) 55 kHz and (c) 75 kHz excitation. 165

Figure A.7 Topology optimization of a two-dimensional PC for bandgap maximization. (a) Initial and (b) optimal configurations and the corresponding dispersion curves. (c) Comparison of the dispersion curves along the $M_S \Gamma_S$ line for Z_{S-45° and the $X\Gamma$ & XM lines for Z 166

Figure A.8 The optimized configuration obtained by the periodicity-controlling bandgap-maximizing topology optimization with (a) $\alpha=0.3$ and (b) $\alpha=0.7$ 167

Figure A.9 The iteration histories for the bandgap maximizing topology optimization (a) without and (b) with the periodicity-preserving methodology maintaining the original unit cell configuration for the case of $\alpha=0.3$ 168

CHAPTER 1

INTRODUCTION

1.1 Phononic crystals and metamaterials

Phononic Crystals (PCs) with periodically-arranged inclusions inside a homogeneous host are useful for controlling elastic and acoustic waves. Intrinsic wave phenomena found in PCs, such as bandgap [1-3] and negative refraction [4], can be used for various applications including wave focusing [5], waveguiding [6], wave filtering [7], and wave attenuation [8]. Because the manipulation of these wave phenomena is closely related to the manipulation of dispersion curves, accurate analysis of dispersion curves is important. In addition, tailoring of dispersion curves by varying various PC parameters such as material property, lattice symmetry, resonator shape, and rotation of inclusions has been an active field of study [9-16].

Metamaterials are the other kind of periodic system, the structure size is much smaller than the wavelength (Phononic crystals have scalable size with the wavelength). For this reason, metamaterials can be considered under long-wavelength assumption, and thus the effective property can be defined for metamaterials [17-19]. This is the reason why metamaterials have been received with great interest even though both phononic crystals and metamaterials can show amazing wave propagation phenomena.

The effective properties of metamaterials are permeability and permittivity for electromagnetic waves; density and bulk modulus for acoustic waves; density and stiffness tensor for elastic waves. Among them, elastic waves have been known that the physics are especially difficult more than others. The reason of this difficulty is from coexistence of longitudinal and transverse waves.

Now, it should be mentioned that metamaterials are highly useful for demonstrating special anisotropy of medium. As previously mentioned, metamaterials can be expressed with effective properties. If one controls the effective properties of metamaterials, they can show various wave propagation phenomena such as hyperlens [20, 21], cloaking [22], acoustic sensor [23], etc. Here, the negative effective properties are very valuable discovery. Many researches realize and exploit metamaterials having the negative effective properties with resonant type unit cells.

1.2 Motivation and research objectives

A wave naturally propagates in the direction identical to an incident, rather than being refracted at a positive or negative angle, when the normal incidence of waves travels through isotropic media such as aluminum and steel [24, 25]. On the other hand, a spatial separation of normally incident waves with multidirectional deflection occurs by using the acoustic axes [26-28] (optical axes [29] for electromagnetic waves) which is a unique property, occurring in an anisotropic medium such as a biaxial crystal. Acoustic and optical axes are the direction in which two or more wave sheets meet in the Equi-Frequency Contour (EFC). This phenomenon, so-called conical refraction [25, 28-36] as mentioned above, is a feature that appears under specific anisotropic conditions, and is not available in a homogeneous isotropic medium. If an engineered structure were to be designed to produce conical refraction by only using a metallic medium such as aluminum, the structure would have numerous applications. To implement such a design, this study exploits a metamaterial, which has a periodic structure composed of sub-wavelength scale unit cells, to realize the phenomenon of conical refraction. By doing this, a system to translocate mechanical stress waves using conical refraction is proposed.

Metamaterials can be used to design a system exhibiting anisotropic characteristics because the sub-wavelength scale of unit cells can induce effective material properties [17-19] (Electromagnetic waves: effective permeability and permittivity;

acoustic waves: effective density and bulk modulus; elastic waves: effective density and stiffness). The effective properties of metamaterials can be exploited to control the anisotropy in a system and this is widely applicable in various fields such as hyperlens [20, 21], cloaking [22], and acoustic sensors [23]. In doing so, the value of an effective property in a metamaterial can be negative, which is important, because it mostly needs unit cells based on the resonant structure, thereby operating in narrow frequency bandwidth.

Recently, new studies have been reported to propose anisotropic metamaterials showing conical refraction. In the case of electromagnetic waves, biaxial hyperbolic metamaterials have a negative value in one of dielectric constants along three principal directions; thus, the metamaterial shows conical refraction [37]. Furthermore, a metamaterial composed of a pseudo-chiral medium with a chirality parameter allows deflection of normally incident waves [38, 39]. Also, conically refracted waves have been demonstrated via numerical simulation by designing a specific EFC shape based on a bi-anisotropic metamaterial [40]. These studies excellently showed that electromagnetic waves can be deflected while propagating along metamaterials with specific effective properties due to conical refraction only existing in an anisotropic medium. However, further studies and experiments are strongly required to determine which structure would be able to realize this concept. Most importantly, these studies are limited to electromagnetic waves and no

theoretical and experimental studies have been conducted on metamaterials with elastic waves propagating along pipe or plate structures.

In the thesis, the research objectives can be summarized as follows.

- **Realization of the anisotropic elastic metamaterial implementing conical refraction phenomenon**

In this study, we propose an elastic metamaterial plate with which to conically refract waves by using only aluminum, an isotropic metallic medium. The study implements the phenomenon onto a single-phase isotropic plate under specific anisotropic conditions. The proposed metamaterial deflects normally incident elastic waves inside the metamaterial, rather than propagating the waves directly. Furthermore, the numerical simulation and experiments show that, when exiting the metamaterial, the waves propagate in the direction perpendicular to the metamaterial slab, the incident direction. (See the schematic diagram in Fig. 3.1.) The elastic metamaterials used in this study are composed of non-resonant type unit cells with rectangular slits installed on an aluminum plate; thus, there are no restrictions on a narrow operational frequency bandwidth. Thus, our metamaterial is innovative in translocating stress waves at the broadband frequency.

- **Translocation of elastic waves by exploiting the engineered metamaterial**

Also, this study suggests and examines a method of unidirectional, rather than multidirectional, deflection of elastic waves by using the proposed metamaterial. An elastic wave propagating along a plate can behave as if being a teleportation while passing the metamaterial slab. An elastic wave is a mechanical stress wave propagating along a solid medium and is used in the fields of nondestructive testing, structural health monitoring, and ultrasonic imaging techniques [41-44]. Elastic waves are more complex than electromagnetic waves or acoustic waves because they comprise a mixture of longitudinal and transverse waves [24, 25, 45]. Therefore, an innovative translocation of elastic waves through the engineered elastic metamaterial may considerably advance the aforementioned fields.

- **Design of metamaterial unit cells for adjusting the deflection angle by using the topology optimization method**

Topology optimization is a method that finds optimal material layout of structures which satisfy their design objectives. In this work, we explain the methodology to find a new configuration of metamaterial unit cells with respect to several deflection angles by using the topology optimization method. The objective function is to follow the target EFC shape. Formulations for conducting the topology optimization and the optimal results are introduced in this study.

1.3 Outline of thesis

In Chapter 2, fundamentals of periodic structure are introduced; the dispersion curve in frequency domain and the equi-frequency contour in wavenumber domain are decisive indicator for interpreting the wave propagation in periodic structures such as phononic crystals, photonic crystals, and metamaterials. Especially, in elastic medium, the material identity can be expressed with the stiffness tensor. The wave propagation characteristics with respect to various stiffness tensors are explained to illustrate the condition for conical refraction of elastic medium.

In Chapter 3, the anisotropic elastic metamaterial is proposed. The dispersion characteristics of elastic waves propagating inside the designed metamaterial is described with the dispersion curve and equi-frequency contour in the range of frequency interest. To satisfy the condition for conical refraction, a special anisotropy is satisfied with an elaborately designed metamaterial unit cell. Thus, the effective property of the metamaterial unit cell is exploited with the special relation between components of the stiffness tensor. Numerical simulations and experiments are conducted to demonstrate the conical refraction performance of the engineered metamaterial. There is also a methodology for adjusting the deflection angle. The broadband metamaterial is realized and verified here with experiments, which is based on a non-resonant type unit cell. Additionally, the system for selection of the travel path inside the metamaterial is reported.

In Chapter 4, an in-depth analysis on the engineered metamaterial is discussed. The perturbation study on the main geometric factors of the metamaterial unit cell is introduced. The effective property of the elastic metamaterial can be defined by S-parameter retrieval method, and its procedure is discussed here. The phase information of transmitted elastic waves after passing through the metamaterial slab is analyzed, which is crucial for implementing the system of selection of travel path. Time transient analysis is conducted and compared with the harmonic analysis results in Chapter 3. Power transmission is calculated with the time transient analysis results.

In Chapter 5, the design of metamaterial unit cells with topology optimization method is newly introduced for adjusting the deflection angle. Conical refraction can deflect elastic waves, and its deflection angle can be tuned by controlling the anisotropy of the system. Thus, the new system showing various deflection angles is proposed here from the optimization results. At first, the topology optimization of phononic crystals to maximize the bandgap size is introduced as an example of designing the periodic structure. Then, the formulations for the topology optimization of metamaterial unit cells are discussed, and its optimization results are reported. Optimal configurations for two target deflection angles are explained.

In Chapter 6, we summarize the achievement of research objectives.

CHAPTER 2

FUNDAMENTAL PRINCIPLES OF WAVE PROPAGATION IN PERIODIC ELASTIC MEDIUM

2.1 Wave behaviors in periodic elastic structures

2.1.1 Dispersion curves

Dispersion curves and equi-frequency contours are very fundamental but important indicators since wave propagation features can be explained through those two graphs. Let's explain firstly the Finite Element Method (FEM) of periodic structures to obtain the dispersion curves. Consider the governing equation describing wave motion in an elastic medium:

$$\nabla(\lambda + \mu)\nabla \cdot \mathbf{u} + \nabla \cdot \mu \nabla \mathbf{u} = \rho \frac{\partial^2 \mathbf{u}}{\partial t^2} \quad (2.1)$$

where $\mathbf{u} = (u, v, w)$ is the displacement vector, λ and μ are Lamé's constants, and the material density is ρ . The symbols ∇ and t denote gradient operator and time. Here in Chapter 2, it will be considered two-dimensional bulk phononic crystals lying on the $x - y$ plane, in which waves are assumed to propagate on the $x - y$ plane. In this circumstance, elastic waves can be decoupled into in-plane and out-of-plane modes according to the direction of displacement fields. Thus, equation (2.1) can be separated into the following forms:

$$\begin{bmatrix} \frac{\partial}{\partial x} \left((\lambda + 2\mu) \frac{\partial u}{\partial x} + \lambda \frac{\partial v}{\partial y} \right) + \frac{\partial}{\partial y} \left(\mu \left(\frac{\partial u}{\partial y} + \frac{\partial v}{\partial x} \right) \right) \\ \frac{\partial}{\partial x} \left(\mu \left(\frac{\partial u}{\partial y} + \frac{\partial v}{\partial x} \right) \right) + \frac{\partial}{\partial y} \left((\lambda + 2\mu) \frac{\partial v}{\partial y} + \lambda \frac{\partial u}{\partial x} \right) \end{bmatrix} = \rho \begin{bmatrix} \frac{\partial^2 u}{\partial t^2} \\ \frac{\partial^2 v}{\partial t^2} \end{bmatrix} \quad (2.2)$$

$$\frac{\partial}{\partial x} \left(\mu \frac{\partial w}{\partial x} \right) + \frac{\partial}{\partial y} \left(\mu \frac{\partial w}{\partial y} \right) = \rho \frac{\partial^2 w}{\partial t^2}. \quad (2.3)$$

These two wave modes are independent from each other, so in-plane and out-of-plane wave modes are analyzed separately. For periodic structures of which the unit cell is defined as Ω , the Floquet-Bloch wave solutions are used to solve equations (2.2) and (2.3) as

$$\begin{bmatrix} u \\ v \end{bmatrix} = \begin{bmatrix} \tilde{u}(\mathbf{r}) \\ \tilde{v}(\mathbf{r}) \end{bmatrix} e^{i(\mathbf{k}^T \mathbf{r} - \omega t)} \quad \text{for in-plane waves,} \quad (2.4)$$

$$w = \tilde{w}(\mathbf{r}) e^{i(\mathbf{k}^T \mathbf{r} - \omega t)} \quad \text{for out-of-plane waves} \quad (2.5)$$

where $\tilde{\mathbf{u}} = (\tilde{u}, \tilde{v}, \tilde{w})$ is the Ω -periodic displacement vector, $\mathbf{r} = (x, y)$ is the position vector, $\mathbf{k} = (k_x, k_y)$ is the wavevector, and ω is angular frequency.

With equations (2.4) and (2.5), the finite element equations corresponding to equations (2.2) and (2.3) become

$$[\mathbf{K}(\mathbf{k}) - \omega^2 \mathbf{M}] \tilde{\mathbf{U}} = 0 \quad \in \Omega \quad (2.6)$$

where $\tilde{\mathbf{U}}$ is the nodal point displacement vector of the unit cell, and $\mathbf{K}(\mathbf{k})$ and \mathbf{M} are the stiffness and mass matrices that can be expressed as

$$\mathbf{K}(\mathbf{k}) = \iint_{\Omega} (\mathbf{B}_1 + i\mathbf{B}_2)^T \mathbf{C} (\mathbf{B}_1 + i\mathbf{B}_2) d\Omega, \quad (2.7)$$

$$\mathbf{M} = \iint_{\Omega} \rho \mathbf{H}^T \mathbf{H} d\Omega \quad (2.8)$$

where \mathbf{H} is the displacement interpolation matrix. The elastic stiffness matrix \mathbf{C} is defined as

$$\mathbf{C} = \frac{E(1-\nu)}{(1+\nu)(1-2\nu)} \begin{bmatrix} 1 & \frac{\nu}{1-\nu} & 0 \\ \frac{\nu}{1-\nu} & 1 & 0 \\ 0 & 0 & \frac{1-2\nu}{2(1-\nu)} \end{bmatrix} \quad \text{for in-plane waves} \quad (2.9)$$

$$\mathbf{C} = \frac{E(1-\nu)}{(1+\nu)(1-2\nu)} \begin{bmatrix} \frac{1-2\nu}{2(1-\nu)} & 0 \\ 0 & \frac{1-2\nu}{2(1-\nu)} \end{bmatrix} \quad \text{for out-of-plane waves} \quad (2.10)$$

where E is Young's modulus and ν is Poisson's ratio. For the plate structure, the stiffness matrix \mathbf{C} is changed into the two-dimensional plane stress condition. The matrix $(\mathbf{B}_1 + i\mathbf{B}_2)$ is the strain-displacement matrix that can be constructed by the following process:

$$\boldsymbol{\varepsilon} = \begin{bmatrix} \varepsilon_{xx} \\ \varepsilon_{yy} \\ \gamma_{xy} \end{bmatrix} = \begin{bmatrix} \frac{\partial u}{\partial x} \\ \frac{\partial v}{\partial y} \\ \frac{\partial u}{\partial y} + \frac{\partial v}{\partial x} \end{bmatrix} = \begin{bmatrix} \frac{\partial \tilde{u}}{\partial x} + ik_x \tilde{u} \\ \frac{\partial \tilde{v}}{\partial y} + ik_y \tilde{v} \\ \frac{\partial \tilde{u}}{\partial y} + \frac{\partial \tilde{v}}{\partial x} + ik_x \tilde{v} + ik_y \tilde{u} \end{bmatrix} = (\mathbf{B}_1 + i\mathbf{B}_2) \tilde{\mathbf{U}} \quad (2.11)$$

$$\boldsymbol{\varepsilon} = \begin{bmatrix} \gamma_{zx} \\ \gamma_{yz} \end{bmatrix} = \begin{bmatrix} \frac{\partial w}{\partial x} + \frac{\partial u}{\partial z} \\ \frac{\partial w}{\partial y} + \frac{\partial v}{\partial z} \end{bmatrix} = \begin{bmatrix} \frac{\partial \tilde{w}}{\partial x} + ik_x \tilde{w} \\ \frac{\partial \tilde{w}}{\partial y} + ik_y \tilde{w} \end{bmatrix} = (\mathbf{B}_1 + i\mathbf{B}_2) \tilde{\mathbf{U}}. \quad (2.12)$$

The nodal displacement vector $\tilde{\mathbf{U}}$ has the dimensions $(2m \times 1)$ for in-plane and $(m \times 1)$ for out-of-plane wave modes respectively where m is the total number of nodes in the unit cell. The nodal displacements for a square unit cell can be grouped as

$$\tilde{\mathbf{U}} = [\tilde{\mathbf{U}}_{in} \quad \tilde{\mathbf{U}}_l \quad \tilde{\mathbf{U}}_u \quad \tilde{\mathbf{U}}_r \quad \tilde{\mathbf{U}}_b \quad \tilde{\mathbf{U}}_{ul} \quad \tilde{\mathbf{U}}_{ur} \quad \tilde{\mathbf{U}}_{bl} \quad \tilde{\mathbf{U}}_{br}]. \quad (2.13)$$

Subscripts denote the location of nodal points sequentially in accordance with *inner, left, upper, right, bottom, upper left, upper right, bottom left, and bottom right* of the unit cell, respectively. From equations (2.4) and (2.5), $\tilde{\mathbf{U}}_r$ can be expressed in terms of $\tilde{\mathbf{U}}_l$, and $\tilde{\mathbf{U}}_b$ in terms of $\tilde{\mathbf{U}}_u$. Likewise, $\tilde{\mathbf{U}}_{ur}$, $\tilde{\mathbf{U}}_{bl}$, and $\tilde{\mathbf{U}}_{br}$ can be expressed through $\tilde{\mathbf{U}}_{ul}$. Therefore, it is convenient to define $\tilde{\mathbf{U}}_f = [\tilde{\mathbf{U}}_{in} \quad \tilde{\mathbf{U}}_l \quad \tilde{\mathbf{U}}_u \quad \tilde{\mathbf{U}}_{ul}]$ consisting of independent nodal displacements and introduce a transformation \mathbf{T} such that

$$\mathbf{T}\tilde{\mathbf{U}}_f \equiv \mathbf{T}[\tilde{\mathbf{U}}_{in} \quad \tilde{\mathbf{U}}_l \quad \tilde{\mathbf{U}}_u \quad \tilde{\mathbf{U}}_{ul}] = \tilde{\mathbf{U}}. \quad (2.14)$$

Substituting equation (2.14) into equation (2.6) yields

$$[\mathbf{T}^T \mathbf{K}(\mathbf{k}) \mathbf{T} - \omega^2 \mathbf{T}^T \mathbf{M} \mathbf{T}] \tilde{\mathbf{U}}_f = 0 \quad \in \quad \Omega, \quad (2.15)$$

$$[\mathbf{K}_f(\mathbf{k}) - \omega^2 \mathbf{M}_f] \tilde{\mathbf{U}}_f = 0 \quad \in \quad \Omega \quad (2.16)$$

where $\mathbf{K}_f(\mathbf{k}) = \mathbf{T}^T \mathbf{K}(\mathbf{k}) \mathbf{T}$ and $\mathbf{M}_f = \mathbf{T}^T \mathbf{M} \mathbf{T}$. The system stiffness \mathbf{K}_f and mass \mathbf{M}_f matrices are constructed by assembling element stiffness (\mathbf{K}_e) and mass (\mathbf{M}_e) matrices as $\mathbf{K}_f = \sum_{e=1}^N \mathbf{K}_e$ and $\mathbf{M}_f = \sum_{e=1}^N \mathbf{M}_e$ where N is the total number of the finite elements used to discretize the unit cell.

Equation (2.16) is the final step of eigenvalue problem to obtain the dispersion curve of periodic structures. By solving this eigenvalue problem, one can get the relation between frequency and wavenumber. As an example, the dispersion curve of two-dimensional bulk phononic crystal of which period is 0.2 m is plotted in Fig. 2.1. Phononic crystal is constructed with aluminum host and tungsten inclusion. Between the third and fourth branches, the small bandgap is measured. This bandgap prevent wave propagating along the phononic crystal, and furthermore it can be enlarged by controlling the radius of corner inclusion or other geometric parameters.

When designing the periodic structures to maximize the bandgap size, the parameter studies involve especially the periods of unit cells. Then, the supercell analysis [46] might be essential to analyze the exact wave propagation characteristics. In Appendix, we introduce periodicity-preserving bandgap maximization problem for two-dimensional bulk phononic crystals.

2.1.2 Equi-frequency contours

Now, let's move into how to obtain Equi-Frequency Contour (EFC) involved in understanding the wave propagating direction inside the periodic structure. Let's start from following equation (2.17):

$$\mathbf{K}_e \mathbf{U}_e = \omega^2 \mathbf{M}_e \mathbf{U}_e . \quad (2.17)$$

With given frequency, element stiffness (\mathbf{K}_e) and mass (\mathbf{M}_e) matrices can be expressed as

$$\mathbf{K}_e = \int_{\Omega} (\mathbf{B} + j\mathbf{kN})^H \mathbf{C} (\mathbf{B} + j\mathbf{kN}) d\Omega , \quad (2.18)$$

$$\mathbf{M}_e = \int_{\Omega} \rho_e \mathbf{N}^T \mathbf{N} d\Omega \quad (2.19)$$

where the superscript \mathbf{H} denotes the Hermitian operator and \mathbf{N} is the displacement interpolation matrix.

By setting the wavevector \mathbf{k} as $\mathbf{k} = k\mathbf{n}_k$ with the directional unit vector

$\mathbf{n}_k = (n_x, n_y, n_z)$, the element stiffness matrix is changed into the following form:

$$\begin{aligned}
\mathbf{K}_e &= \int_{\Omega} (\mathbf{B} + j\mathbf{k}\mathbf{N})^H \mathbf{C} (\mathbf{B} + j\mathbf{k}\mathbf{N}) d\Omega \\
&= \int_{\Omega} \mathbf{B}^H \mathbf{C} \mathbf{B} d\Omega + \int_{\Omega} (j\mathbf{k}\mathbf{n}_k \mathbf{N})^H \mathbf{C} \mathbf{B} d\Omega \\
&\quad + \int_{\Omega} \mathbf{B}^H \mathbf{C} (j\mathbf{k}\mathbf{n}_k \mathbf{N}) d\Omega + \int_{\Omega} (j\mathbf{k}\mathbf{n}_k \mathbf{N})^H \mathbf{C} (j\mathbf{k}\mathbf{n}_k \mathbf{N}) d\Omega \\
&= k^2 \int_{\Omega} (j\mathbf{n}_k \mathbf{N})^H \mathbf{C} (j\mathbf{n}_k \mathbf{N}) d\Omega \\
&\quad + k \left[\int_{\Omega} (j\mathbf{n}_k \mathbf{N})^H \mathbf{C} \mathbf{B} d\Omega + \int_{\Omega} \mathbf{B}^H \mathbf{C} (j\mathbf{n}_k \mathbf{N}) d\Omega \right] + \int_{\Omega} \mathbf{B}^H \mathbf{C} \mathbf{B} d\Omega \\
&= k^2 \mathbf{A}_e + k\mathbf{B}_e + \mathbf{C}_e
\end{aligned} \tag{2.20}$$

with

$$\mathbf{A}_e = \int_{\Omega} (j\mathbf{n}_k \mathbf{N})^H \mathbf{C} (j\mathbf{n}_k \mathbf{N}) d\Omega \tag{2.21}$$

$$\mathbf{B}_e = \int_{\Omega} (j\mathbf{n}_k \mathbf{N})^H \mathbf{C} \mathbf{B} d\Omega + \int_{\Omega} \mathbf{B}^H \mathbf{C} (j\mathbf{n}_k \mathbf{N}) d\Omega \tag{2.22}$$

$$\mathbf{C}_e = \int_{\Omega} \mathbf{B}^H \mathbf{C} \mathbf{B} d\Omega. \tag{2.23}$$

The eigenvalue equation (2.17) now can be converted into the following form:

$$\begin{aligned}
(k^2 \mathbf{A}_e + k \mathbf{B}_e + \mathbf{C}_e) \mathbf{U}_e &= \omega^2 \mathbf{M}_e \mathbf{U}_e \\
\{k^2 \mathbf{A}_e + k \mathbf{B}_e + (\mathbf{C}_e - \omega^2 \mathbf{M}_e)\} \mathbf{U}_e &= 0.
\end{aligned} \tag{2.24}$$

By constructing the global matrices, the eigenvalue problem is expressed as

$$\{k^2 \mathbf{A}_g + k \mathbf{B}_g + (\mathbf{C}_g - \omega^2 \mathbf{M}_g)\} \mathbf{U}_g = 0 \tag{2.25}$$

where $\mathbf{A}_g = \sum_{m=1}^{N_e} (\mathbf{A}_e)_m$, $\mathbf{B}_g = \sum_{m=1}^{N_e} (\mathbf{B}_e)_m$, $\mathbf{C}_g = \sum_{m=1}^{N_e} (\mathbf{C}_e)_m$ and

$$\mathbf{M}_g = \sum_{m=1}^{N_e} (\mathbf{M}_e)_m . \text{ Note that } N_e \text{ is the total number of the finite elements used to}$$

discretize the unit cell.

To solve equation (2.25) for the eigenvalue k , it is convenient to change the equation (2.25) into the equation as following,

$$\begin{bmatrix} \mathbf{0} & \mathbf{I} \\ -(\mathbf{C}_g - \omega^2 \mathbf{M}_g) & -\mathbf{B}_g \end{bmatrix} \begin{bmatrix} \mathbf{U}_g \\ k \mathbf{U}_g \end{bmatrix} = k \begin{bmatrix} \mathbf{I} & \mathbf{0} \\ \mathbf{0} & \mathbf{A}_g \end{bmatrix} \begin{bmatrix} \mathbf{U}_g \\ k \mathbf{U}_g \end{bmatrix}. \tag{2.26}$$

Note that wavenumber k contains the real and complex number.

Now, one can obtain the equi-frequency contour for the given angular frequency ω using the eigenvalue problem of equation (2.26). As an example, the equi-frequency contours of two-dimensional bulk phononic crystal of which period is 0.2 m is plotted in Fig. 2.2. Phononic crystal is identical with the one in Fig. 2.1. The contour plot is drawn for three different frequencies of 62 kHz, 64 kHz, and 66 kHz (Each contour is plotted with blue, black, and red color.). Because of inhomogeneity, the contours for longitudinal and shear waves of the phononic crystal have larger radius than the ones of homogeneous aluminum medium denoted as Al_longi and Al_shear , respectively. It means that the wave velocity in periodic structures becomes slowed down.

Here, the most important thing is that the normal direction to the contour means the direction of wave energy propagation. Thus, for the bulk aluminum medium, the shape of contour is circular form because of homogeneity. Otherwise, for the periodic structure, the shape of contour is bulged in and out according to the direction. Using this feature, wave propagating directions can be elaborately controlled by designing the periodic structures.

2.2 Brillouin zones in two-dimensional periodic structures

In Section 2.2, the direct lattice and the reciprocal lattice for the most well-known type of two-dimensional periodic structures are introduced. In addition, what Brillouin zone [47] appearing in analyzing process of dispersion curves and Equi-frequency contours means is also explained.

First, in the case of two-dimensional periodic structure consisting of square unit cells, the direct lattice which is also known as a physical space can be defined as followings:

$$\mathbf{R}_{mn} = m\mathbf{a}_1 + n\mathbf{a}_2 \quad (m, n : \text{integer}) \quad (2.27)$$

$$\mathbf{a}_1 = p\hat{\mathbf{x}}, \quad \mathbf{a}_2 = p\hat{\mathbf{y}} \quad (2.28)$$

where p is period of square unit cell, \mathbf{a}_1 and \mathbf{a}_2 are unit vectors in direct lattice, $\hat{\mathbf{x}}$ and $\hat{\mathbf{y}}$ are the directional unit vectors, and \mathbf{R}_{mn} is the position of possible lattice points defined as an integral multiple of unit vectors (See Fig. 2.3(a)).

Also, it is possible to determine the reciprocal lattice by using the Fourier analysis which describes the relationship between physical space and the wavenumber space. Reciprocal lattice have unit vectors \mathbf{b}_1 and \mathbf{b}_2 , and these unit vectors

have special relationship with unit vectors of direct lattice as followings:

$$\begin{aligned} \mathbf{b}_i \cdot \mathbf{a}_j &= 2\pi\delta_{ij} \\ (\delta_{ij} &= 1 \text{ if } i = j \text{ and } \delta_{ij} = 0 \text{ if } i \neq j) \end{aligned} \quad (2.29)$$

where δ_{ij} is Kronecker delta. Reciprocal lattice means a wavevector space (i.e., $\mathbf{k} = (k_x, k_y)$) of periodic structures as shown in Fig. 2.3(b). Note that it is necessary for Brillouin zone to discuss the reciprocal lattice. Reciprocal lattice of square lattice is constructed by equation (2.29) and it can be expressed as follows:

$$\mathbf{G}_{rs} = r\mathbf{b}_1 + s\mathbf{b}_2 \quad (r, s : \text{integer}) \quad (2.30)$$

$$\mathbf{b}_1 = \frac{2\pi}{p} \hat{\mathbf{x}}, \quad \mathbf{b}_2 = \frac{2\pi}{p} \hat{\mathbf{y}} \quad (2.31)$$

where \mathbf{G}_{rs} is the position of reciprocal lattice points defined as an integral multiple of \mathbf{b}_1 and \mathbf{b}_2 (See Fig. 2.3(b)).

Since we identified how to configure the direct lattice and reciprocal lattice of two-dimensional periodic structures, now the method for finding the Brillouin zone is examined. At first, Brillouin zone which is utilized to understand the wave propagation aspect includes the primary, secondary and higher order of Brillouin

zones. Bragg condition is satisfied at the boundary of Brillouin zone. The frequency information at the position of a particular wavevector point in the first Brillouin zone has the identical with the one at all corresponding reciprocal lattice points which are integral multiple of unit vectors. This is the reason why Brillouin zone has important meaning in wave physics in the field of periodic structures.

As we explained the meaning of Brillouin zones in the reciprocal lattice, there is now need to know the Wigner-Seitz cell [48] to follow-up the procedure of finding the irreducible Brillouin zone. If one selects a certain reference point in reciprocal lattice as shown in Fig. 2.3(b), then one can draw four lines connecting the most adjacent points. These lines are denoted as dashed line in Fig. 2.3(b). Then, one can find the square polygon by depicting the vertical bisector of previous four lines. This square polygon is the so-called Wigner-Seitz cell and becomes the first Brillouin zone of the square unit cell. In the same way, the repetitive procedure can make the second and higher Brillouin zones.

With above described method, the first Brillouin zone of square lattice can be drawn as shown in Fig. 2.3(b). It is located at the region of $-\pi/p \leq k_x, k_y \leq \pi/p$ marked with blue color. In most cases, the square unit cell is horizontally and vertically symmetric structure. Then, the wavevectors only along the line $\Gamma - X - M - \Gamma$ are considered to identify wave propagation physics of periodic structures. It is so-called the irreducible Brillouin zone [47]. For

the square lattice case, symmetrical points of the irreducible Brillouin zone can be denoted as

$$\Gamma = \mathbf{0}, \quad \mathbf{X} = \frac{\pi}{p} \hat{\mathbf{x}}, \quad \mathbf{M} = \frac{\pi}{p} \hat{\mathbf{x}} + \frac{\pi}{p} \hat{\mathbf{y}}. \quad (2.32)$$

2.3 Wave propagation characteristics by changing the stiffness tensor

The material property of an elastic medium can be expressed by its density and elastic stiffness tensor. These material properties represent medium identity because of the uniqueness of material properties. Thus, each property in a medium such as aluminum, steel, and copper has inherent values. The material property of an anisotropic medium may have complexity, compared to the simplicity of an isotropic medium. Such complexity can be actively applied for the implementation of new wave phenomena. Section 2.3 focuses on C_{11} and C_{66} , elastic stiffness tensor components that are closely related to longitudinal waves and transverse waves in an elastic medium. We analyze the EFC shape and the wave propagation aspect as the value of C_{11} of an anisotropic medium as being less than, greater than, or equal to the value of C_{66} .

At first, the following description investigates wave propagation at 90 kHz along an isotropic aluminum plate prior to investigating elastic waves propagating along an anisotropic medium. Fig. 2.4 shows that C_{11} of the elastic stiffness tensor is greater than C_{66} , and that the EFC shape is circular. Among the two circular curves, the inner curve represents the S_0 wave (longitudinal wave), and the outer curve represents the SH_0 wave (transverse wave). All isotropic media have a circular EFC shape because C_{11} is always greater than C_{66} , and accordingly the speed of the

longitudinal wave is always higher than that of the transverse wave. The results of wave propagation simulation with a longitudinal wave source explain that the field distribution is only measured in the normal stress plot along the x direction. Note that Perfectly Matched Layers (PMLs) are used to absorb reflections from the outer boundary in both the right and left areas.

From now on, we consider the case where a 90 kHz S_0 wave is normally incident on an anisotropic medium having the elastic stiffness tensor values with $C_{11} = 10.722$ GPa, $C_{12} = 1.994$ GPa, $C_{22} = 10.722$ GPa, and $C_{66} = 1.072$ GPa, as shown in Fig. 2.5. Here C_{11} is ten times greater than C_{66} , and thus the EFC formation is curved, rather than circular. For more details, the outer curve is convex to the x and y axes, and concave in the 45 and -45 degree directions. The EFCs of the longitudinal and transverse waves in aluminum are represented by blue and red dashed lines for reference. Seeing wave propagation simulation, the black dashed box corresponds to the anisotropic medium area; the rest of the area corresponds to aluminum. Wave propagation is only measured in the normal stress plot (σ_{xx}); no measurement is obtained in the shear stress plot (σ_{xy}). Furthermore, incident waves pass through the anisotropic medium along the normal direction, and continue along the initial direction even after exiting the anisotropic medium. This behavior is no different from the one of an isotropic medium.

The following case considers that C_{66} is increased to $C_{66} = 4.072$ GPa, otherwise holding the same values of elastic stiffness tensor component in Fig. 2.5. Thus, as shown in Fig. 2.6, C_{11} is two and half times higher than C_{66} . Examining the outer curve of EFC, the convexity to the x and y axes is reduced, compared to that shown in Fig. 2.5, whereas the convexity is increased in the 45 and -45 degree directions. This tendency is more clearly described through Fig. 2.7 and Fig. 2.8. When C_{66} is gradually increased to $C_{66} = 7.072$ GPa and $C_{66} = 9.072$ GPa, the outer curves become more concave to the x and y axes, and convex in the 45 and -45 degree directions. However, there is still no tremendous change in the wave propagation aspect from the simulation result.

From these studies of variation of the elastic stiffness tensor, we can figure out the important feature that two curves intersect on the k_x axis of EFC as the values of C_{11} and C_{66} approach each other. Also, it reaches the analytical solution to put in the special conditions, the relationship between components of the effective stiffness tensor: $C_{11} = C_{66}$ and $C_{16} = C_{26} = 0$, into the Christoffel equation

$$(\Gamma_{im}k^2 - \rho\omega^2\delta_{im})u_m = 0.$$

Now we especially pay attention to the situation satisfying $C_{11} = C_{66}$, as shown in Fig. 2.9. The EFC curves are degenerated on the k_x axis, and thus the existence

of a conical double point is revealed. If a wave incident on the anisotropic medium satisfying the condition $C_{11} = C_{66}$, transmitted waves are conically deflected and propagate along the newly generated upper and lower paths, rather than propagating in the x direction. It is well verified in the black dashed box, and more cleared interpretations are provided in Chapter 3. Furthermore, seen in the red dashed box, waves after exiting the anisotropic medium are spatially separated and propagate along both the upper and lower paths. Additionally, the field distribution is newly measured in the shear stress plot as well as the normal stress plot. This unique wave propagation characteristic can occur in special cases satisfying $C_{11} = C_{66}$, which attracted our attention. Our study is conducted to induce the specific structure showing the conical refraction phenomenon and to test viable applications.

On the other hand, the question arises for the case where C_{66} is greater than C_{11} . Fig. 2.10 corresponds to the results of the wave propagation simulation using an anisotropic medium with $C_{66} = 12.722$ GPa. In this case, the conical refraction phenomenon cannot occur. Therefore, the simulation produces results of wave propagation in the x direction as in a common medium.

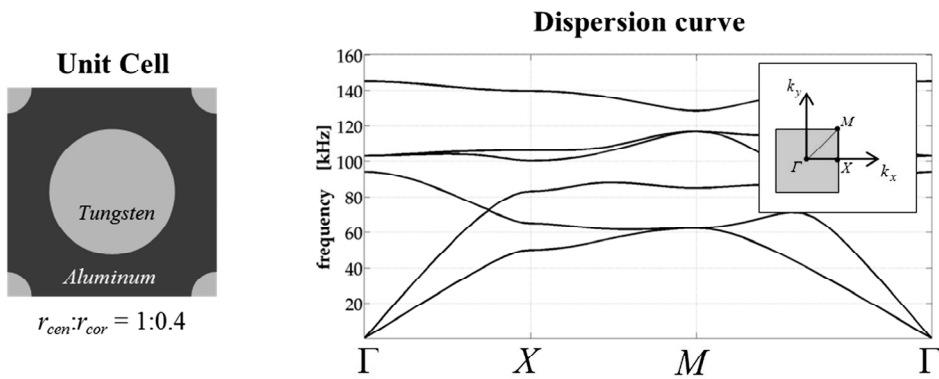


Figure 2.1 Dispersion curve of a periodic structure having aluminum host and tungsten inclusion. Configuration of unit cell (left). Dispersion curve (right).

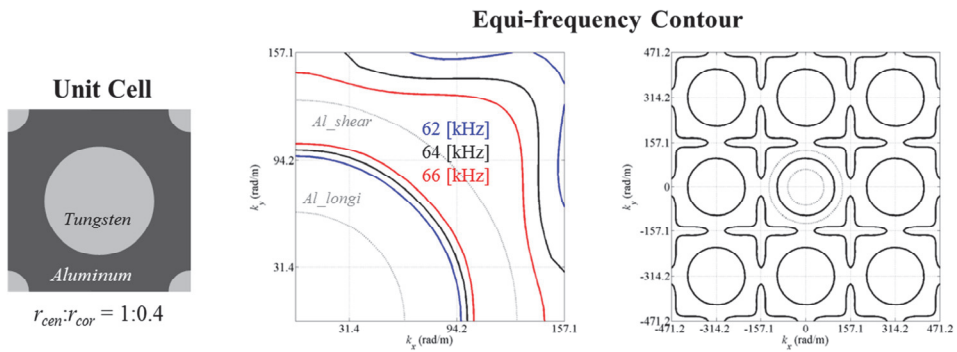


Figure 2.2 Equi-frequency contours of a periodic structure having aluminum host and tungsten inclusion. Configuration of unit cell (left). EFCs at three different frequencies in the first Brillouin zone (middle). EFC at 64 kHz in the whole wavevector domain (right).

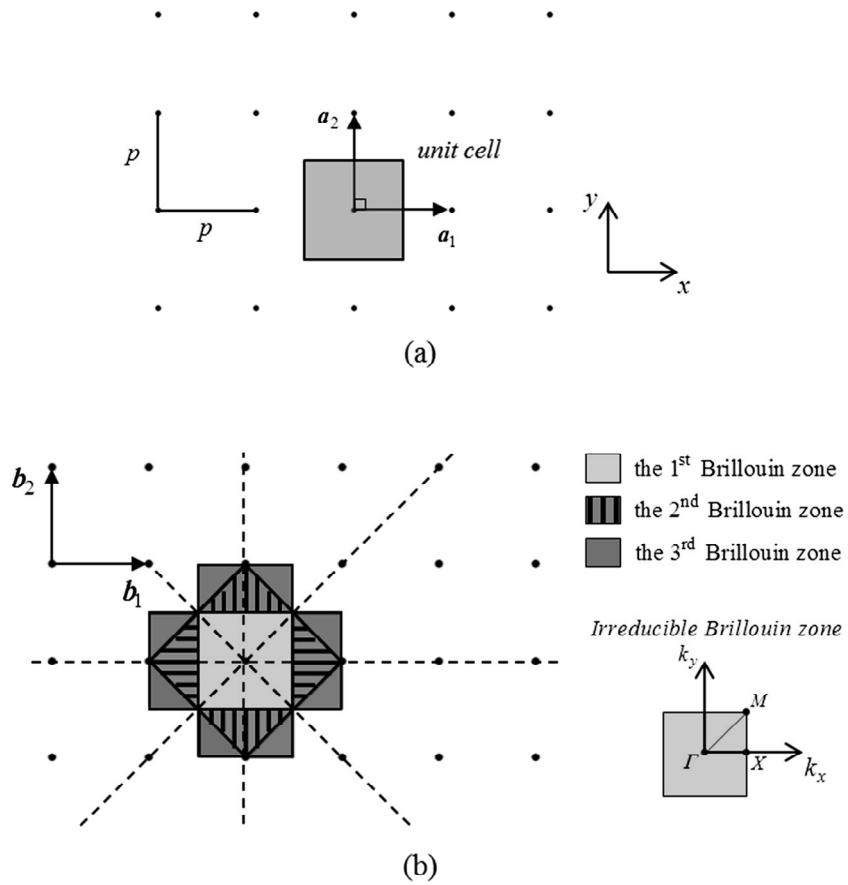


Figure 2.3 (a) Direct lattice of the two-dimensional periodic structures consisting of square unit cells having period p . (b) Reciprocal lattice and Brillouin zones.

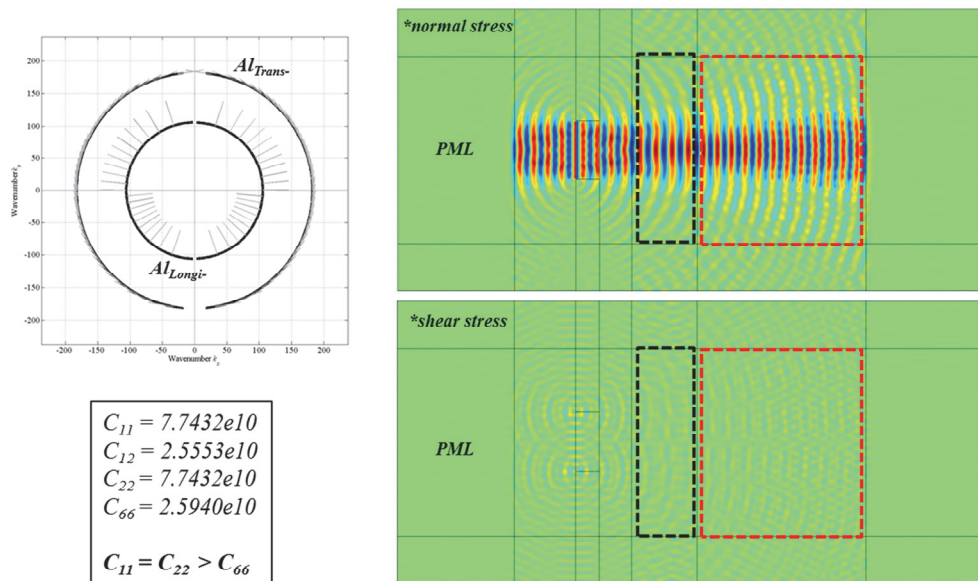


Figure 2.4 EFC shape and S_0 wave propagating simulation for the aluminum medium.

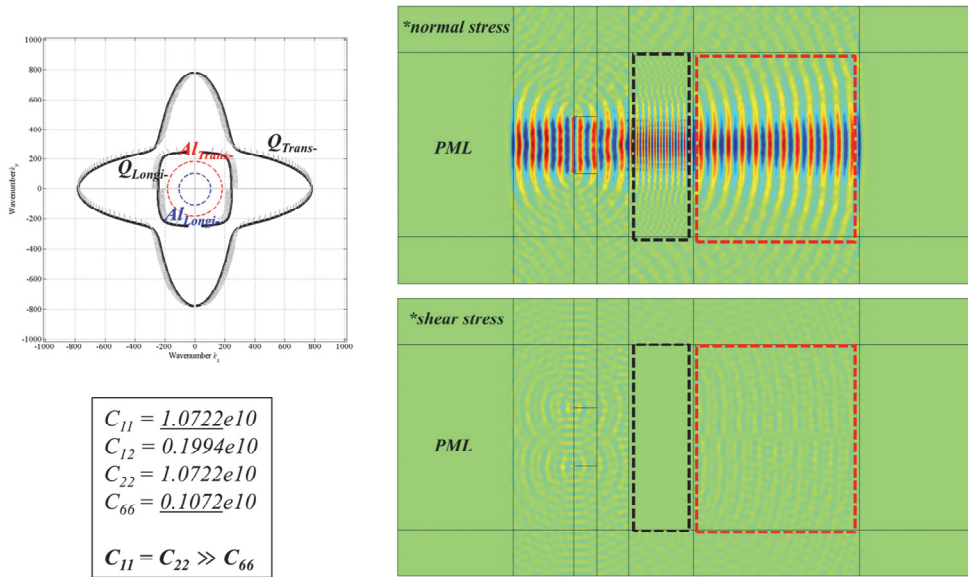


Figure 2.5 EFC shape and S_0 wave propagating simulation for the effective medium of which stiffness property C_{11} is greater than C_{66} about 10 times.

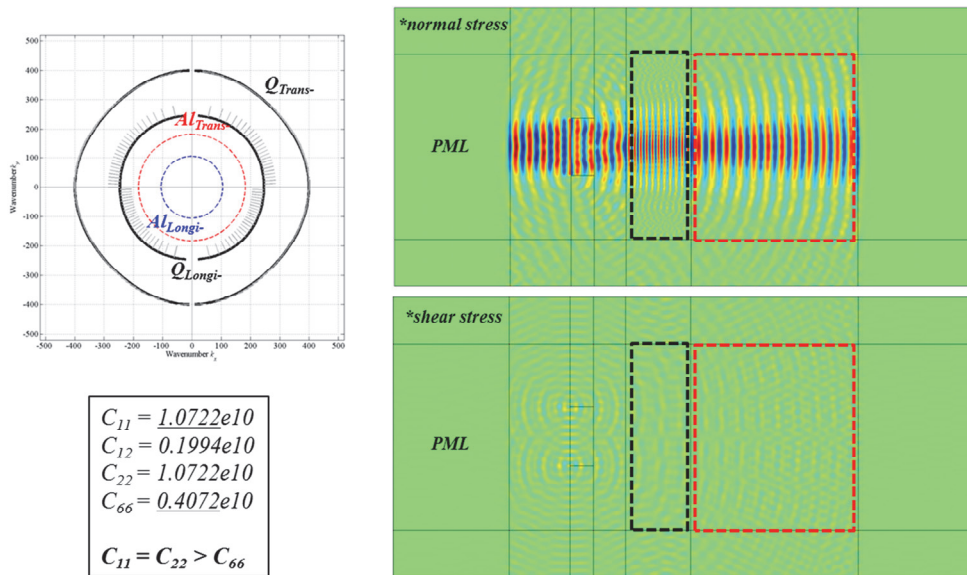


Figure 2.6 EFC shape and S_0 wave propagating simulation for the effective medium of which stiffness property C_{11} is greater than C_{66} about 2.5 times.

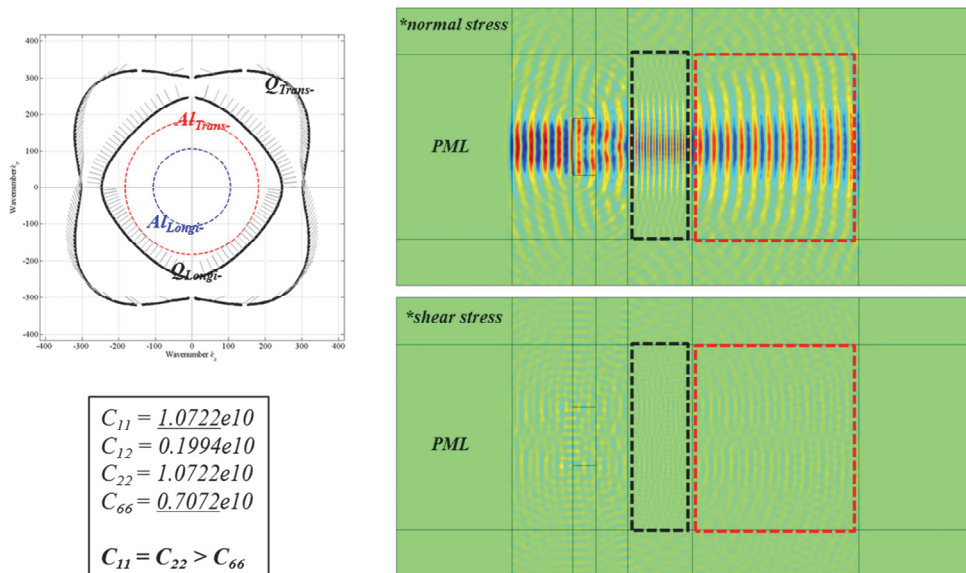


Figure 2.7 EFC shape and S_0 wave propagating simulation for the effective medium of which stiffness property C_{11} is greater than C_{66} about 1.4 times.

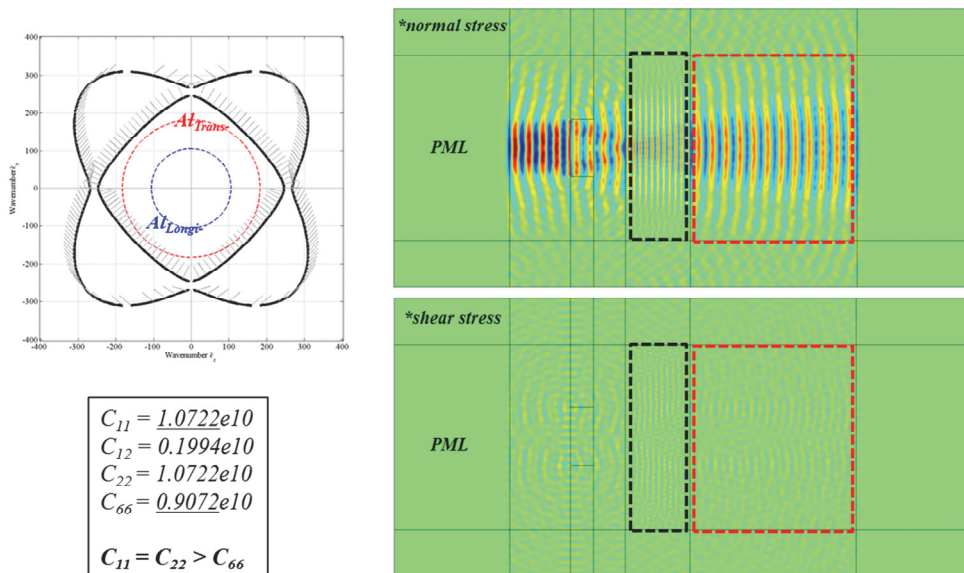


Figure 2.8 EFC shape and S_0 wave propagating simulation for the effective medium of which stiffness property C_{11} is greater than C_{66} about 1.1 times.

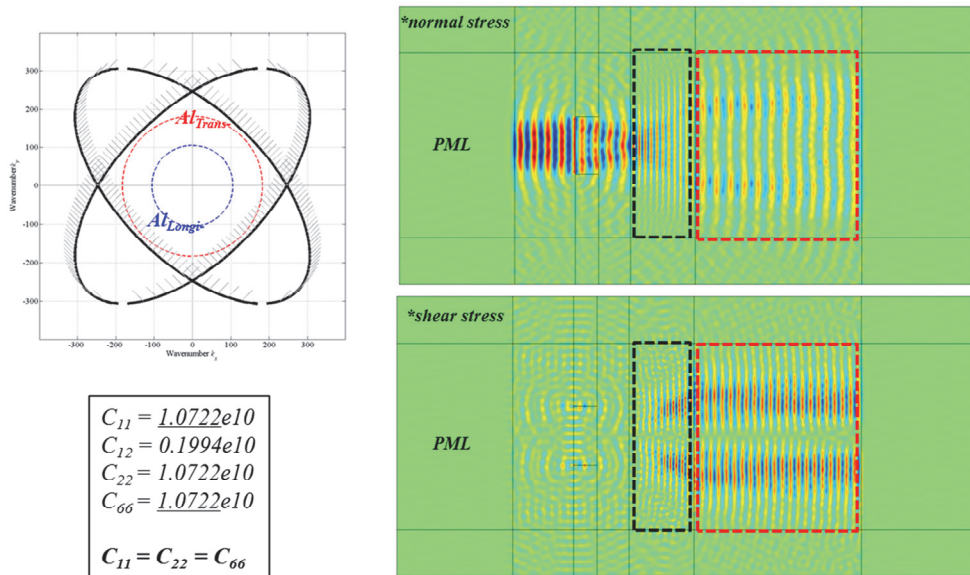


Figure 2.9 EFC shape and S_0 wave propagating simulation for the effective medium of which stiffness property C_{11} is equal to C_{66} .

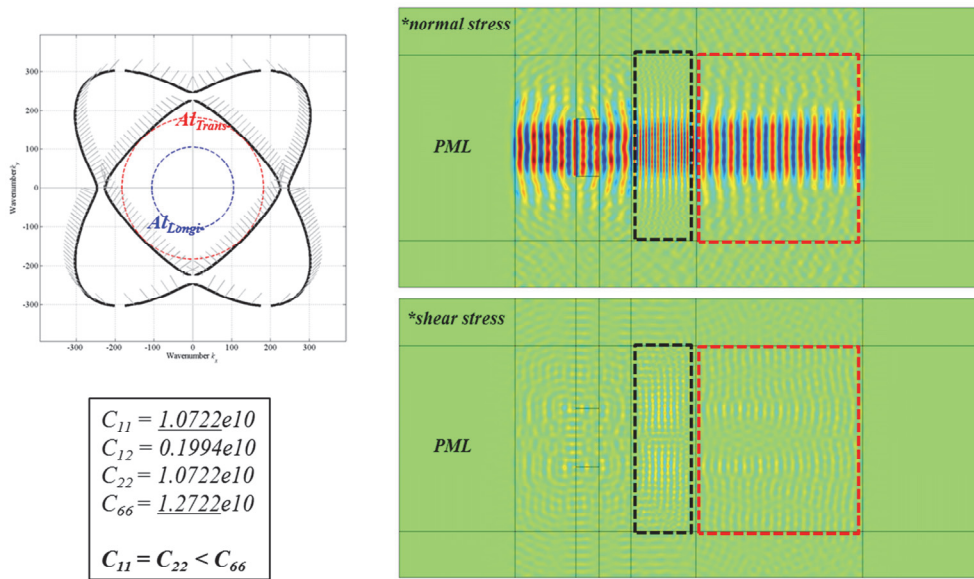


Figure 2.10 EFC shape and S_0 wave propagating simulation for the effective medium of which stiffness property C_{11} is a little less than C_{66} .

CHAPTER 3

ELASTIC WAVE TRANSLOCATION METAMATERIALS BY CONICAL REFRACTION

3.1 Overview

Conical refraction phenomenon [28-36] has been considered mainly in the optics and electromagnetics. However, this phenomenon is somewhat uncharted territory for ultrasonics, and only a few researches [30-33] have been conducted theoretically. Even though laser beam or electromagnetic waves can be conically deflected through specific anisotropic medium implementing the conical refraction, the application of conical refraction has not been clearly investigated.

In this chapter, we realize the anisotropic elastic metamaterial demonstrating the conical refraction phenomenon. The engineered metamaterial is proposed by

considering how to fulfill the condition for the conical refraction. The slit-based unit cell plays a role that the velocities of the longitudinal and the transverse waves are equal to each other. In numerical simulations, the ability of multi-directionally deflection is demonstrated with the von Mises stress field distribution. Thus, an elastic wave propagates along the newly generated two paths inside the metamaterial. The deflection angle depends on the anisotropy of the metamaterial. This feature is exploited for adjusting the deflection angle, and its results are introduced.

When elastic waves exit the metamaterial slab, they propagate in the normal direction to the boundary of the metamaterial slab, i.e., in the x direction. The performance of the designed metamaterial is verified by experiments. We explain the details of the experimental setting and procedure from generating to measuring the wave signal at the plate. Short-time Fourier transform results effectively identify the performance of the proposed metamaterial. Furthermore, our proposed metamaterial shows a wide operating frequency range because it is based on a non-resonant type unit cell. This could be very strong advantage for application of various wave propagation systems. In addition, a new system that enables choosing the travel path among two paths is discussed. We verify this ability by numerical simulations and experiments.

3.2 Design and realization of anisotropic metamaterials

3.2.1 Condition for conical double point in elastic medium

As shown in Fig. 3.1b, to implement conical refraction such that it deflects the elastic plane wave normally incident in the x -direction, the metamaterial would need to be designed with the specific EFC shape. For the engineered EFC, two wave sheets represented by the red and blue solid lines intersect at the wavevector k_x axis as shown in Fig. 3.2b. To achieve this EFC shape, the effective stiffness tensor of the elastic metamaterial is required to satisfy special conditions such that: $C_{11} = C_{66}$, and $C_{16} = C_{26} = 0$. Also, by solving the Christoffel equation $(\Gamma_{im}k^2 - \rho\omega^2\delta_{im})u_m = 0$ [24, 25] with the conditions, $C_{11} = C_{66}$ and $C_{16} = C_{26} = 0$, we can confirm the degenerated double point, the conical point at the k_x axis. It is identical with the EFC obtained from a finite element method shown in Fig. 3.2.

In the long-wavelength area where the effective property can be defined, the values of C_{11} and C_{66} show the following relationships to the velocities of the longitudinal wave (the lowest symmetric Lamb wave mode: S_0 -wave) and transverse wave (the lowest shear-horizontal wave mode: SH_0 -wave):

$V_L = \sqrt{C_{11}/\rho}$, $V_T = \sqrt{C_{66}/\rho}$, respectively, where V_L and V_T imply the

phase velocity of the longitudinal and transverse waves. In a common isotropic medium (e.g., aluminum: $\rho = 2700 \text{ kg/m}^3$, $E = 69 \text{ GPa}$, $\nu = 0.33$), $C_{11} = E / (1 - \nu^2) = 77.4 \text{ GPa}$ is always greater than $C_{66} = E / (2 + 2\nu) = 25.9 \text{ GPa}$ and therefore, the longitudinal wave velocity ($V_L = 5355.2 \text{ m/s}$) is always higher than the transverse wave velocity ($V_T = 3099.6 \text{ m/s}$). It can be also confirmed by comparing the two slopes of the gray dashed lines on the ΓX direction of dispersion curve shown in Fig. 3.2a. The steeper gray dashed line represents the longitudinal wave mode of a 1 mm aluminum plate, and the other line represents the transverse wave mode. Note that these lines are marked in the form of two gray-colored dashed circles on EFC.

In this regard, a metamaterial satisfying the condition $C_{11} = C_{66}$ with the EFC shape as shown by the red and blue solid lines in Fig. 3.2b, needs to be designed such that its structure lowers the value of V_L to equal V_T in the ΓX direction of the dispersion curve. Importantly, in a longitudinal wave, particle motion occurs in the x -direction, whereas in a transverse wave, particle motion is in the y -direction. This fact results in a structure based on the idea that waves are hindered while propagating in the x -direction and less affected while propagating in the y -direction. In this sense, a structure is designed by inserting a long rectangular slit in the y -direction, thereby achieving a large reduction of the propagation speed of longitudinal waves and a small reduction in the propagation speed of transverse

waves to lead to equality between V_L and V_T .

3.2.2 Engineered metamaterials

Therefore as shown in Fig. 3.1, an elastic metamaterial plate is engineered so as to have periodically patterned rectangular slits on the 1 mm thick aluminum plate. To satisfy the other condition $C_{16} = C_{26} = 0$ for the targeted EFC shape, a metamaterial unit cell is designed to have horizontal line symmetry. The lattice periods of the metamaterial are $L_x = 3.5$ mm and $L_y = 5$ mm in the x - and y -directions, respectively. The width and height of the slit are $S_w = 0.7$ mm and $S_h = 2.7$ mm, respectively, and the gap between adjacent slits in the x -direction is $S_d = 2.0$ mm. The unit cell geometric parameters are fine-tuned to obtain the effective stiffness tensor to implement the required EFC shape. This proposed metamaterial enables the quasi-longitudinal wave mode (blue square line) and quasi-transverse wave mode (red circle line) to meet in the targeted frequency band between 60 kHz and 120 kHz, as shown in Fig. 3.2a. On the EFC plot two types of wave sheets can be seen to intersect on the k_x axis, as shown in Fig. 3.2b.

Furthermore, this study calculates the effective property at 10 kHz intervals in the targeted frequency band by using the S-parameter retrieval method [49] to confirm

whether the conditions $C_{11} = C_{66}$ and $C_{16} = C_{26} = 0$ are satisfied in the designed metamaterial. The metamaterial satisfies the required conditions, as evident from Table 3.1. The value of an effective property can be found by approximating a thin three-dimensional plate as two-dimensional (2D) plane stress in the long wavelength area. Thus, the effective property values found in this study are obtained based on the metamaterial unit cell under a 2D plane stress condition.

At last we successfully engineer an elastic metamaterial plate showing conical refraction, a special anisotropic characteristic, by only using aluminum, an isotropic homogeneous metal. The proposed structure uses non-resonant-type unit cells to confer the requisite effective property on the metamaterial, thereby achieving a very broad operating frequency bandwidth reaching more than several tens of kHz. Note that because the size of a metamaterial unit cell is approximately 0.13λ at a frequency of 90 kHz, the effective medium theory can be applied effectively to this study.

3.3 Numerical simulations for conical refraction of elastic waves

3.3.1 Wave propagation simulations

Wave deflection based on conical refraction, occurring only in a few anisotropic medium, is achieved by inserting the designed elastic metamaterial into an aluminum plate. An elastic stress wave, normally incident on the engineered metamaterial, is deflected upward and downward at an angle of θ_d . In this case, either the longitudinal wave or transverse wave can be deflected from the metamaterial. Thus, the center area behind the metamaterial can be designated as a safety zone that is unaffected by an elastic wave accompanied by stress, as shown in Fig. 3.1b.

To verify the conical refraction of elastic waves, this study establishes the simulation model described in Figs. 3.3(a) and 3.3(d). We analyze the simulation of harmonic wave propagation by using finite element software COMSOL Multiphysics. Plane wave sources of longitudinal waves (L-wave, $\lambda_L = 59.5$ mm) or transverse waves (T-wave, $\lambda_T = 34.4$ mm) at 90 kHz are normally incident in the x -direction. To absorb boundary reflection on both the right-end and left-end boundaries, Perfectly Matched Layers (PMLs) are applied. The vertical source length is set at 250 mm and equivalent to approximately $4\lambda_L$. Figs. 3(b) and 3(e)

show the simulation results with the normalized von Mises stress field. The white solid box is the area in which the metamaterial is installed, composed of 12800 unit cells (80×160 unit cells). Accordingly, the metamaterial is 280 mm wide and 800 mm high.

We can confirm that normally incident waves are deflected at the angle of $\theta_d = 37.9^\circ$. Note that the propagating direction of elastic waves after exiting the metamaterial slab is still initial x -direction. Furthermore, the elastic waves undergo translocation, into either the upper or the lower path after passing the metamaterial whereas the elastic waves propagated horizontally at the center of the plate before entering the metamaterial. The effect of elastic stress waves on the center area behind the metamaterial is minimized because of the installation of the engineered metamaterial; otherwise, the waves would have fully impacted the safety zone.

On the other hand, replacement of the engineered metamaterial area, corresponding to the white solid box, by an effective medium, the same simulations show the equivalent performance, as shown in Figs. 3.3(c) and 3(f). The white dashed box represents the effective medium area with the values of the effective property at 90 kHz in Table 3.1. The width and height of the area are not changed by the replacement. As a result, the waves are confirmed to have been conically deflected at the angle of θ_d , as the case of direct insertion of the designed metamaterial. We

hereby identify that the metamaterial having required anisotropy is tested to be capable of wave translocation based on conical refraction.

Additionally, this study conducts a simulation of time transient analysis with the designed metamaterial. The findings correspond to the results from the simulation of harmonic wave propagation (See Chapter 4.). The simulation clearly explains the progress of wave propagation, deflecting inside the metamaterial by conical refraction; and the propagation path of the waves outside the metamaterial. Also, we introduce the power transmission of the incident waves entering the metamaterial slab, quantifying the amount of wave penetration, whose values are reported in the Chapter 4.

3.3.2 Adjusting the deflection angle by altering the anisotropy factor

The deflection angle θ_d of an elastic wave incident on the acoustic axes can be obtained from the EFC of the engineered metamaterial. Our structured metamaterial has a deflection angle $\theta_d = 37.9^\circ$. It is well known that, on the EFC of an anisotropic medium, the curvature of the quasi-longitudinal wave and quasi-transverse wave modes on the k_x axis is adjustable with the anisotropy factor $A = 2C_{66} / (C_{11} - C_{12})$ [25]. Thus, we can propose a system having a different

deflection angle by changing the anisotropy factor for the proposed metamaterial while satisfying the conditions for conical refraction.

First, the conical double point for the metamaterial is required to satisfy the effective stiffness tensor conditions such that $C_{11} = C_{66}$ and $C_{16} = C_{26} = 0$. Let us start from using the effective property of the existing metamaterial at 90 kHz. To adjust the anisotropy factor $A = 2C_{66} / (C_{11} - C_{12})$, we consider an effective medium having a different C_{12} value but fixed C_{11} and C_{66} values. When C_{12} happens to be $C_{12} = 1.994 \times 10^9$, the deflection angle from the EFC is obtained as $\theta_d = 30.6^\circ$. On the EFC shown in Fig. 3.2(b), the curvature on the k_x axis should be deformed as a consequence of the changes in the anisotropy factor. Here we introduce the numerical simulation result as shown in Fig. 3.4(a). The setting for the simulation is identical with the one in Fig. 3.3. A 90 kHz L-wave is incident on the effective medium having an effective property of $C_{12} = 1.994 \times 10^9$. The deflection angle is confirmed as $\theta_d = 30.6^\circ$, which is less than $\theta_d = 37.9^\circ$ of the previously engineered metamaterial. Because the current case satisfies the condition of $C_{11} = C_{66}$ and $C_{16} = C_{26} = 0$, it shows the performance that the elastic waves are conically refracted and translocated after passing through the metamaterial slab. The only change is the deflection angle, and thus the explanations in Section 3.3.1 are all applicable to the current model.

Fig. 3.4(b) shows the case in which the 90 kHz L-wave is normally incident on the effective medium having an effective property of $C_{12} = 9.994 \times 10^9$. The other components are equivalent to those for the existing metamaterial at 90 kHz. Because this case still satisfies the conditions for the occurrence of conical refraction, the elastic waves are multi-directionally deflected despite their normal incidence. Furthermore, the deflection angle is much widened and confirmed as $\theta_d = 44.0^\circ$ according to the changed anisotropy factor. Further studies on the configuration of the metamaterial unit cell will be subsequently introduced for various deflection angles.

Our proposing metamaterial system is expected to be useful by placing it an appropriate location to protect the zone where the mechanical stress waves can be fatal. The engineered metamaterial with a deflection angle of $\theta_d = 37.9^\circ$ can have a safety zone of about 0.1859 m. The size of this safety zone can be explained from the numerical simulations in Fig. 3.3. The vertical size of the safety zone can be determined using the width and deflection angle of the metamaterial slab with the relation as following: $2 \times \text{width of AEMM} \times \tan \theta_d - \text{width of source}$. Of course, the larger the width of the metamaterial slab, the greater the vertical size of the safety zone. However, it is meaningful to explain the size of the safety zone for various deflection angles based on the fixed metamaterial slab width satisfying the Fabry-Perot resonance condition ($kd = n\pi$). In Fig. 3.3 and Fig. 3.4, the width of

metamaterial slab is fixed with 0.28 m. Thus, when the deflection angle is $\theta_d = 30.6^\circ$, the vertical size of the safety zone is 0.0812 m. When the deflection angle is $\theta_d = 44.0^\circ$, the vertical size of the safety zone is 0.2908 m.

3.4 Experimental demonstration of metamaterials

3.4.1 Experimental procedure

The experiment shown in Fig. 3.5(a) is established to test the effectiveness of the engineered elastic metamaterial, which is microfabricated onto an aluminum plate with dimensions of $2400 \times 1200 \times 1$ mm by using a laser-cutting machine (TRUMPF TruLaser 5030 fiber). The metamaterial is patterned with 80×160 unit cells in both the x - and y -directions, respectively. The circumstance is equivalent to the simulation model shown in Fig. 3.3. The metamaterial is 280 mm wide and 800 mm high and located at the center of the aluminum plate. A zoomed-in view of the actually fabricated metamaterial is shown in the right panel of Fig. 3.5(a), and this metamaterial is elaborately manufactured nearly error free as engineered.

A transmitter is used for wave excitation by placing a coil and magnet on a nickel patch bonded to a plate. Elastic waves are generated along the plate due to the mechanical deformation of the patch based on the magnetostriction effect [50-52]. Two transmitters elongated in the y -direction [53] are used to excite the plane wave, reaching a size of 250 mm. Each transmitter generates L-wave or T-wave, and is packaged by changing the configuration of their magnet and coil, respectively. They are installed at distances of $L_L = 4\lambda_L = 238$ mm and $L_T = 4\lambda_T = 138$ mm from the entrance of the manufactured metamaterial. Note

that the excitation locations L_L and L_T of waves are identical with the setting in simulations in Fig. 3.3.

To demonstrate the translocation of waves after passing the structured metamaterial, the wave signals are measured while moving the receiver, at 17 measurement points that are distributed 50 mm wide above the vertical line 100 mm away from the exit of the metamaterial. Two types of receivers are used to collect the L-waves and T-waves, respectively. This characterized experimental environment is shown in Fig. 3.5(b).

The excitation Gabor pulse signals used for the experiment are generated by a function generator (Agilent Technologies 33220A). They are amplified by a power amplifier (T&C Power Conversion AG1017L) before being sent to the transmitters. The Gabor pulse signals centered at 90 kHz are represented as amplitude by time, shown in the upper panel of Fig. 3.5(c). Then, the signals measured by the receiver are amplified through a pre-amplifier (Stanford Research Systems SR560) and measured as shown in the middle and lower panels of Fig. 3.5(c).

A detail flowchart of the experimental procedure can be explained with images of laboratory equipment. Fig. 3.6(b) shows the essential equipment for conducting experiments in this study. A function generator (Agilent Technologies 33220A) is a device that is used to excite various shapes of sources such as Gabor, sine, rectangular pulses. We send a source signal to a transmitter by primarily selecting

signal information such as frequency and burst period. Fig. 3.6(a) is an experimental flowchart showing the overall procedures by which the generated signals are transmitted by the transmitter and the signals measured by the oscilloscope are analyzed. Wave signals generated from the function generator pass a power amplifier (T&C Power Conversion AG1017L) before entering the transmitter to produce sufficient signal intensity. An adequate amplification ratio is selected according to the content of experiment. The waves sent to the transmitter propagate along a plate, and scattered signals affected by the structure configuration inside the plate reach the receiver. These measured signals are amplified by the pre-amplifier (Stanford Research Systems SR560) and finally sent to the oscilloscope.

The metamaterial plate used in the experiment is fabricated according to the dimensions shown in Fig. 3.7. The metamaterial composed of 12800 unit cells is located at the center of the aluminum plate, 2500 mm wide and 1200 mm high. A sufficiently large size of a plate is considered to absorb the boundary reflection effect coming from the left- and right-end boundary. Because the study uses a 250 mm long source to satisfy the plane wave condition, the proposed metamaterial is patterned with 80×160 unit cells to allow for a sufficient width and height for testing the performance of that metamaterial.

The output signals measured by the oscilloscope are the voltage amplitude as a

function of time. Two types of receivers are capable of measuring either an S_0 wave or SH_0 wave, respectively. They can categorize the measured signals into two subgroups. Fig. 3.8 and Fig. 3.9 show experimental raw data by using the S_0 wave receiver at 17 measuring points. The signal highlighted in blue color near $190 \mu s$ is measured immediately after passing the metamaterial and the most intense signals are measured near points #4 and #14. However, few signals are measured at point #9, at the center of the plate. The signals detected after $500 \mu s$ denote the reflected waves caused from the outer boundary and are not used for signal processing. The experimental results for demonstration of the conical deflection, shown in Fig. 3.12(a), can be obtained after undergoing the STFT process with these 17 signals.

The SH_0 wave also occurs after passing the metamaterial slab even in the case that the S_0 wave is excited by a transmitter. Experimental raw data measured by the SH_0 wave receiver confirms this occurrence as shown in Fig. 3.10 and Fig. 3.11. The signals highlighted in red color near $200 \mu s$ are measured after passing the metamaterial, and as with the S_0 wave, the most intensive signals are measured near points #4 and #14.

3.4.2 Short-time Fourier transform results

Now, we explain the experimental results that how elastic waves of 90 kHz can be deflected and translocated through the manufactured elastic metamaterial. Fig. 3.12 shows a plot of the Short-Time Fourier Transform (STFT) by using measured data from a receiver. Figs. 3.12(a) and 3.12(b) are the results of experimental models where waves are excited by an L-wave transmitter and measured by an L-wave or T-wave receiver. Figs. 3.12(c) and 3.12(d) are the results of the experimental models where the waves are excited by the T-wave transmitter and measured by the L-wave or T-wave receiver. These plots confirm that waves normally incident on the metamaterial appear at the translocated position after passing the metamaterial. Thus, wave measurements are rarely obtained at measure point #9 (central area); wave measurements are dominant near points #5 and #13 where waves propagate along the path transferred by conical refraction of the metamaterial. Furthermore, both L- and T-wave modes propagate after exiting the metamaterial even in the case that either the L-wave or T-wave enters the metamaterial. Such proposed metamaterials are applicable to various wave-use devices because the metamaterial can translocate the paths of elastic waves and facilitate wave propagation with mode conversion.

The arrival time of a signal reaching the receiver can be calculated by considering the wave propagation velocity inside and outside the metamaterial. In the long-wavelength area, the phase velocity of waves propagating along a plate is nearly

equivalent to the group velocity, an energy propagation velocity. Thus, V_L and V_T can be determined from the effective property values at the frequency of 90 kHz reported in Table 3.1. Of course, the wave propagation velocity inside the metamaterial can be obtained from the slope of the dispersion curve shown in Fig. 3.2(a). Using this, the energy propagation velocity of the elastic waves inside the metamaterial is obtained as 2295 m/s. In a homogeneous aluminum plate, the group velocity of an L-wave and T-wave is $V_L = 5355.2$ m/s and $V_T = 3099.6$ m/s, respectively. The arrival time of elastic waves from a transmitter through a propagation path to a receiver is now calculated based on these velocity values. The calculated arrival time is nearly close to the time measured in the time domain of the STFT results shown in Fig. 3.12; $t_{arrival} = 217.7 \mu s$ in Figs. 3.12(a) and 3.12(c), $t_{arrival} = 231.3 \mu s$ in Figs. 3.12(b) and 3.12(d). The results can be compared to and demonstrated with the results from a simulation of time transient wave propagation, described in Chapter 4.

When the wavenumber k of elastic waves and the width d of the metamaterial slab satisfy the Fabry-Perot resonance condition, $kd = n\pi$ where n is a positive integer value, the extent of wave transmission passing the metamaterial slabs is maximized. The width of the metamaterial slabs used in this study is 280 mm,

which is very close to $d = 280.5$ mm satisfying the Fabry-Perot resonance condition for elastic waves at 90 kHz.

3.4.3 Wide operating frequency range of metamaterials

The proposed metamaterial in this study is advantageous because the metamaterial is designed based on a non-resonant type, and thereby, the operational frequency range is broad. Seen from the dispersion curve and EFC in Fig. 3.2, the targeted performance is confirmed in the range from 60 kHz to 120 kHz. Furthermore, as shown in Table 3.1, the anisotropy conditions, $C_{11} = C_{66}$ and $C_{16} = C_{26} = 0$, are satisfied in the frequency range of interest. Fig. 3.12 already shows the experimental results at 90 kHz, indicating that the experimental results correspond with those obtained in the simulation. Additionally, we verify that the deflection and translocation performance of elastic stress waves are well implemented in the frequency range, the area in Fig. 3.2(a) highlighted in green.

Here, the superior performance of the structured metamaterial is experimentally verified with 60 kHz and 120 kHz elastic waves. Figs. 3.13(a) and 13(b) show the experimental results from the excitation of either the 60 kHz L-wave or T-wave. The same experimental setting, denoted in Fig. 3.5, is used to measure the signal data and conduct the Short-Time Fourier Transform. The proposed metamaterial

can explain wave translocation of 60 kHz elastic waves. Furthermore, the experimental results with the 120 kHz elastic wave support the conical refraction performance of the proposed metamaterial, as shown in Figs. 3.14(a) and 14(b). Accordingly, this study experimentally prove that the engineered metamaterial composed of non-resonant unit cells operates in a broad frequency range. In previous studies on designing the metamaterial, targeted wave propagation characteristics were implemented by employing metamaterials using resonant type unit cells to achieve the target effective property. Thus, they have exhibited a narrow operational frequency range. However, the metamaterial in this study can attract huge attention because this metamaterial is a system with a wide operating frequency range, overcoming the existing drawback.

3.5 Selection of the travel path in engineered metamaterials

Thus far, we have examined that elastic stress waves normally incident on engineered metamaterials are conically deflected. At the next part of examination, we introduce that the same metamaterial can implement a function to pass waves in one direction and stop waves in the other direction. As shown in schematic diagram of Fig. 3.1(b), the engineered metamaterial can select the path of wave propagation among two newly created paths inside the metamaterial. If this is true, installation of our proposed metamaterial in front of a zone would cause waves to detour around the zone, which would be protected against mechanical stress waves.

The metamaterial used here has the same unit cells as those of the previously designed metamaterial in Fig. 3.1(a). However, we exploit a special phase relationship between the longitudinal waves and transverse waves propagating inside the metamaterial. If the L-wave is incident on the metamaterial slab, conically deflected waves have both L-wave and T-wave modes. They propagate along two newly created paths inside the metamaterial. Then, the phase of the T-wave mode on one path is opposite to that of deflected waves on the other path, whereas the phases of L-wave modes are the same each other. Likewise, if the T-wave is incident on the metamaterial slab, the phase of the T-wave mode on one path is the same as that of the deflected waves on the other path, whereas L-wave modes have the opposite phases each other. This phase characteristic can be explained and verified by simulations and experiments, the results of which are

reported in Chapter 4.

Using the above mentioned phase characteristic, we can select the path of wave propagation among two paths inside the metamaterial by generating destructive interference along either of two paths. A numerical simulation and an experiment are conducted to test this finding, as shown in Fig. 3.15. Fig. 3.15(a) corresponds to the simulation results for the case in which the L-wave and T-wave are simultaneously excited at distances of L_L and L_T , respectively. The excited L- and T-waves simultaneously reach the entrance of the metamaterial. In this case, because the L-wave and T-wave propagating along the upper path undergo destructive interference, stress waves propagate only along the lower path, rather than the upper path, as shown in Fig. 3.15(a). The results indicate that elastic waves, propagating at the center of a plate in the beginning, are moved downward after passing the metamaterial slab. Also, elastic waves would only be able to pass along the upper path by shifting the phase of the T-wave source by π when initially setting the excitation. It is explained in Fig. 3.15(d). In this case, the L-wave and T-wave still reach the entrance of the metamaterial simultaneously. However, the destructive interference appears at the lower path, thereby allowing elastic waves to pass only along the upper path. Such selective propagation is excellently confirmed in the simulation results, shown in Figs. 3.15(a) and 15(d).

Now, the experimental results for selective propagation are demonstrated in Figs.

3.15(b), 15(c), 15(e) and 15(f). All the experimental settings are the same as those used for verifying the conical refraction in Fig. 3.5. The only difference here is that the two transmitters generating the L-wave and T-wave are simultaneously excited. The STFT results in Figs. 3.15(b) and 15(c), confirm that the manufactured metamaterial permits waves to pass only along the lower path. Thus, wave measurements are dominant near measure point #5. On the other hand, we can change the path of appearing the destructive interference by shifting the phase by π when exciting the T-wave transmitter. Note that when it comes to the L-wave transmitter, its setting is unchanged. As shown in Figs. 3.15(e) and 15(f), these figures explain that elastic waves pass only along the upper path and that the destructive interference occurs along the lower path. In this case, wave measurements are dominant near measure point #13. Through our findings, we can say that the structured metamaterial is capable of translocating the position of wave propagation as if being teleported.

Here, another unique wave propagation system can be designed by using the fact that elastic stress waves can be unidirectionally deflected inside the metamaterial. Deploying the metamaterial slab twice would return the elastic waves to their initial location. First, as shown in Fig. 3.16(a), let us consider the safety zone that should be protected from mechanical stress waves. This zone is located at the center of an isotropic aluminum plate and is 100 mm wide and 200 mm high. When elastic waves incident on this safety zone, it is unavoidable that the zone is directly

affected by elastic waves. However, as shown in Fig. 3.16(b), if the metamaterial proposed in this study were to be installed in front of the safety zone, this would deflect the elastic waves by translocating most of the waves into the upper and lower areas of the safety zone. Subsequently, if another metamaterial slab were to be installed on the behind of the safety zone, the previous translocated waves would be returned to the center of the plate, i.e., to the initial location. The wave propagation characteristics in the second metamaterial slab are easily understandable because we have already examined the method for wave propagation along either the upper or lower path inside the engineered metamaterial.

The process of an excited T-wave source passing through two metamaterial slabs can be described step by step as follows. L- and T-waves after passing the first metamaterial slab encounter the second metamaterial slab while detouring around the safety zone. When waves propagating in the detour above the safety zone enter the second metamaterial slab, they travel only in a downward direction. Conversely, when waves propagating in the detour below the safety zone enter the second metamaterial slab, they travel only in an upward direction. As a result, the elastic waves initially propagating at the center of the plate can be returned to the center. Fig. 3.16(b) presents the simulation results where T-waves at 90 kHz are excited 100 mm before the first metamaterial slab. The two areas represented by the white dashed box denote effective medium that use effective property values at 90 kHz.

For this metamaterial area, $L_{MM} = 280$ mm and 800 mm are used as they have been. Importantly, the length of L_C , the gap between the two metamaterial slabs, has to be carefully considered. A simulation is conducted by carefully setting $L_C = 286.2$ mm, satisfying that waves in the upper and lower area of the second metamaterial slab undergo downward and upward deflections, respectively.

An impedance difference occurs at the boundary of the metamaterial slab because there is a difference between the effective property of the engineered metamaterial and the material property of aluminum. Because of this difference, the transmission values of waves passing through the metamaterial are below a certain value, as reported in the Chapter 4. If the waves were to pass through the metamaterial slabs twice, the transmission values would decrease significantly. Accordingly, such low transmission values may restrict applications in which transmitted waves return to the center. That restriction is only expected when multiple metamaterial slabs are used. Of course, there is no doubt that the currently proposed metamaterial is a highly reproducible structure permitting successfully translocating elastic waves.

3.6 Summary

This study implements an elastic metamaterial capable of forming acoustic axes where the phase velocities of two wave modes are equal, occurring only in a special anisotropic medium. The study thoroughly describes the process of inducing a structural configuration to meet the effective stiffness condition required for a metamaterial. As a result, the study elaborately designs a refined metamaterial only by using an isotropic aluminum metal. The study successfully demonstrates, by numerical simulation and experiments, that the engineered metamaterial exhibits the phenomenon of conical deflection of stress waves. Furthermore, the study proposes and examines a method for implementing a unidirectional wave deflection by satisfying the destructive interference conditions of longitudinal and transverse wave modes along only one path inside the metamaterial. Our findings are innovative in terms of manipulating the direction and location of wave propagation. The engineered metamaterial is capable of translocating spatial locations of waves. The operational performance of the proposed metamaterial is advantageous because the metamaterial can be used in a broad frequency band. This achievement is possible because the unit cells in this study are designed based on non-resonant type unit cells. Therefore, we hereby propose an innovative system to change the propagation paths of mechanical stress waves. This wave-controlling technique advances the fields of nondestructive testing, ultrasonic imaging techniques, structural health monitoring and a novel type of cloaking application.

Table 3.1 Effective density and effective stiffness tensor of the elastic metamaterial for the frequency range from 60 kHz to 120 kHz.

frequency (kHz)	ρ (kg/m ³)	C_{11} (GPa)	C_{12} (GPa)	C_{22} (GPa)	C_{66} (GPa)	C_{16}, C_{26} (GPa)
60	2070	10.99	6.23	50.66	10.98	0
70	2057	10.9	6.171	50.34	10.89	0
80	2045.6	10.81	6.084	50.15	10.80	0
90	2035.7	10.72	5.994	50.04	10.72	0
100	2026.3	10.64	5.921	49.89	10.64	0
110	2018.7	10.56	5.846	49.81	10.55	0
120	2014.8	10.5	5.787	49.85	10.48	0

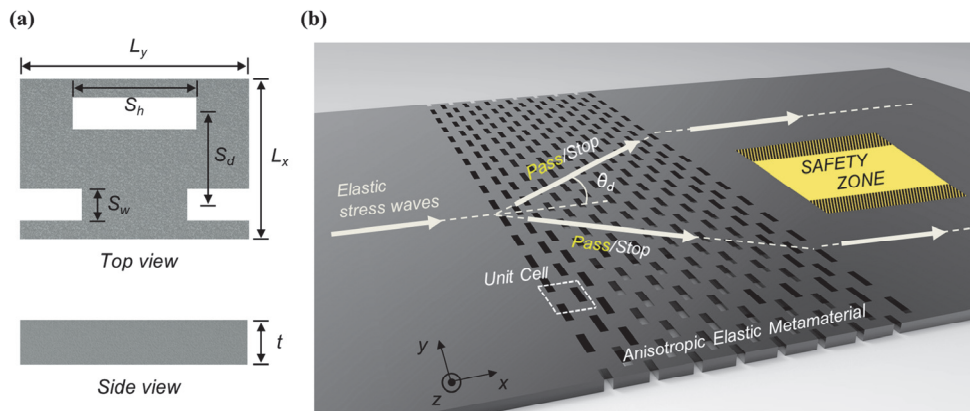


Figure 3.1 The engineered anisotropic metamaterial unit cell and the elastic stress wave propagation along the metamaterial plates. (a) Unit cell dimensions of the structured anisotropic metamaterial plate. (b) Translocation of normal incident elastic waves, both upward and downward. The center of behind the metamaterial where the elastic stress waves cannot reach is designated as safety zone.

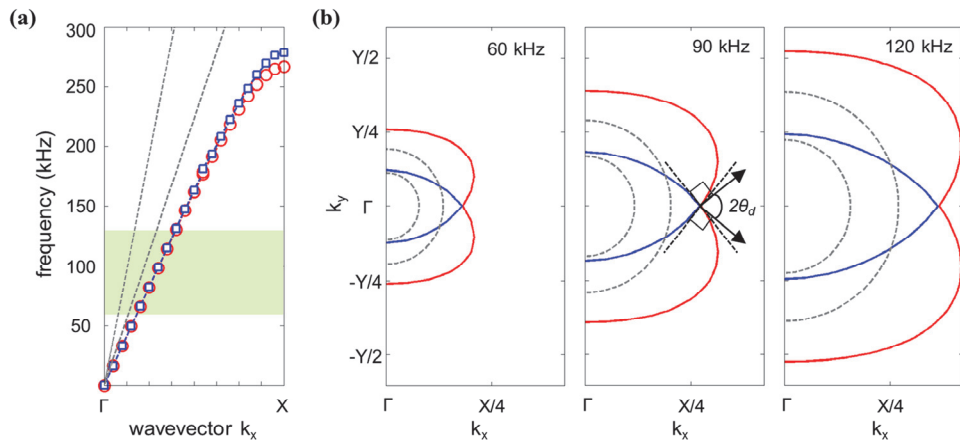


Figure 3.2 Dispersion curve and equi-frequency contours for the engineered metamaterial plate. (a) Dispersion curve along Γ X direction for the proposed metamaterial. (b) Equi-frequency contours at 60, 90 and 120 kHz for elastic metamaterial plate.

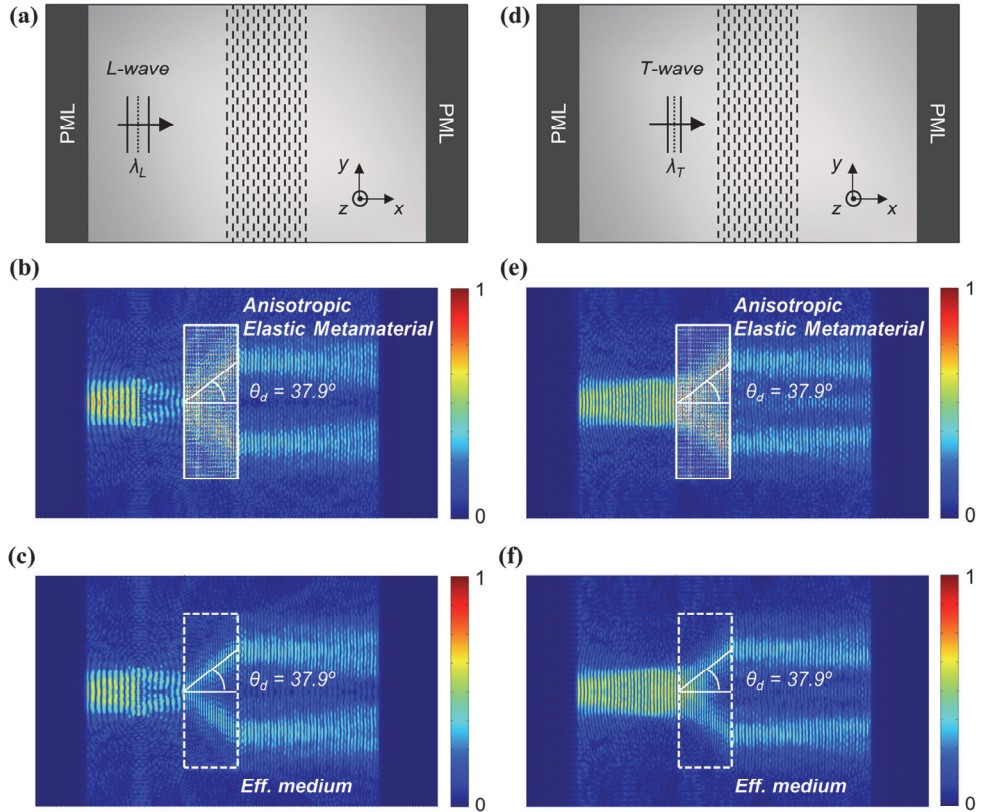


Figure 3.3 (a) Simulation model for 90 kHz longitudinal wave incident case. (b,c) Normalized von Mises stress field distribution for (b) the engineered metamaterial and (c) effective medium. (d) Simulation model for 90 kHz transverse wave incident case. (e,f) Normalized von Mises stress field distribution for (e) the engineered metamaterial and (f) effective medium.

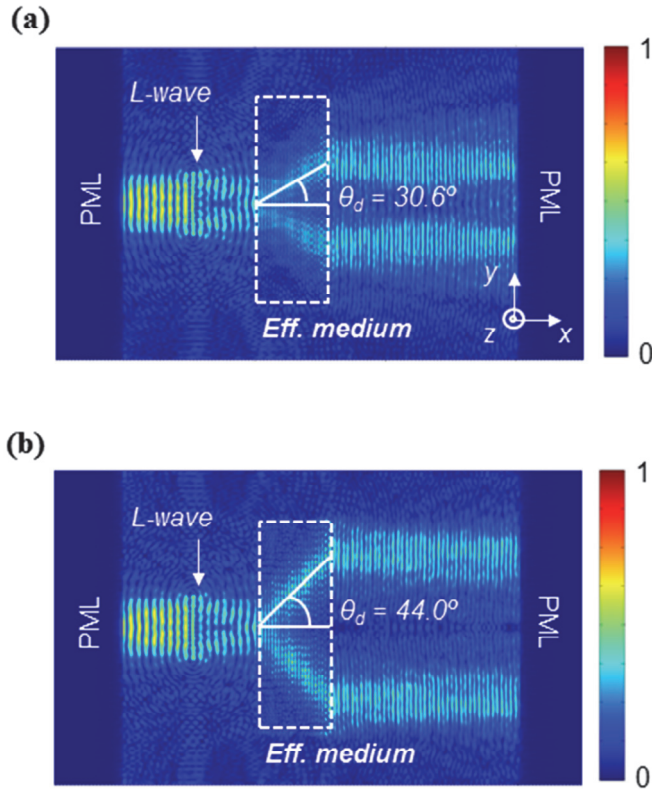


Figure 3.4 Adjusting the deflection angle by changing the effective elasticity tensor. Normalized von Mises stress field distribution for 90 kHz longitudinal wave incident case (White dashed box: the region for the effective medium of (a) $C_{12} = 1.994 \times 10^9$ Pa and (b) $C_{12} = 9.994 \times 10^9$ Pa).

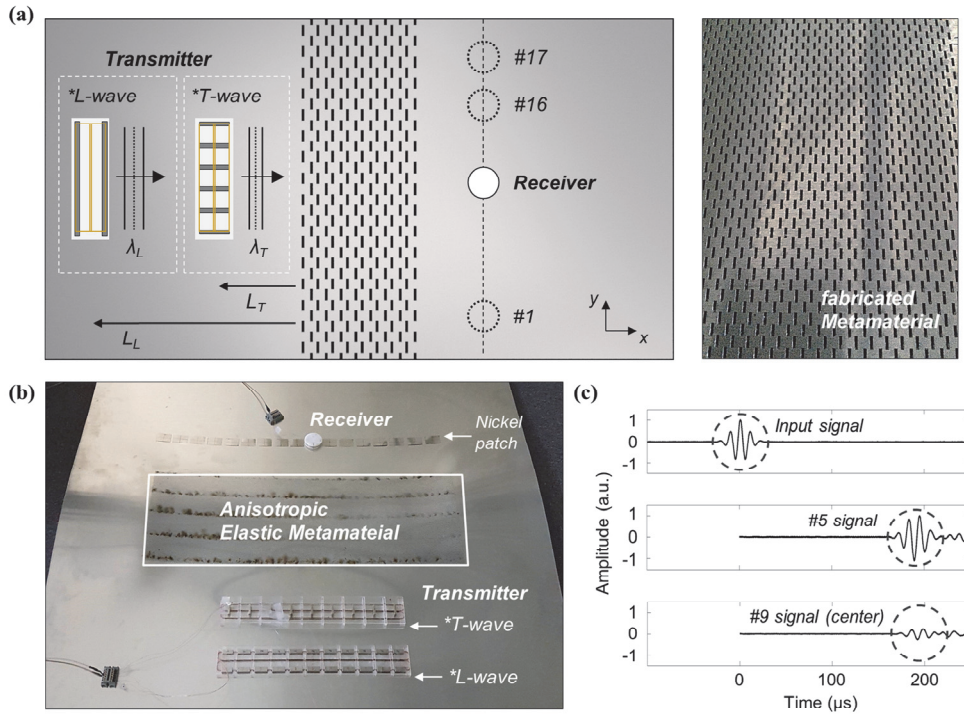


Figure 3.5 Experimental set-up for evaluating the performance of the structured elastic metamaterial plate. (a) Schematic diagram of experimental measurement system (left) and zoomed-in view of the fabricated metamaterial (right). (b) Actual set-up of the experiment. (c) Generated 90 kHz input Garbor pulse signal and measured signal at point #5 and #9.

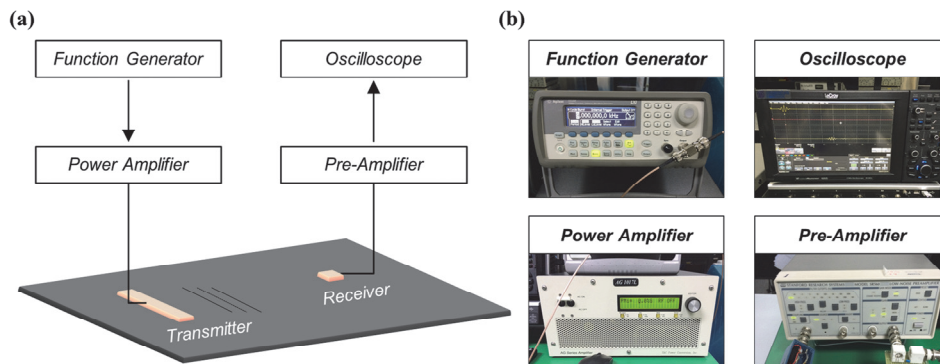


Figure 3.6 Experimental set-up for wave generation and measurement system. (a) Schematic diagram of experimental measurement system. (b) Experiment equipment: function generator, power amplifier, pre-amplifier, oscilloscope.

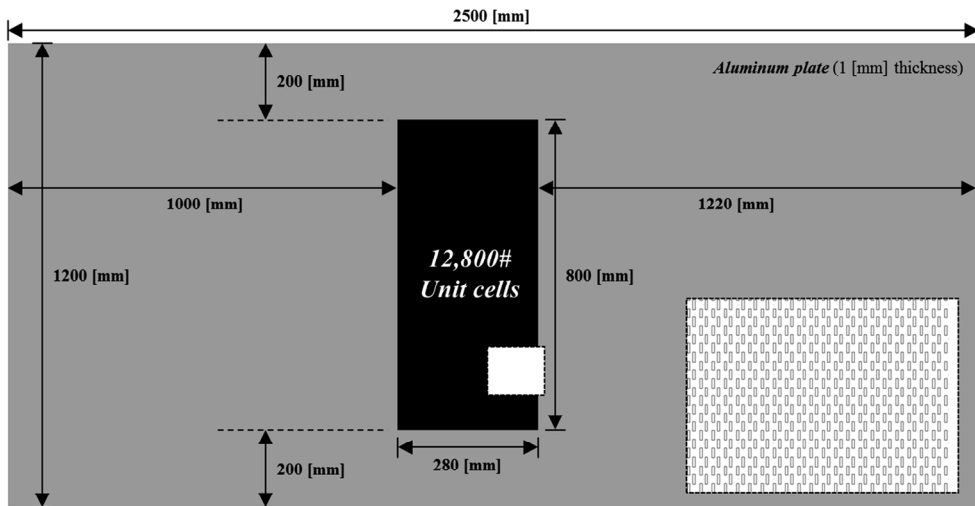


Figure 3.7 Geometric dimension of the manufactured plate.

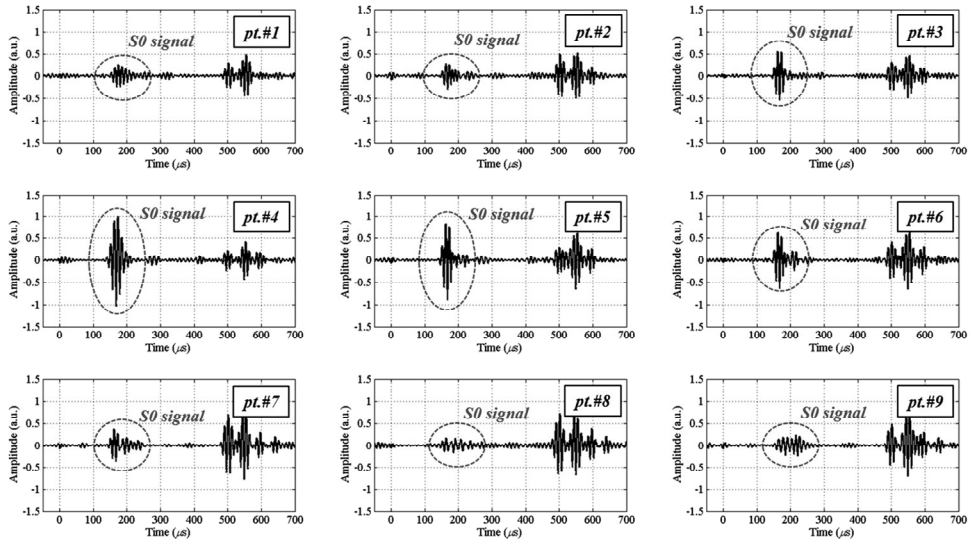


Figure 3.8 Experimental raw data at the measuring points from #1 to #9. This data is for the case of S_0 wave transmitter and S_0 wave receiver.

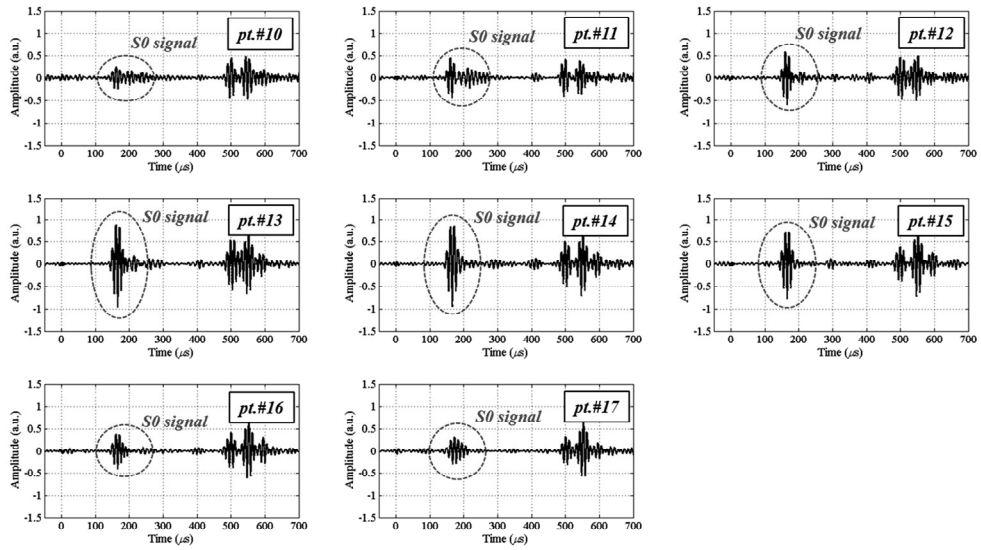


Figure 3.9 Experimental raw data at the measuring points from #10 to #17. This data is for the case of S_0 wave transmitter and S_0 wave receiver.

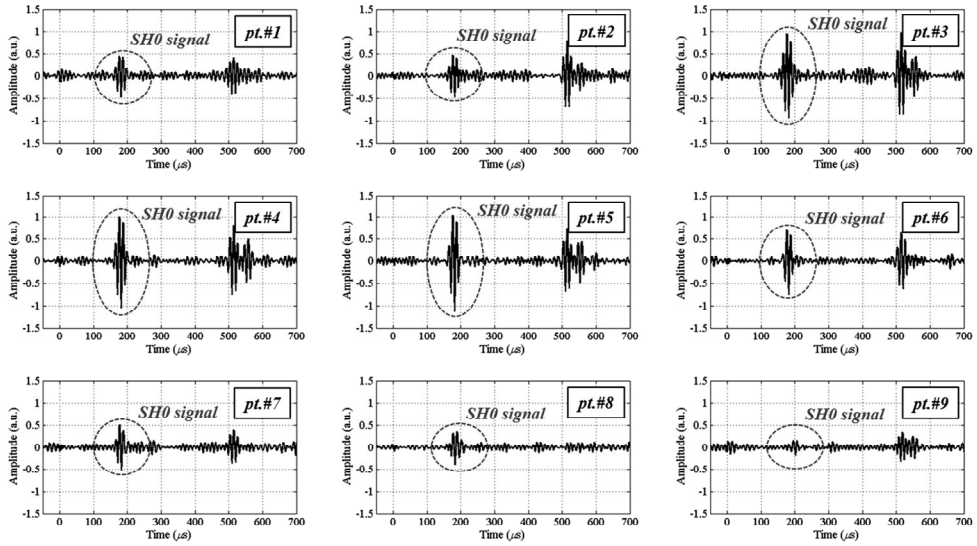


Figure 3.10 Experimental raw data at the measuring points from #1 to #9. This data is for the case of S_0 wave transmitter and SH_0 wave receiver.

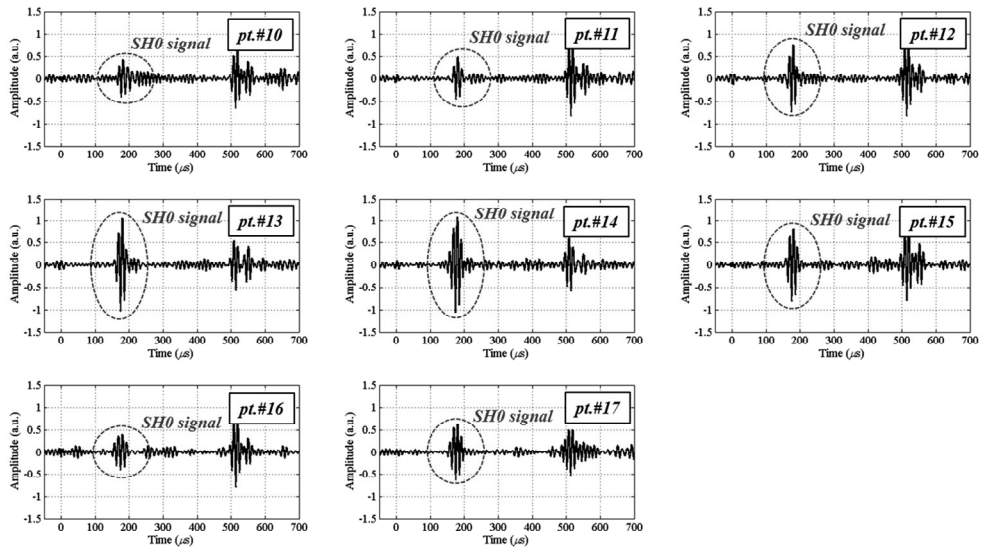


Figure 3.11 Experimental raw data at the measuring points from #10 to #17. This data is for the case of S_0 wave transmitter and SH_0 wave receiver.

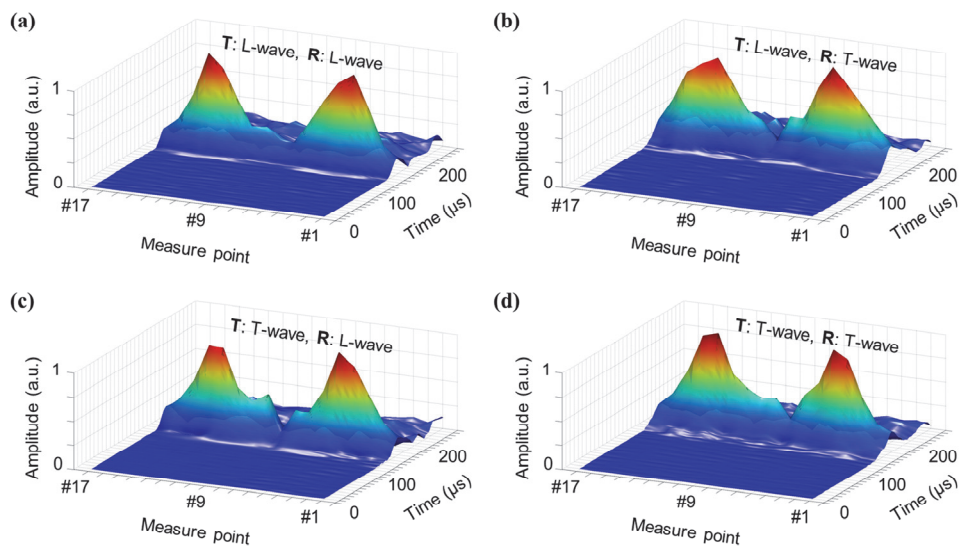


Figure 3.12 Short-time Fourier transform results using experimental data. (a,b) Case for 90 kHz longitudinal wave transmitter and (a) longitudinal wave or (b) transverse wave receiver. (c,d) Case for 90 kHz transverse wave transmitter and (c) longitudinal wave or (d) transverse wave receiver.

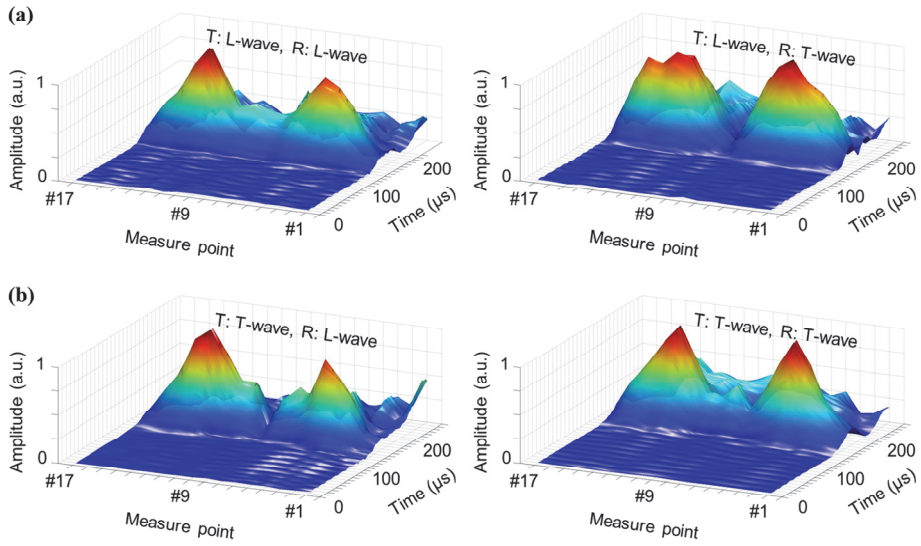


Figure 3.13 Short-time Fourier transform results using experimental data. (a) Cases for 60 kHz longitudinal wave transmitter and longitudinal wave receiver (left) or 60 kHz longitudinal wave transmitter and transverse wave receiver (right). (b) Cases for 60 kHz transverse wave transmitter and longitudinal wave receiver (left) or 60 kHz transverse wave transmitter and transverse wave receiver (right).

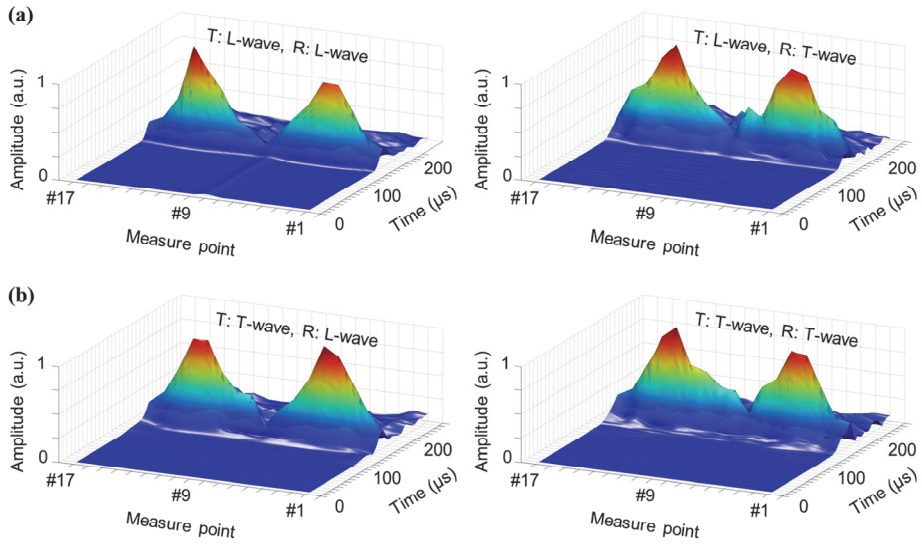


Figure 3.14 Short-time Fourier transform results using experimental data. (a) Cases for 120 kHz longitudinal wave transmitter and longitudinal wave receiver (left) or 120 kHz longitudinal wave transmitter and transverse wave receiver (right). (b) Cases for 120 kHz transverse wave transmitter and longitudinal wave receiver (left) or 120 kHz transverse wave transmitter and transverse wave receiver (right).

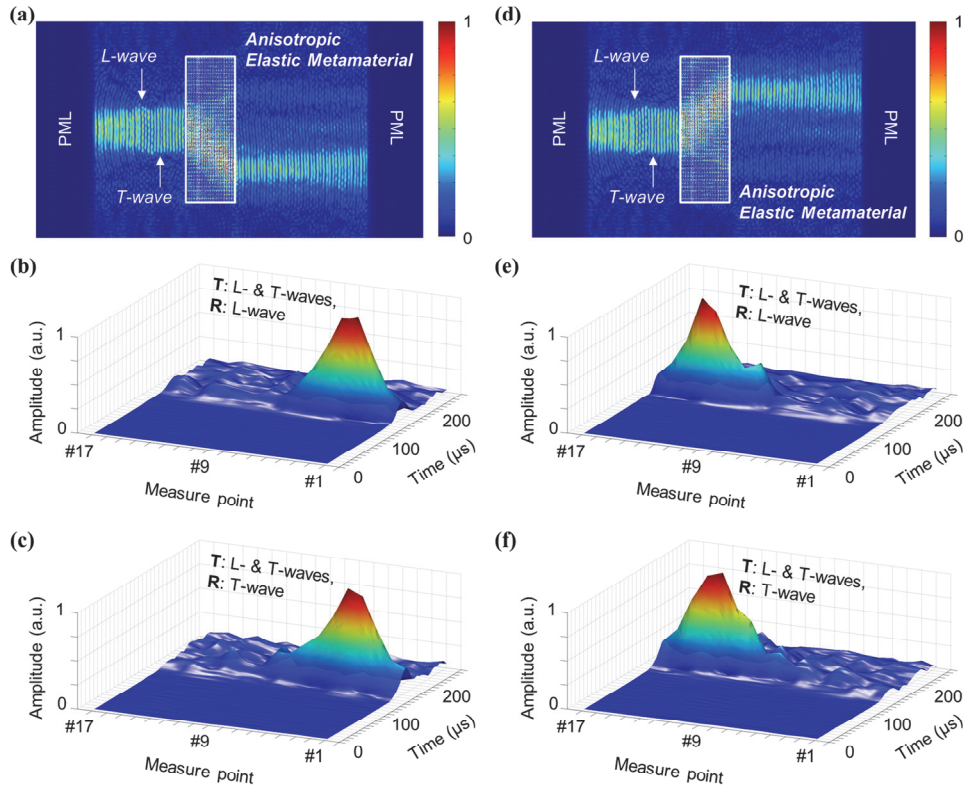


Figure 3.15 Wave path choice by tuning the phase of two transmitters. (a) Simulation result for simultaneous excitation of transmitters for 90 kHz longitudinal wave and transverse wave. (b,c) Experimental STFT results for the situation in a. (d) Simulation result for simultaneous excitation of transmitters for 90 kHz longitudinal wave and transverse wave. Setting is identical with **a** except for transmitter for transverse wave set-up to have an opposite phase to the one in **a**. (e,f) Experimental STFT results for the situation in **d**.

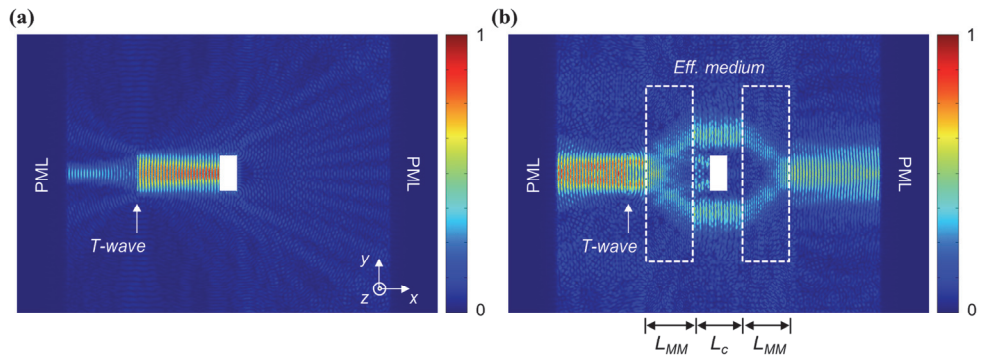


Figure 3.16 Defense of safety zone against normal incident elastic stress waves with and without the engineered anisotropic metamaterials. (a) Numerical simulation result when transverse wave incident normally on safety zone. (b) Additional two metamaterials having the horizontal length L_{MM} are placed in front and back of the safety zone with a distance of L_c .

CHAPTER 4

IN-DEPTH ANALYSIS ON ENGINEERED METAMATERIALS

4.1 Overview

Regarding the wave propagation path, a certain system capable of dramatically deflecting waves can be versatile in terms of changing the travel path of the waves. Periodic structures showing the birefringence property have played a key role in manipulating the travel path. When a wave is angularly incident on periodic structures such as sonic [53], photonic [54] and phononic crystals [55], a wave can be refracted in crystal structure with two or more waves. At this point, negative refraction is very crucial phenomenon, and the theoretical possibility of negative refraction has been first reported a few decades ago [56]. Since then, experimental verification of negative refraction has been completed in phononic crystal [4, 57],

photonic crystals [58] and an elastic metamaterial [59]. Furthermore, with using a metasurface [60], one can implement negative refraction by controlling a wave front without using the birefringence characteristic. So far, negative refraction phenomenon has been a stepping stone for various studies on metamaterials showing tremendous ability.

Previously in Chapter 3, the anisotropic elastic metamaterial with conical refraction phenomenon is newly proposed and examined the direction control performance on normally incident waves. The conical refraction can be innovatively exploited to control the travel direction of normally incident waves whereas the birefringence property can be simply used to control angularly incident waves. This chapter introduces additional interpretations for an in-depth understanding of our proposed elastic metamaterial. We explain the effect on the EFC by changing the geometric dimension of the slits and the transient analysis results on the engineered metamaterial. Furthermore, we analyze the phase information of elastic waves propagating after passing the metamaterial slab. Using this phase characteristic, a system capable of detouring the safety zone is already proposed in Chapter 3. Here in this chapter, additional numerical simulation is conducted by making several situations that the safety zone is made in various sizes.

4.2 The effect of metamaterial geometry perturbation

The dispersion curve of the proposed metamaterial unit cell was introduced as shown in Fig. 3.2. This is for waves propagating along the x direction in the metamaterial, and its wave vector has only an k_x component. If a wave enters in the y or 45-degree axis directions toward the metamaterial, the conical refraction phenomenon cannot be exploited. To explain this, the dispersion curves in the ΓY and ΓM directions are denoted in Fig. 4.1. For the dispersion curve in the ΓX direction, as shown in Fig. 3.2, the phase velocities of the quasi-longitudinal wave and quasi-transverse wave coincide below about 150 kHz, which is an indicator that an important condition for implementing conical refraction is satisfied. On the other hand, the dispersion curves in the ΓY and ΓM directions confirm that the quasi-longitudinal wave and quasi-transverse wave modes do not intersect. Furthermore, the slope of the quasi-longitudinal wave is steeper than that of the quasi-transverse wave. From these facts, it can be summarized that the conical refraction occurs only in the case where a wave incident on the metamaterial slab along the x direction. The reason for this is because the metamaterial unit cell is constructed with long slits elongated in the y direction to equalize V_L and V_T for waves propagating in the x direction.

The following description shows how five factors determining the geometric dimension of metamaterial unit cells affect the occurrence of conical refraction.

Table 4.1 shows the gap of the inner and outer curves of EFC at the k_x axis when the lattice period along the x direction, L_x , is fine-tuned. The original size of the gap obtained from the geometric dimension of the metamaterial unit cell shown in Fig. 3.1 is numerically measured as 0.4460 rad/m where $L_x = 3.5$ mm, $L_y = 5$ mm, $slitw = 0.7$ mm, $slith = 2.7$ mm and $slitd = 2$ mm. Because the occurrence of conical refraction depends on the degenerated double point at the k_x axis, the gap size is required to converge to numerically almost zero.

Table 4.1 explains the results of the case where L_x is adjusted as slightly larger or smaller, maintaining the other four parameters L_y , $slitw$, $slith$ and $slitd$. As L_x increases or decreases gradually to become larger or smaller than 3.5 mm, the gap size of EFC increases, failing to form a conical point at EFC. Also, we examine the results of fine-tuning the other four parameters as shown in from Table 4.2 to Table 4.5. This information can introduce which factor among the four parameters of the metamaterial unit cell would be more sensitive. Our findings through the perturbation study confirm that the metamaterial unit cell proposed in this study is well prepared with EFC formation showing conical refraction performance. Because minimal changes in geometric values may affect the performance, it has significance that the metamaterial is elaborately fabricated and tested within minimal error. The parameter study conducted in Section 4.2 is expected to

subsequently help discover the optimal unit cell structure according to the operational frequency band.

4.3 S-parameter retrieval method for the effective property

To verify the effectiveness of the engineered metamaterial, we need to check whether the effective properties of the metamaterial truly meet the target conditions such that $C_{11} = C_{66}$ and $C_{16} = C_{26} = 0$. The study in Section 4.3 introduces how we obtain the effective stiffness tensor of the anisotropic metamaterial unit cell by using the S-parameter retrieval method. Because elastic waves, other than acoustic waves or electromagnetic waves, are with a mixture of a longitudinal wave and a transverse wave, it shows complexity. Thus, a more complicated procedure is required to find the effective property of an elastic metamaterial [49].

At first, the reflection and transmission coefficients should be calculated by using the simulation model shown in Fig. 4.7. Those coefficients are exploited to find the effective property of our proposed metamaterial. The cyan colored EFC in Fig. 4.7 is obtained from an effective medium with the calculated effective property. This perfectly corresponds to the EFC from the actual metamaterial unit cell by using eigen-frequency analysis.

In addition, the proof of the effective property can be conducted by comparing and analyzing the scattering parameters obtained from the simulation model in Fig. 4.7. SLL and SLT imply the transmission coefficients for the transmitted longitudinal and transverse waves, respectively. RTL and RTT imply the reflection coefficients

of the reflected longitudinal and transverse waves. Fig. 4.8 explains a comparison of the reflection and transmission information calculated from a medium with an effective property of a metamaterial unit cell at 100 kHz, to the wave scattering results of an actual metamaterial unit cell. The cyan dot plot and blue colored line are confirmed to be well matched. This result means that the scattering property of the engineered anisotropic metamaterial unit cell corresponds to that of a medium with effective parameters. Now we can say that the adequacy of the effective parameters for the elastic medium is verified by using the S-parameter retrieval method.

Fig. 4.9 shows plots regarding the effective density and effective stiffness tensor of the metamaterial unit cell, found by using the S-parameter retrieval method. The conditions for conical refraction, such that $C_{11} = C_{66}$, are well satisfied in the broad frequency band from 50 kHz to 120 kHz, as confirmed in the middle panel. The process for finding the effective property is referenced to the research; material property characterization studies on elastic medium [49].

4.4 Phase information of transmitted elastic waves

In Section 3.5, we have verified, by numerical simulation and experiments, a methodology to send waves along only one of two paths where elastic waves propagate inside the metamaterial. This goal is attained by generating destructive interference along the selected path among two paths. Thus, phase information on the L-wave and T-wave is important as we have previously mentioned.

Whether the excited elastic wave is the L-wave or T-wave before entering the metamaterial, both wave types can propagate after exiting the metamaterial. At this point, we need to focus on the fact that the upward and the downward waves inside the metamaterial have an opposite phase each other only for the wave type different with the excited one. Figs. 4.10(a) and 10(b) show the phase information, by the simulation shown in Fig. 3.3, extracted along a vertical line at 200 mm behind from the metamaterial. The blue and red boxes represent the phase information on translocated waves in the lower and upper paths, respectively. As shown in Fig. 4.10(a), when L-waves are excited and measured, the translocated waves in the upper and lower paths are in phase. On the other hand, when T-waves are excited and L-waves are measured, the translocated waves in the upper and lower paths are out of phase. Likewise, as shown in Fig. 4.10(b), when the L-wave is excited and the T-wave is measured, the translocated waves in the upper and lower paths are out of phase. On the other hand, when T-waves are excited and measured, the translocated waves in the upper and lower paths are in phase.

These phase behavior can be verified experimentally. As shown in Fig. 4.10(c), when an excited wave and a measured wave are all L-waves, the blue colored #5 signal, implying waves translocated in the lower path, and the cyan colored #13 signal, implying waves translocated in the upper path, are measured in phase. On the other hand, when an excited wave is the T-wave and a measured wave is the L-wave, two translocated waves are out of phase each other, showing a subtle difference. Likewise, as shown in Fig. 4.10(d), when an excited wave and a measured wave are all T-waves, the waves translocated in the lower path (the red colored line) or the upper path (the magenta colored dashed line) are in phase. On the other hand, when the types of an excited wave and a measured wave are different, two translocated waves are out of phase each other. Accordingly, the key phase information is identified by numerical simulation and experimentally to implement the phenomenon whereby waves are transmitted along one of the two paths inside the metamaterial. If we set a path occurring a destructive interference by tuning the phase of transmitters, the wave propagation direction can be chosen freely.

4.5 Time transient analysis

4.5.1 Snapshot of wave propagation in the engineered metamaterial

The results from the harmonic analysis for the engineered metamaterial are described in Chapter 3. In the simulation results, the incident elastic waves are conically deflected inside the metamaterial slab, and they propagate in the normal direction to the boundary of the metamaterial slab after exiting the metamaterial.

Here, the transient analysis is introduced where the generation and progress of the excited waves are examined according to each time step by using the finite element software COMSOL Multiphysics. The simulation model for time transient analysis is shown in the left panel of Fig. 4.11. The width of the metamaterial slab is 280 mm, and longitudinal waves (L-waves) are excited at $L_L = 4\lambda_L = 238$ mm from the entrance of the metamaterial. These geometric dimensions are identical with the ones in the harmonic analysis, as conducted in Fig. 3.3. Where the L-wave Gabor pulse at the 90 kHz center frequency is excited, the von Mises stress field distribution at $t = 30.0 \mu s$ is shown in the right panel of Fig. 4.11(a). The white dashed box represents the effective medium of the metamaterial. The effective property at 90 kHz is used for the effective medium obtained from the S-parameter retrieval method. Fig. 4.11(a) explains that the excited L-waves are incident on the metamaterial at about $t = 30.0 \mu s$.

The following description covers the progress of wave propagation inside and outside the metamaterial slab according to each time step. The interpretations are divided into propagation processes of the L-waves and transverse waves (T-waves), respectively. $(P_n)_{L-wave}$ implies a power density of L-wave propagating in the x -direction; where $(P_n)_{L-wave} = |-0.5V_x\sigma_{xx}|$ is expressed with V_x , particle velocity along x direction and σ_{xx} , normal stress. $(P_n)_{T-wave}$ implies a power density of T-wave propagating in the x direction; where $(P_n)_{T-wave} = |-0.5V_y\sigma_{xy}|$ is expressed with V_y , particle velocity along y direction and σ_{xy} , shear stress. As shown in Fig. 4.11(b), the propagation process of the L-waves normally incident on the metamaterial is identified at time steps of $t = 64.5\mu s$, $t = 124.5\mu s$, $t = 174.5\mu s$ and $t = 214.5\mu s$. Excited L-waves begin to multi-directionally deflect by conical refraction as they enter the metamaterial slab, and the waves are confirmed to exit in the direction normal to the metamaterial slab after passing through the slab.

The propagation process of the T-wave can be identically explained, as shown in Fig. 4.11(c). Note that the L-wave and T-wave inside the metamaterial have the same wave propagation speed due to the conical double point. Accordingly, the power densities in each plot of Figs. 4.11(b) and 11(c) are measured at the same location from the wave field distribution at the time step $t = 124.5\mu s$. Of course,

after exiting the metamaterial slab, L-waves propagate faster than T-waves because the waves propagate along the isotropic aluminum plate.

Time transient analysis on normally incident T-waves can be described as in Fig. 4.12. As shown in the simulation model, T-waves are excited at $L_T = 4\lambda_T = 138 \text{ mm}$ from the entrance of the metamaterial slab. In this case, the T-wave Gabor pulse is excited at the 90 kHz center frequency. Excited T-waves begin to be incident on the metamaterial slab approximately at $t = 30.0 \mu\text{s}$. The field distributions of the power densities $(P_n)_{L\text{-wave}}$ and $(P_n)_{T\text{-wave}}$ according to each time step show a similar tendency with the case for excitation of L-waves. Through the study in this research, the performance of our proposed metamaterial could be effectively verified by not only harmonic wave propagation analysis but also time transient analysis.

4.5.2 Power transmission calculation

By exploiting the results from the time transient analysis, the power transmission can be calculated. Power transmission means how much the amount of input power passes through the metamaterial slab. The *boundary 1* and *boundary 2*, shown in Fig. 4.11 and Fig. 4.12, signify the boundary to calculate the input power and

transmitted power, respectively. The time and boundary integrals are performed with power density $(P_n)_{L-wave}$ and $(P_n)_{T-wave}$ at *boundary 1* and *boundary 2*.

Let us start with an incidence of the 90 kHz L-wave source, shown in Fig. 4.11. Input power is obtained by integrating $(P_n)_{L-wave}$ during Δt , the time interval between the creation and extinction of L-waves at the *boundary 1*. Thus, the input power can be expressed as

$$(P_{input})_{L-wave} = \iint (P_n)_{L-wave} dA dt . \quad (4.1)$$

Of course, the waves reflected from left-end boundary are not considered and thus ignored in calculation of equation (4.1). Likewise, the transmitted power passing through the metamaterial slab can be calculated for the L-wave and the T-wave respectively, using the relationships as followings:

$$(P_{transmitted})_{L-wave} = \iint (P_n)_{L-wave} dA dt \quad (4.2)$$

$$(P_{transmitted})_{T-wave} = \iint (P_n)_{T-wave} dA dt . \quad (4.3)$$

By using the equations from (4.1) to (4.3), the power transmission is obtained as follows:

$$(P_{transmitted})_{L-wave} / (P_{input})_{L-wave} = 0.2735 \quad (4.4)$$

$$(P_{transmitted})_{T-wave} / (P_{input})_{L-wave} = 0.3440. \quad (4.5)$$

On the other hand, for the incident T-wave source at 90 kHz, shown in Fig. 4.12, power transmission can be calculated using the same process. As a result, we can obtain the following results:

$$(P_{transmitted})_{L-wave} / (P_{input})_{T-wave} = 0.3249 \quad (4.6)$$

$$(P_{transmitted})_{T-wave} / (P_{input})_{T-wave} = 0.4301. \quad (4.7)$$

There is a difference between the impedance of the aluminum medium and the metamaterial system due to a difference in their material properties. Thus, it affects power transmission. If certain metamaterials were engineered while maintaining the conical double point characteristic and with the same impedance as aluminum, a transmission-enhanced system would be proposed in future work.

4.6 Detouring around the high-risk area

Chapter 3 introduces a methodology whereby elastic waves normally incident on the metamaterial slab are returned to the plate center by twice deflecting the waves. A safety zone, free from stress waves, can be formed between the two metamaterial slabs. If a high-risk facility is located in the safety zone, the facility would not be affected by a mechanical stress wave. This is highly expected to be successful application for many fields of industry.

Section 4.6 introduces the simulation results with respect to various object sizes located in the high-risk zone. The simulation shows that the performance of the metamaterial depends on the presence of the metamaterial slab in front of and behind the high-risk zone. Fig. 4.13 shows a conceptual diagram of the high-risk area. Mechanical stress waves propagate in the detours above and the below the high-risk area, and this ability is invariable regardless of whether the incident wave is an S_0 wave or SH_0 wave.

The following description covers the case where, as shown in Fig. 4.14, two metamaterial slabs are installed without any object at the center of a plate. They are spaced 0.2862 m apart. When the S_0 wave is excited, the waves are multi-directionally deflected at the first metamaterial slab due to conical refraction. After exiting the first metamaterial slab, both the S_0 wave and SH_0 wave propagate at the aluminum plate area. Then, a safety zone is formed at the center, free from impact

by elastic waves. When S_0 waves and SH_0 waves encounter the second metamaterial slab, the waves are deflected downward at the upper path and upward at the lower path. After exiting the second metamaterial slab, SH_0 waves do not propagate due to wave cancellation; only S_0 waves propagate in the x direction. For the case when the SH_0 wave is excited initially, the same explanation can be used in the analysis. However, in this case, after exiting the second metamaterial slab, S_0 waves do not propagate due to wave cancellation after exiting the second metamaterial slab; only SH_0 waves propagate in the x direction. These results can be explained with Fig. 4.15.

Now we analyze the case in which vulnerable objects are located at the center of the plate. Note that a safety zone free from mechanical stress waves can be formed by using two metamaterial slabs. If there is an 0.1×0.05 m object as shown in Fig. 4.16, waves confronting the object directly affect the object. The results can be easily understood from the simulation where the 90 kHz SH_0 wave is incident with a source width of 0.2 m. However, if the designed metamaterial slabs are installed in front of and behind the object as shown in Fig. 4.17, we could make two detours around the object. Mechanical stress waves do not affect an object, and they return to the center of the plate. Our proposing system is applicable to facilities vulnerable to stress waves and applicable as a new way of cloaking.

The distance between two metamaterial slabs needs to be carefully determined to implement this phenomenon, restricting the wave propagation path inside the second metamaterial slab. Consider the case where a larger area needs protection against mechanical waves due to a wider object. This case can be verified as in Fig. 4.18. The results of the simulation confirm that the safety zone at the center of the plate is extended. The performance is still superior where mechanical waves propagate in the detours above and below the safety zone. The distance between the two metamaterial slabs is 0.5315 m. This value is determined for the case in which both longitudinal and transverse waves propagate along only the targeted path inside the second metamaterial slab.

The following description considers the simulation results where a vertically longer object is located in the high-risk area. Fig. 4.19 shows the case where an excited wave is confronting the 0.1×0.2 m object. Due to the similarity in wave source length and object size, the object is directly exposed to impact by the stress waves. Accordingly, reflections are dominant without scattering of waves. On the other hand, where two metamaterial slabs are installed as shown in Fig. 4.20, the object is safe from mechanical stress waves.

At this point, the question arises as to how the vertical length of a safety zone at the center of the plate, which can be formed by a metamaterial, can be controlled. Conical refraction can control the deflection angle of waves by a metamaterial,

requiring a new metamaterial structure with a deflection angle greater than or less than that of the current metamaterial. Topology optimization can be utilized to design a target EFC shape. In Chapter 5, the results of topology optimization will be introduced to propose metamaterial structures with various deflection angles.

4.7 Summary

An in-depth analysis on an engineered metamaterial is explained. Our proposed metamaterial composed of non-resonant type unit cells has a broadband operational frequency range. The experimental verification of the broadband metamaterial is described in this chapter. Furthermore, a perturbation study is conducted on the dimension of the slits comprising the metamaterial unit cells and its impact on EFC is analyzed. Testing of the effective property of the metamaterial is conducted by the S-parameter retrieval method to explain that the structure of our proposed metamaterial is such that it effectively shows the target performance. Chapter 3 described the harmonic analysis to show that elastic waves are conically deflected; on the other hand this chapter introduces the progress of wave propagation by conducting transient analysis according to several time steps. Also, the power transmissions for the elastic waves are calculated and reported. This study introduces a method for protecting a high-risk facility against mechanical stress waves by using two metamaterial slabs. The simulations for the various geometric dimensions a facility may have are conducted and the results are presented. This analysis is carried out to determine the impact of waves on the object, depending on the presence of elaborately designed metamaterial slabs. Our proposing protection system of mechanical stress waves are based on an important phase relation among elastic waves propagating along upper and lower paths. In this chapter, we identify the phase information after passing through the metamaterial slab by numerical simulation and experiments.

Table 4.1 Parameter study for geometry size of the anisotropic elastic metamaterial unit cell. Especially for the lattice period along x direction.

Numbering (#)	L_x (mm)	L_y (mm)	slitw (mm)	slith (mm)	slitd (mm)	gap
#1	3.3	5.0	0.7	2.7	2.0	20.3266
#2	3.4	5.0	0.7	2.7	2.0	9.5420
#3	3.6	5.0	0.7	2.7	2.0	7.4135
#4	3.7	5.0	0.7	2.7	2.0	14.2932

Table 4.2 Parameter study for geometry size of the anisotropic elastic metamaterial unit cell. Especially for the lattice period along y direction.

Numbering (#)	L_x (mm)	L_y (mm)	slitw (mm)	slith (mm)	slitd (mm)	gap
#5	3.5	4.8	0.7	2.7	2.0	2.6465
#6	3.5	4.9	0.7	2.7	2.0	1.8408
#7	3.5	5.1	0.7	2.7	2.0	1.4515
#8	3.5	5.2	0.7	2.7	2.0	3.7948

Table 4.3 Parameter study for geometry size of the anisotropic elastic metamaterial unit cell. Especially for the slit width.

Numbering (#)	L_x (mm)	L_y (mm)	slitw (mm)	slith (mm)	slitd (mm)	gap
#9	3.5	5.0	0.5	2.7	2.0	5.4602
#10	3.5	5.0	0.6	2.7	2.0	2.8531
#11	3.5	5.0	0.8	2.7	2.0	4.5255
#12	3.5	5.0	0.9	2.7	2.0	9.5481

Table 4.4 Parameter study for geometry size of the anisotropic elastic metamaterial unit cell. Especially for the slit height.

Numbering (#)	L_x (mm)	L_y (mm)	slitw (mm)	slith (mm)	slitd (mm)	gap
#13	3.5	5.0	0.7	2.5	2.0	19.6160
#14	3.5	5.0	0.7	2.6	2.0	9.6879
#15	3.5	5.0	0.7	2.8	2.0	10.6006
#16	3.5	5.0	0.7	2.9	2.0	20.5711

Table 4.5 Parameter study for geometry size of the anisotropic elastic metamaterial unit cell. Especially for the distance between adjacent slits in the x direction.

Numbering (#)	L_x (mm)	L_y (mm)	slitw (mm)	slith (mm)	slitd (mm)	gap
#17	3.5	5.0	0.7	2.7	1.8	4.0031
#18	3.5	5.0	0.7	2.7	1.9	2.5468
#19	3.5	5.0	0.7	2.7	2.1	5.1868
#20	3.5	5.0	0.7	2.7	2.2	12.1079

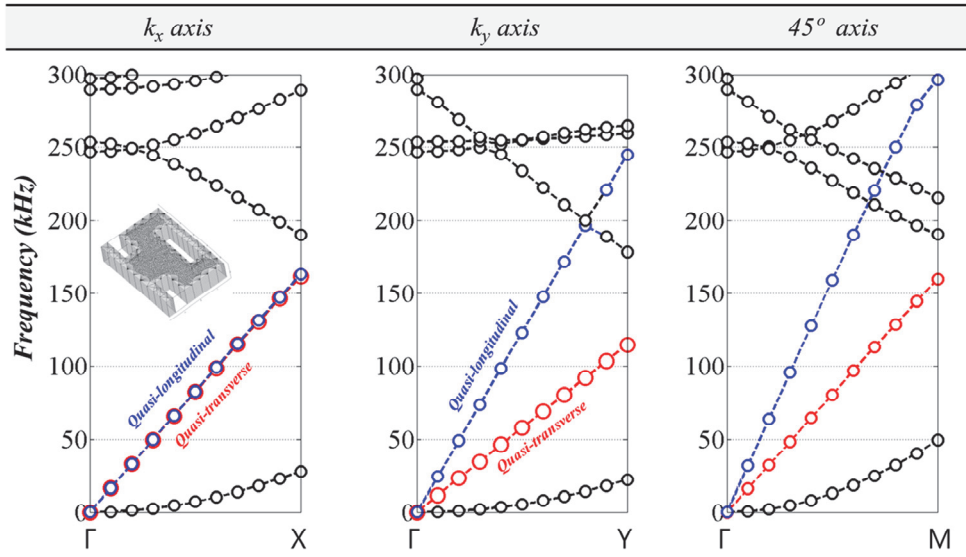


Figure 4.1 Dispersion curve of proposed anisotropic metamaterial along k_x (ΓX), k_y (ΓY) and 45° (ΓM) axis.

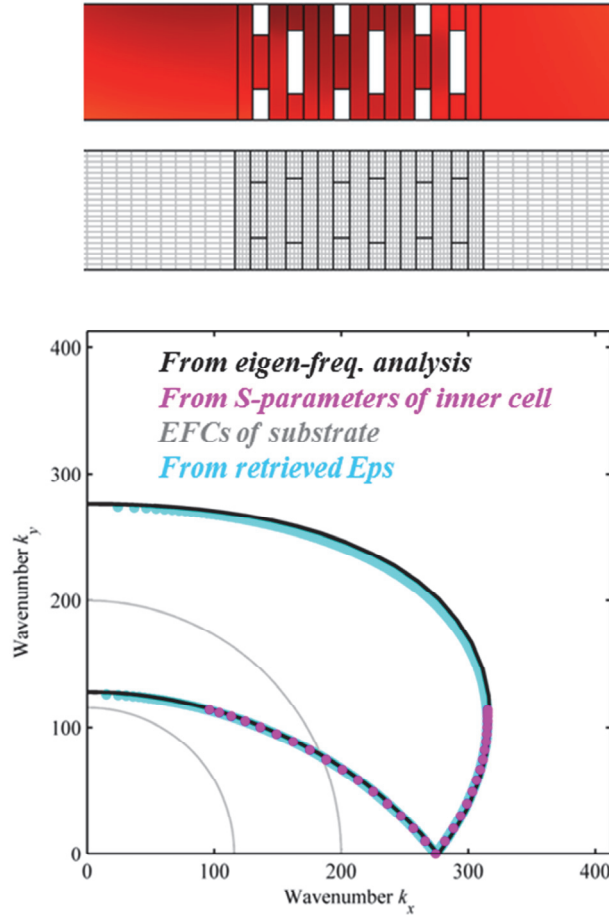


Figure 4.2 Simulation model for calculating transmission and reflection coefficients (upper panel). EFC estimations by using measured scattering parameters or retrieved effective properties at 100 kHz (lower panel).

From detailed model (Inner cell), From retrieved EPs

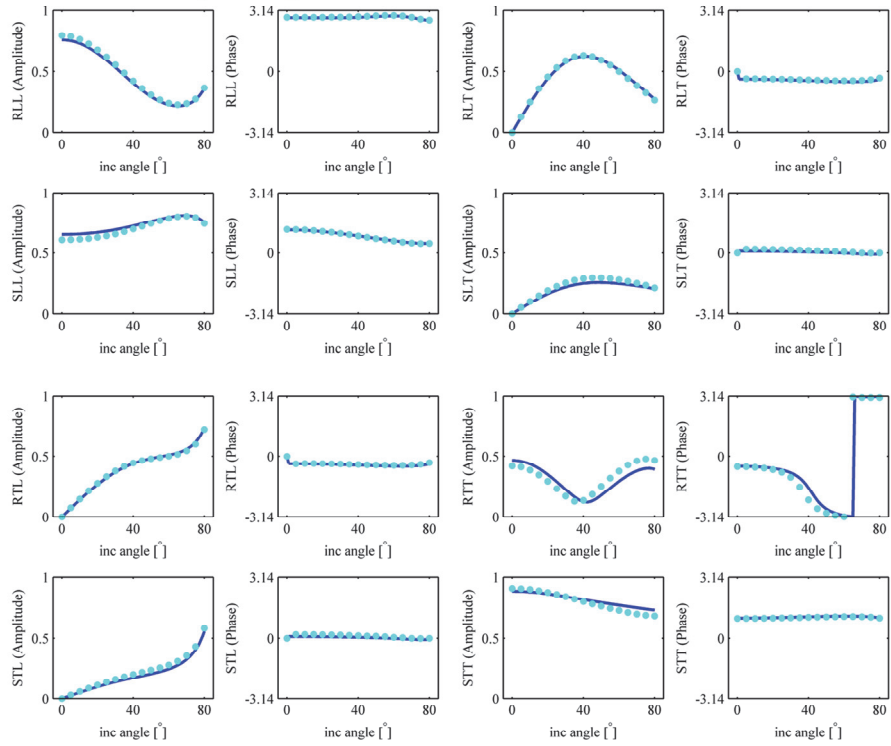


Figure 4.3 Validation of retrieved effective parameters by the comparison of scattering parameters at 100 kHz.

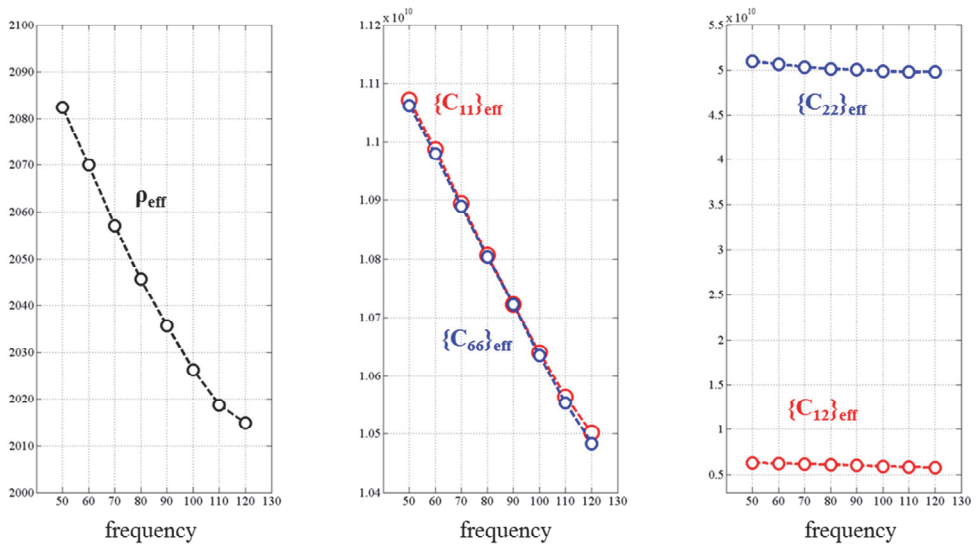


Figure 4.4 Graph for effective density and effective stiffness tensor obtained by S-parameter retrieval method in the frequency range from 50 kHz to 120 kHz.

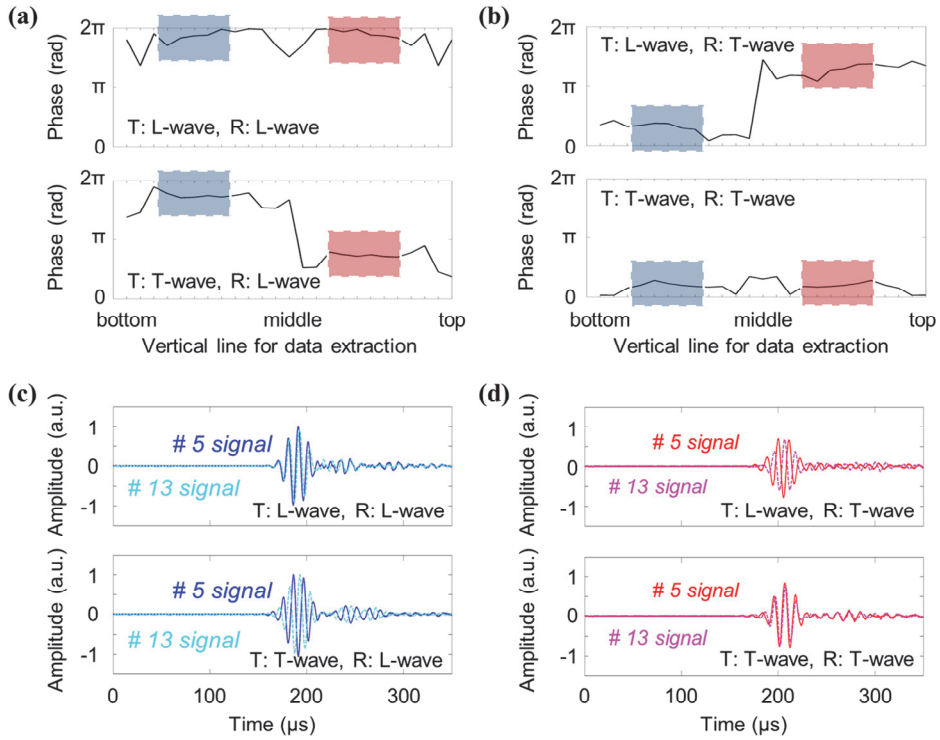


Figure 4.5 Phase information by numerical simulation and experimental signals. (a,b) Numerical phase information along the vertical line at the 200 mm behind of the metamaterial. (c,d) Experimentally measured signal at point #5 (blue and red solid) and point #13 (cyan and magenta dashed).

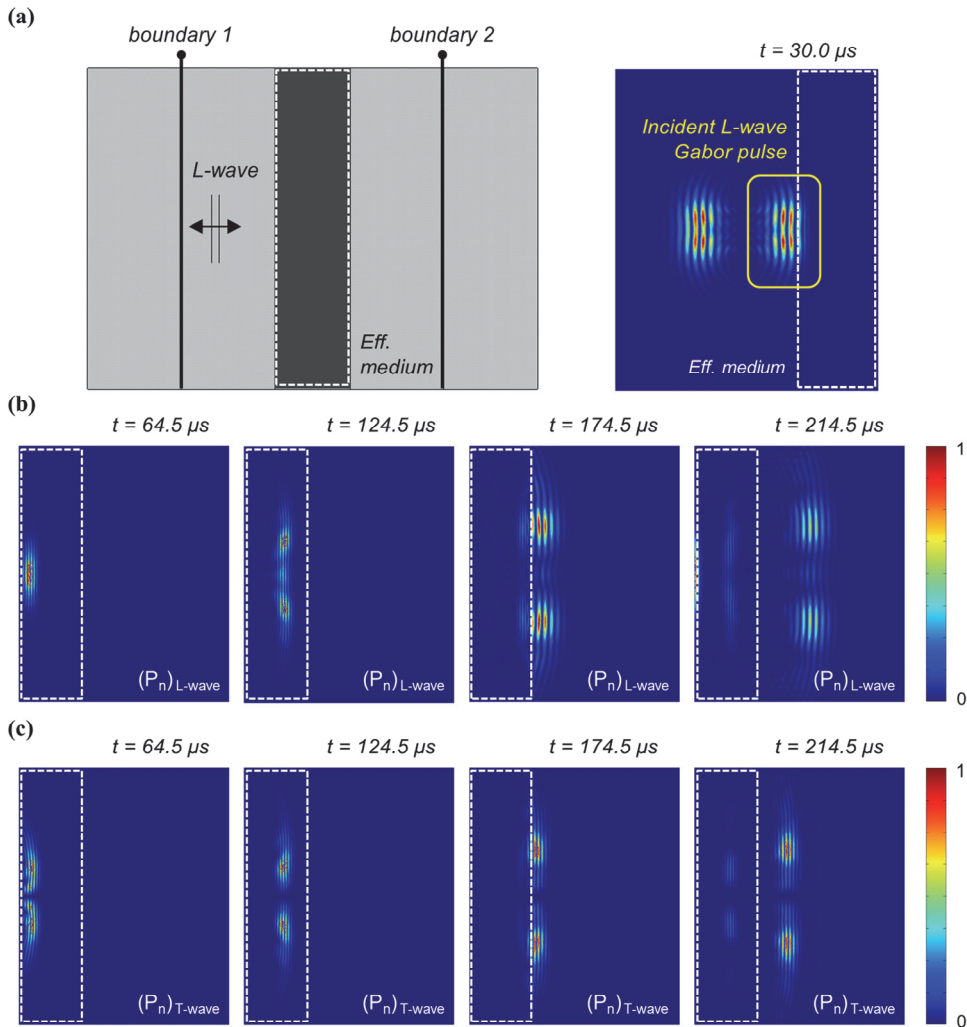


Figure 4.6 Time transient analysis for effective medium of proposed anisotropic elastic metamaterial. (a) Gabor pulse of longitudinal waves propagates along both negative and positive x directions and incident on metamaterial. (b,c) Normalized power density for (b) longitudinal wave and (c) transverse wave component at the time 64.5, 124.5, 174.5 and 214.5 μs .

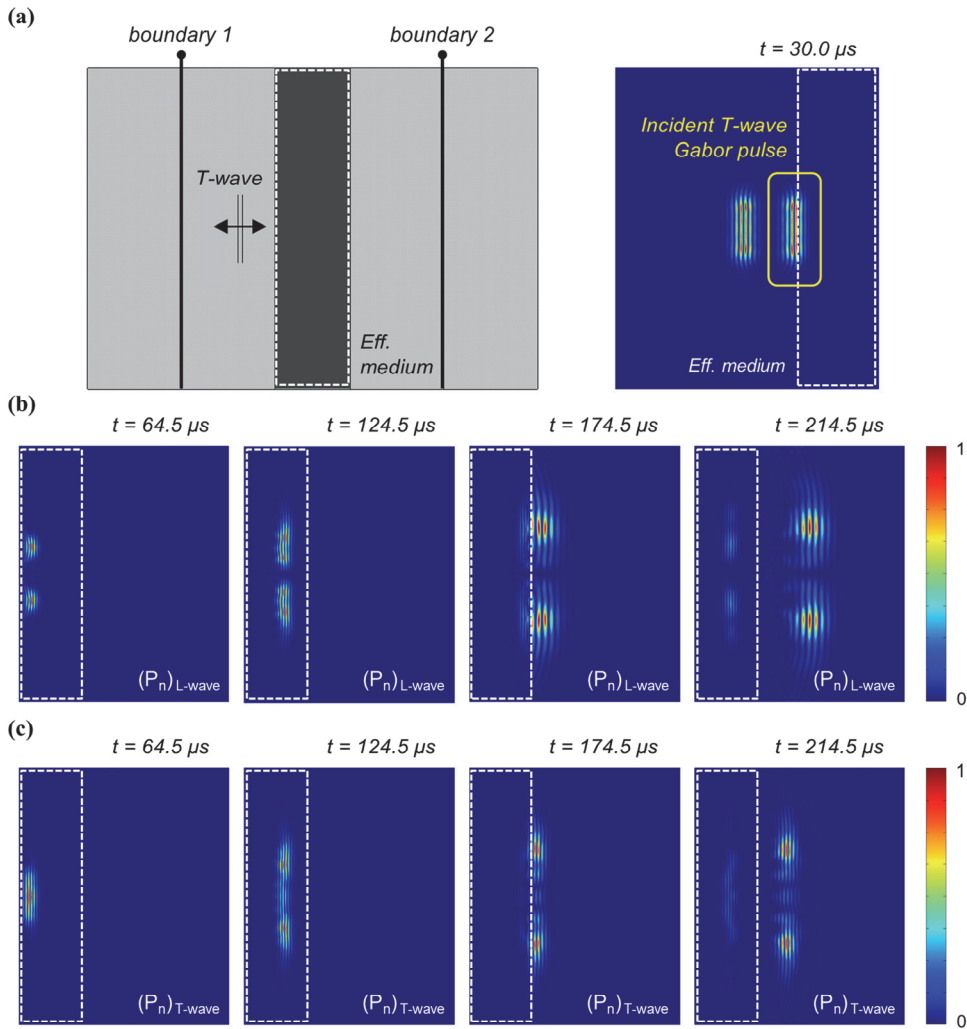


Figure 4.7 Time transient analysis for effective medium of proposed anisotropic elastic metamaterial. (a) Gabor pulse of transverse waves propagates along both negative and positive x directions and incident on metamaterial. (b,c) Normalized power density for (b) longitudinal wave and (c) transverse wave component at the time 64.5, 124.5, 174.5 and 214.5 μs .

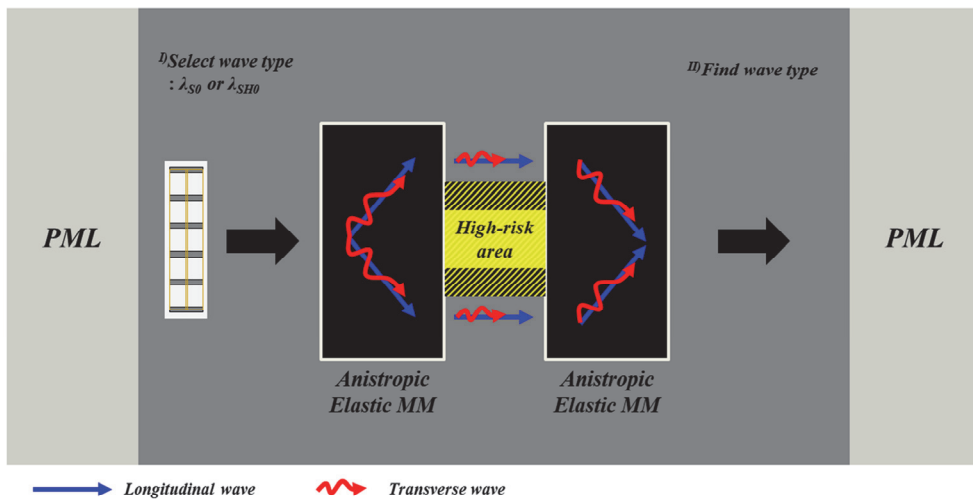
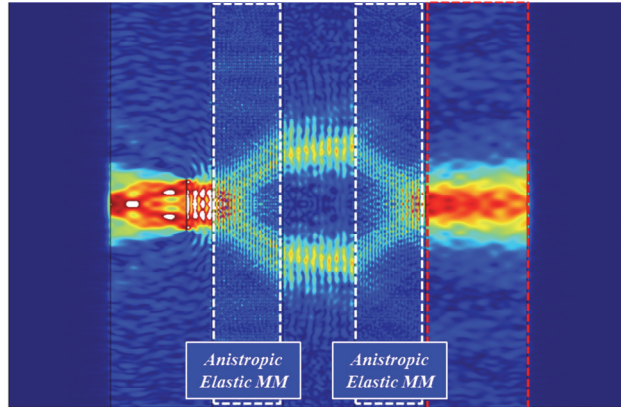


Figure 4.8 Schematic diagram of detouring around the high-risk area by using anisotropic elastic metamaterials.

- *normal stress amplitude*



- *shear stress amplitude*

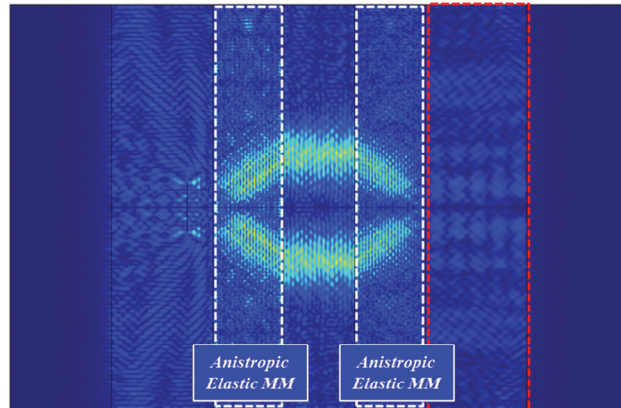
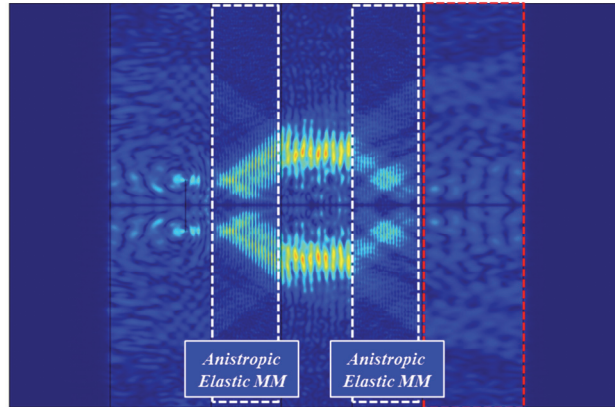


Figure 4.9 Numerical simulation results of S_0 wave excitation to verify the detouring of high-risk area.

- *normal stress amplitude*



- *shear stress amplitude*

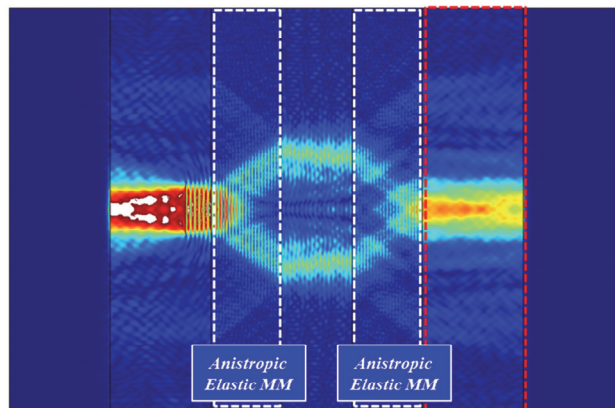


Figure 4.10 Numerical simulation results of SH_0 wave excitation to verify the detouring of high-risk area.

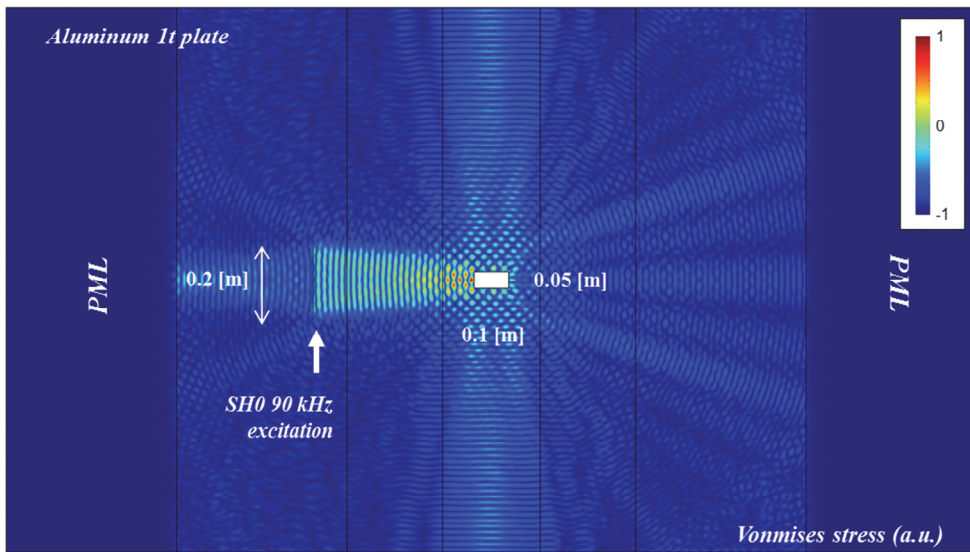


Figure 4.11 Numerical simulation results when 90 kHz SH₀ wave incidents directly on the object whose size is 0.1 m and 0.05 m for width and height respectively.

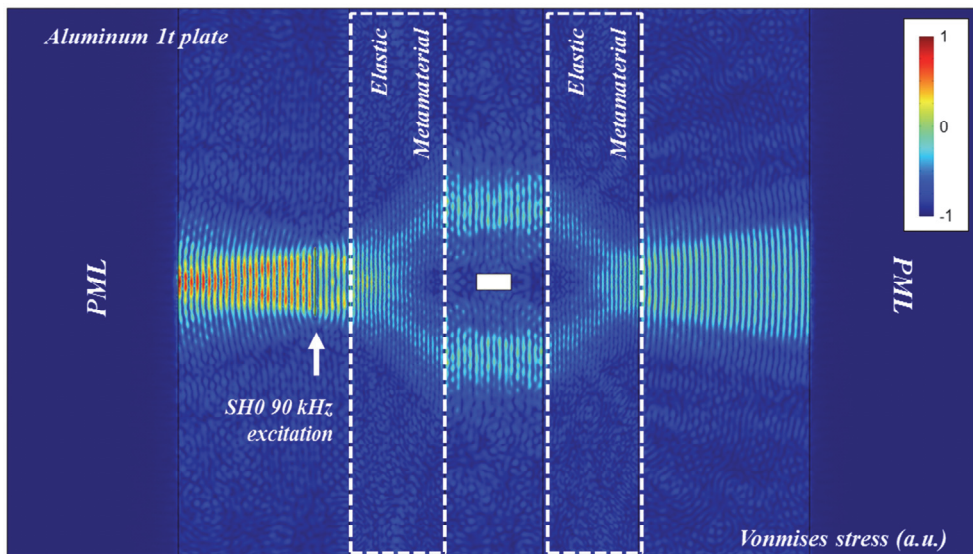


Figure 4.12 Numerical simulation results when 90 kHz SH₀ wave incidents on the engineered elastic metamaterial. It makes a detour around object whose size is 0.1 m and 0.05 m for width and height respectively.

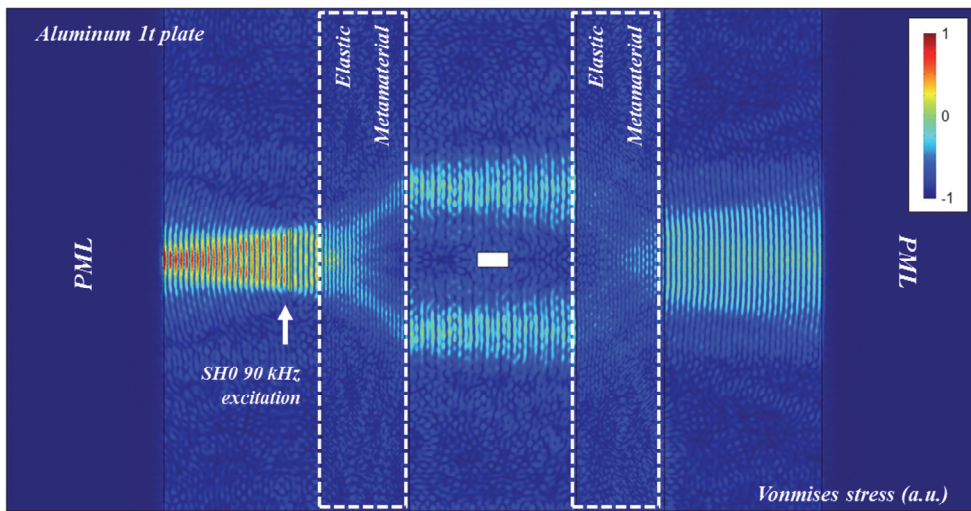


Figure 4.13 Numerical simulation results when 90 kHz SH₀ wave incidents on the engineered elastic metamaterial. The horizontal length of the safety zone is set to be larger value.

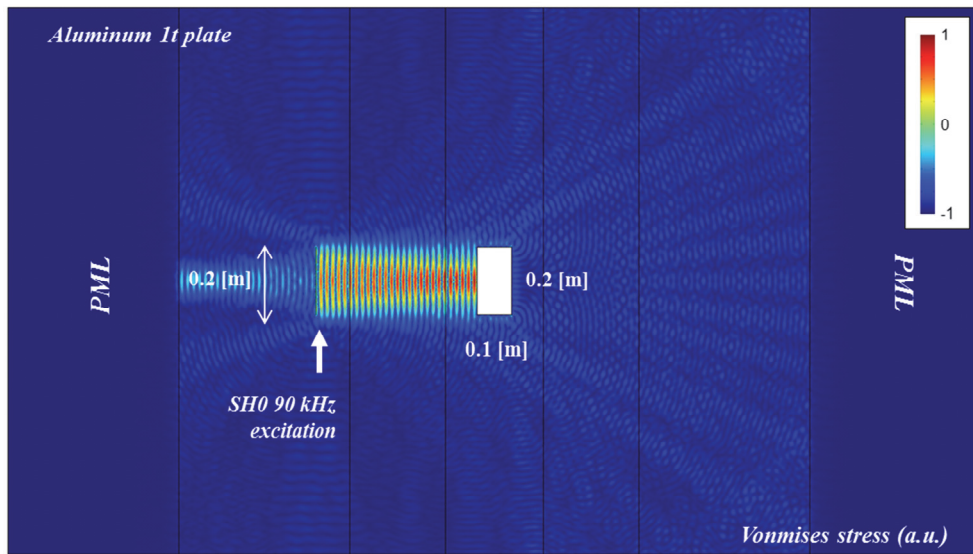


Figure 4.14 Numerical simulation results when 90 kHz SH_0 wave incidents directly on the object whose size is 0.1 m and 0.2 m for width and height respectively.

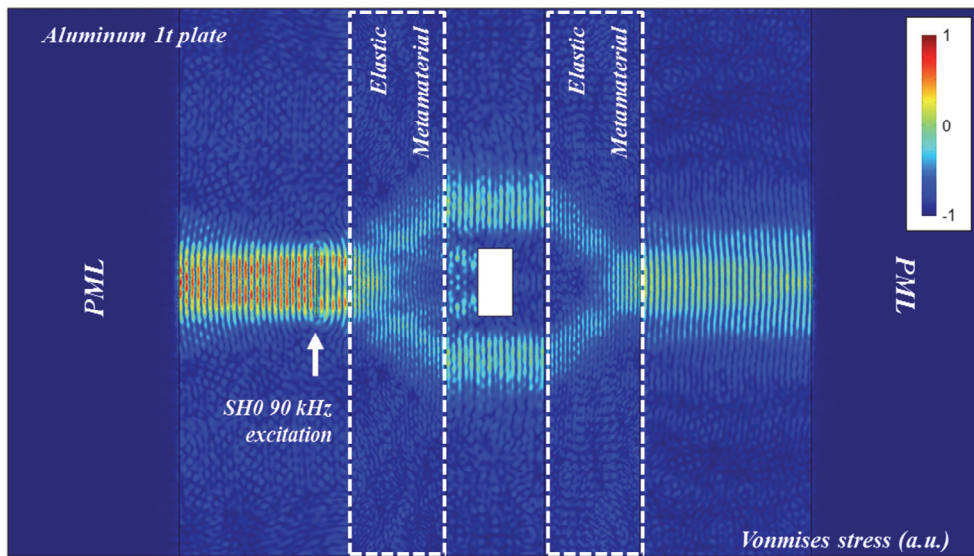


Figure 4.15 Numerical simulation results when 90 kHz SH_0 wave incidents on the engineered elastic metamaterial. It makes a detour around object whose size is 0.1 m and 0.2 m for width and height respectively.

CHAPTER 5

TOPOLOGY OPTIMIZATION OF METAMATERIAL UNIT CELLS FOR ADJUSTING THE DEFLECTION ANGLE

5.1 Overview

This chapter is to find candidates for metamaterial unit cells showing various deflection angles. As reported in Chapter 3, the normally incident elastic waves can be deflected into both upward and downward directions with the deflection angle θ_d . The manipulation of this angle can be carried out with controlling the Equi-Frequency Contour (EFC) at the wavevector k_x direction. To do this, we design the unit cell of anisotropic elastic metamaterial by employing the topology optimization method. Topology optimization is a methodology to find optimal structure achieving the objective function. The objective function and constraints

are mathematically defined to evaluate the performance of designed structure. The design domain is discretized with many elements. By iterative procedure, if the designed structure satisfies the convergence condition, then the configuration at the final iteration would be an optimal result.

The topology optimization originally has been developed for designing the structures such as the bridge, building, beam and truss structure. However, it has been also used to design crystal structures [61-70]. Among them, many researches have mainly concerned with the bandgap maximization [71-80], a representative problem. Recently in Ref. [81], the methodology for following the target EFC of anisotropic metamaterials has been also reported to prevent distortion of elastic waves in waveguide.

Here, we present two design results for adjusting the deflection angle by using the topology optimization. First, we set up the design #1 of which deflection angle has bigger than the previous value of θ_d in Chapter 3. Second, the design #2 of which deflection angle has smaller than θ_d in Chapter 3 is defined. We explain the formulation for the optimization and report the configuration of unit cells satisfying the target EFC for those two deflection angles.

5.2 Topology optimization of periodic structures in frequency domain

The topology optimization of periodic structures in frequency domain is introduced, especially for the bandgap maximizing topology optimization that has drawn a lot of attention. The bandgap structure can prevent wave propagation in certain frequency range. Designing the bandgap structure could be a fundamental of many other design researches on periodic structures including metamaterials. Furthermore, some of the formulation and technical explanation in Section 5.2 are still valid in design process of metamaterial unit cells.

For topology optimization, the element matrices \mathbf{K}_e and \mathbf{M}_e are interpolated by the design variable x_e ($0 \leq x_e \leq 1$) assigned to the e^{th} element. For a unit cell consisting of host and inclusion materials, \mathbf{K}_e and \mathbf{M}_e can be interpolated as

$$\mathbf{K}_e = \iint_{\Omega_e} (\mathbf{B}_1 + i\mathbf{B}_2)^T \mathbf{C} (\mathbf{B}_1 + i\mathbf{B}_2) d\Omega_e = (1 - x_e^{\alpha_K}) \mathbf{K}_{host} + x_e^{\alpha_K} \mathbf{K}_{inclusion}, \quad (5.1)$$

$$\mathbf{M}_e = \iint_{\Omega_e} \rho \mathbf{H}^T \mathbf{H} d\Omega_e = (1 - x_e^{\alpha_M}) \mathbf{M}_{host} + x_e^{\alpha_M} \mathbf{M}_{inclusion} \quad (5.2)$$

where Ω_e and $d\Omega_e$ denote the area of the finite element and the infinitesimal area, respectively. The matrices $(\mathbf{K}_{host}, \mathbf{M}_{host})$ denote the element stiffness and

mass matrices for the host medium while $(\mathbf{K}_{inclusion}, \mathbf{M}_{inclusion})$ denote those for the inclusion medium of a given Phononic Crystal (PC). The penalization parameters α_K and α_M are selected to be 3 and 1, respectively. (The influence of these parameters on optimized results may be found in Bendsøe and Sigmund [82].)

Let us present the topology optimization formulation for finding PC unit cells that maximize a target bandgap. Specifically, we aim to maximize the lowest frequency of the $(i+1)^{th}$ branch and minimize the highest frequency of the i^{th} branch. Thus, the bandgap between two adjacent branches is maximized for a selected branch number i . The following is a topology optimization setup formulated for bandgap maximization using the bound parameters [83]:

$$\text{Objective: } \underset{\beta_1, \beta_2, x_1, \dots, x_N}{\text{Minimize}} \quad f_{obj} = \frac{\beta_2 - \beta_1}{\frac{\beta_1 + \beta_2}{2}} \quad (5.3)$$

$$\text{Constraint 1: } [\omega_{i+1}(\mathbf{k})]_p \geq \beta_1, \quad p = 1, 2, \dots, N_k \quad (5.4)$$

$$\text{Constraint 2: } [\omega_i(\mathbf{k})]_p \leq \beta_2, \quad p = 1, 2, \dots, N_k \quad (5.5)$$

where f_{obj} is an objective function for topology optimization, β_1 and β_2 are the bound parameters that control the upper and lower branches respectively, and

N_k is the number of wavevector points lying along $\mathbf{k} \in [\Gamma - X - M - \Gamma]$ for a square lattice. The method of moving asymptotes [84] is used as an optimization algorithm, and the sensitivity of the objective function and constraints are calculated by the adjoint method based on the following two equations:

$$\{\tilde{\mathbf{U}}_f\}_i^T \mathbf{M}_f \{\tilde{\mathbf{U}}_f\}_i = 1 \quad (5.6)$$

$$\frac{\partial \omega_i}{\partial x_e} = \frac{1}{2\omega_i} \{\tilde{\mathbf{U}}_f\}_i^T \frac{\partial \mathbf{K}_f}{\partial x_e} \{\tilde{\mathbf{U}}_f\}_i - \frac{\omega_i^2}{2\omega_i} \{\tilde{\mathbf{U}}_f\}_i^T \frac{\partial \mathbf{M}_f}{\partial x_e} \{\tilde{\mathbf{U}}_f\}_i \quad (5.7)$$

where ω_i and $\{\tilde{\mathbf{U}}_f\}_i$ are the i^{th} eigenvalue and eigenvector, respectively. Equation (5.6) represents the mass-normalization condition, and equation (5.7) gives the sensitivity of eigenvalue ω_i . The sensitivity analysis is used to update the design domain to find the optimal topology of the unit cell. Note that these sensitivity equations are valid for a single eigenvalue problem. For the eigenvalue analysis, we consider $\mathbf{k} \in [\Gamma - X - M - \Gamma]$ for a square lattice.

We hereby are ready to obtain an optimized configuration of PC implementing a maximized bandgap size. Using the objective function and constraints in equations from (5.3) to (5.5), the topology optimization can be conducted while updating the design variables.

5.3 Topology optimization of periodic structures in wavenumber domain

5.3.1 Design proposal to control the deflection angle

The anisotropic metamaterial consisting of the unit cell shown in Fig. 5.1(a) can deflect the elastic waves with the angle of $\theta_d = 37.9^\circ$. It is easily identified by considering the normal direction of EFC at the intersecting point of two wave sheets. This elastic metamaterial has effective properties as follows: $\rho = 2035.7 \text{ kg/m}^3$, $C_{11} = 1.072 \times 10^{10} \text{ Pa}$, $C_{12} = 0.5994 \times 10^{10} \text{ Pa}$, $C_{22} = 5.004 \times 10^{10} \text{ Pa}$, $C_{66} = 1.072 \times 10^{10} \text{ Pa}$, $C_{16} = 0 \text{ Pa}$, and $C_{26} = 0 \text{ Pa}$. Note that EFC can be bulged in and out by controlling the anisotropy factor $A = 2C_{66} / (C_{11} - C_{12})$.

Let us consider the situation that the effective properties of the current metamaterial unit cell are fixed except for C_{12} . Thus, only the value of C_{12} can be changed into other values, and the conical refraction phenomenon is still valid. Fig. 5.1(b) shows the change of the EFC shape with respect to two different values of C_{12} . By decreasing the C_{12} value from $C_{12} = 0.5994 \times 10^{10} \text{ Pa}$ to $C_{12} = 0.1994 \times 10^{10} \text{ Pa}$, the deflection angle is changed into $\theta_d = 31.1^\circ$. On the other hand, by increasing the C_{12} value from $C_{12} = 0.5994 \times 10^{10} \text{ Pa}$ to

$C_{12} = 0.8994 \times 10^{10}$ Pa , the deflection angle is changed into $\theta_d = 43.7^\circ$.

These new deflection angles can be examined by simulation results. When the 90 kHz SH_0 wave incidents on the effective medium whose EFC is identical with Fig. 5.1(a), both longitudinal and transverse waves propagate along two generated paths with the deflection angle $\theta_d = 37.9^\circ$, as shown in Fig. 5.2. However, if the same incident wave encounters the effective medium whose EFC is identical with a left panel of Fig. 5.1(b), the system has more narrow deflection angle than the previous case, as shown in Fig. 5.3. Of course, the conical refraction performance is still effective as before because the components of effective stiffness tensor have a relation, $C_{11} = C_{66}$. On the other hand, as shown in Fig. 5.4, if the 90 kHz SH_0 wave incidents on the effective medium whose EFC is identical with a right panel of Fig. 5.1(b), it shows more widened deflection angle comparing with the results in Fig. 5.2.

Now, we can suggest two design proposals to follow the target EFCs as denoted in Fig. 5.1(b). By doing this, we employ the topology optimization. As an initial design domain, the previously engineered unit cell in Fig. 5.1(a) is selected, and its EFC acts as a starting line for topology optimization. As shown in Fig. 5.5, the design #1 is to make the deflection angle be $\theta_d = 43.7^\circ$, and the design #2 is to

make the deflection angle be $\theta_d = 31.1^\circ$. For the topology optimization, EFC is plotted with the interval of $\pi/6$.

Through the optimization, design #1 and #2 can achieve the directional tunability of elastic waves. A new configuration of metamaterial unit cells can be artificially designed while satisfying the condition for the conical refraction.

5.3.2 Formulations for topology optimization

In Section 5.3.2, the formulations for topology optimization of metamaterial unit cells are introduced. In Ref. [81], there has been a research that successfully conducts the curve fitting of EFC to the target shape by using the topology optimization. By referring the formulations in Ref. [81], we can start setting the topology optimization formulations for adjusting the deflection angles.

The basic equations in Section 5.3.1 are still valid such as element stiffness and mass matrices in equations (5.1) and (5.2). The initial unit cell considered in the optimization, i.e., our proposed metamaterial unit cell, is composed of an aluminum and air, as shown in Fig. 5.1(a). In this case, to construct the element stiffness and mass matrices, a density and the Young's modulus of each element can be interpolated during the iterations as follows:

$$\rho(\chi) = \rho_{Al}\chi^{p_{rho}} + \rho_{Air}(1 - \chi^{p_{rho}}) \quad (5.8)$$

$$E(\chi) = E_{Al}\chi^{p_E} + E_{Air}(1 - \chi^{p_E}) \quad (5.9)$$

where χ is the design variable and the penalization parameters are selected as $p_{rho} = 1$ and $p_E = 3$. For the material properties of air medium, $\rho_{Air} = 0.0001 \text{ kg/m}^3$ and $E_{Air} = 10^{-5} \text{ Pa}$ are used for preventing the convergence error. After constructing the element matrices, we can obtain the eigenvalue problem of equation (2.25). Then, equation (2.25) can be slightly changed into the following form:

$$k^2 \mathbf{U}_g^T \mathbf{A}_g \mathbf{U}_g + k \mathbf{U}_g^T \mathbf{B}_g \mathbf{U}_g + \mathbf{U}_g^T (\mathbf{C}_g - \omega^2 \mathbf{M}_g) \mathbf{U}_g = 0. \quad (5.10)$$

In the topology optimization, the sensitivity analysis is essential for updating the objective function and constraints. Using equation (5.10), the sensitivity of the wavenumber k with respect to the design variable χ_i can be expressed as

$$\frac{\partial k}{\partial \chi_i} = \frac{- \left\{ k^2 \mathbf{U}_g^T \frac{\partial \mathbf{A}_g}{\partial \chi_i} \mathbf{U}_g + k \mathbf{U}_g^T \frac{\partial \mathbf{B}_g}{\partial \chi_i} \mathbf{U}_g + \mathbf{U}_g^T \frac{\partial (\mathbf{C}_g - \omega^2 \mathbf{M}_g)}{\partial \chi_i} \mathbf{U}_g \right\}}{2k \mathbf{U}_g^T \mathbf{A}_g \mathbf{U}_g + \mathbf{U}_g^T \mathbf{B}_g \mathbf{U}_g} \quad (5.11)$$

through the following procedure:

$$\begin{aligned}
& 2k \frac{\partial k}{\partial \chi_i} \mathbf{U}_g^T \mathbf{A}_g \mathbf{U}_g + k^2 \mathbf{U}_g^T \frac{\partial \mathbf{A}_g}{\partial \chi_i} \mathbf{U}_g + \frac{\partial k}{\partial \chi_i} \mathbf{U}_g^T \mathbf{B}_g \mathbf{U}_g + \\
& k \mathbf{U}_g^T \frac{\partial \mathbf{B}_g}{\partial \chi_i} \mathbf{U}_g + \mathbf{U}_g^T \frac{\partial (\mathbf{C}_g - \omega^2 \mathbf{M}_g)}{\partial \chi_i} \mathbf{U}_g = 0.
\end{aligned} \tag{5.12}$$

Now, the followings are the objective function and the constraints to find optimized configuration of metamaterial unit cells demonstrating two target deflection angles. At first, if a design variable χ_i has a value between 0 and 1, a density and the Young's modulus of an i^{th} element have the intermediate property between the aluminum and air. To avoid this ambiguity, the objective function is defined as follows:

$$\text{Objective function: Minimize}_{\chi_m} \sum_{m=1}^{N_e} \chi_m (1 - \chi_m) / F_{Obj} \tag{5.13}$$

where N_e is the number of elements. This objective function makes elements should be either aluminum or air after finishing the topology optimization. The constant F is appropriate value which is selected at an initial iteration step for the best convergence of optimization.

On the other hand, the constraints play a role to follow the target EFC shape during

the iterations. As already examined in Fig. 3.2, the initial unit cell operates well in the frequency range of interest, i.e., from 60 kHz to 120 kHz. Thus, we aim to design the optimal structures operating in the same frequency range of interest. Thus, the Constraint 1 and Constraint 2 are proposed to control the EFC at the upper bound of interest frequency range. The Constraint 3 and Constraint 4 are proposed to control the EFC at the lower bound of interest frequency range. These constraints are defined as the followings:

$$\text{Constraint 1: } \left[\sum_{\theta=\theta_1}^{\theta_{N\theta}} \{(Sl_{T-in})_{\theta} - (Sl_{in})_{\theta}\}_{f_u}^2 / F_{C1} \right] - 1 \leq 0 \quad (5.14)$$

$$\text{Constraint 2: } \left[\sum_{\theta=\theta_1}^{\theta_{N\theta}} \{(Sl_{T-out})_{\theta} - (Sl_{out})_{\theta}\}_{f_u}^2 / F_{C2} \right] - 1 \leq 0 \quad (5.15)$$

$$\text{Constraint 3: } \left[\sum_{\theta=\theta_1}^{\theta_{N\theta}} \{(Sl_{T-in})_{\theta} - (Sl_{in})_{\theta}\}_{f_l}^2 / F_{C3} \right] - 1 \leq 0 \quad (5.16)$$

$$\text{Constraint 4: } \left[\sum_{\theta=\theta_1}^{\theta_{N\theta}} \{(Sl_{T-out})_{\theta} - (Sl_{out})_{\theta}\}_{f_l}^2 / F_{C4} \right] - 1 \leq 0 \quad (5.17)$$

where Sl denotes a slowness that expresses the relation between the wavenumber and angular frequency. It is evaluated at every angle and is reciprocal of phase velocity; $Sl = 1 / V_{phase} = k / \omega$. Sl_T means a slowness of target EFC, and Sl_{in} and Sl_{out} denote a slowness of inner and outer curves of EFC at the intermediate

design iteration. θ_{N_θ} is the number of angles for drawing the EFC. To match Sl with Sl_T during the optimization process, the optimizer keeps repeating the iteration until the convergence condition is satisfied. The method of moving asymptotes [84] is used as an optimization algorithm.

The sensitivity analysis for the objective function and the constraints can be implemented by using the below equations:

$$\frac{\partial}{\partial \chi_i} \left(\sum_{m=1}^{N_e} \chi_m (1 - \chi_m) / F_1 \right) = (1 - 2\chi_i) \quad (5.18)$$

$$\frac{\partial}{\partial \chi_i} \left(\left[\sum_{\theta=\theta_1}^{\theta_{N_\theta}} \{(Sl_T)_\theta - (Sl)_\theta\}^2 / F_C \right] - 1 \right) = -\frac{2}{\omega F_C} \sum_{\theta=\theta_1}^{\theta_{N_\theta}} \frac{\partial k_\theta}{\partial \chi_i} \{(Sl_T)_\theta - (Sl)_\theta\}. \quad (5.19)$$

Finally, the formulations for adjusting the deflection angles are arranged. With equations from (5.11) to (5.19), the design #1 and the design #2 can bring the optimized configuration showing two deflection angles in Fig. 5.3 and Fig. 5.4.

5.3.3 Optimal configurations of metamaterial unit cells

The optimized results according to the iterations are shown in Fig. 5.6. At the initial step, the unit cell configuration is identical with the one in Fig. 5.1(a). The

unit cell is discretized with 35×50 elements, and black and white colored elements denote an aluminum and air, respectively. EFCs are obtained by solving the eigenvalue problem in Section 2.1.2.

We can identify the difference between the target EFC (black solid lines) and the initial EFC shape (red and blue solid lines). The topology optimization method starts deforming the configuration as the iteration is repeated. The EFC gradually follows the aimed shape, and thus there appears a gray colored element to obey the constraints. However, when the convergence condition is almost satisfied, the optimization brings the well-designed results of which EFC is perfectly matched with the target EFC.

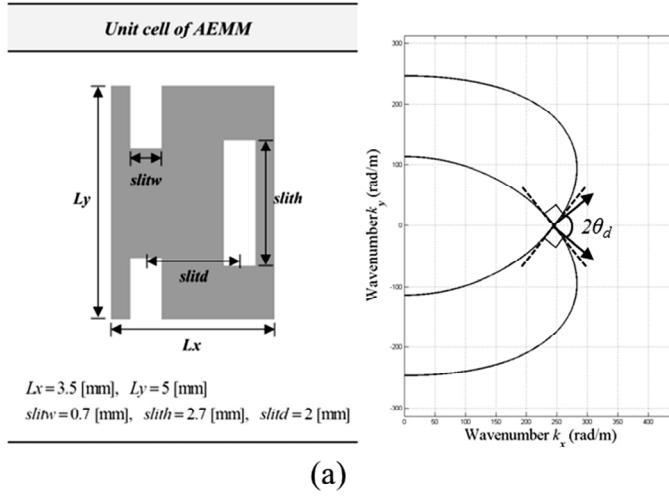
In Fig. 5.7, there is an iteration history for the objection function and four constrains. The Constraint 1 and the Constraint 3 show the similar tendency with respect to the progress of iterations. Likewise, the Constraint 2 and the Constraint 4 show the similar tendency. We can confirm that these constraints are well converged to the zero. For the objective function, especially at the beginning of iterations, the value of the objective function is increased even though it should be minimized. Because the initial unit cell is composed of elements whose design variables are $\chi_i = 1$ or $\chi_i = 0$, the value of the objective function is completely zero at the initial step. However, as four constraints play major roles to follow the target EFC, the value of the objective function starts increasing, caused by gray

elements. After that, when the EFC starts following the target shape, the value of the objective function undergoes decreasing. By updating the design variables, the objective function at the final step can be well minimized below than 0.04.

Fig. 5.8 reports the optimized results for the design #2 of which the deflection angle is $\theta_d = 31.1^\circ$. This case also shows the difference between the target EFC and the EFC shape in the beginning. However, they are finally overlapped as a consequence of the curve fitting optimization. As a result of design # 2, a new topology is formed. There are newly created holes in the designed unit cell shape and it is necessary to interpret how these affect the EFC. Therefore, we analyze the difference of the EFC model according to the presence or absence of the newly created holes. The newly created hole on the left side of the unit cell does not have a significant effect on the shape of the EFC. On the other hand, the newly created holes on the right side of the unit cell are slightly sensitive to the change of EFC at the k_x axis. An iteration history for the objective function and four constraints can be examined with the previously mentioned explanations for the design #1, as shown in Fig. 5.9.

5.4 Summary

The new metamaterial unit cells are reported in Chapter 5. Using the topology optimization method, it is confirmed that the deflection angle can be widened or be narrow comparing with the one in Chapter 3. With the effective medium having the target EFC shapes, the numerical simulations are conducted to verify the aimed deflection angles: $\theta_d = 43.7^\circ$ for the design #1 and $\theta_d = 31.1^\circ$ for the design #2. After the convergence of the topology optimization, the optimized configurations of metamaterial unit cells are reported and their EFCs are perfectly matched with the target EFCs. Chapter 5 explains that our proposing metamaterial systems demonstrating the conical refraction phenomenon can have the directional tunability. The achievement is based on the characteristic that the bulginess of EFC depends on the anisotropy factor. By controlling the anisotropy factor, we propose newly designed metamaterial unit cells. These systems are applicable to an appropriate location to protect certain area where the elastic waves should be prohibited.



✓ Case for $C_{12} = 0.1994e10$

✓ Case for $C_{12} = 0.8994e10$

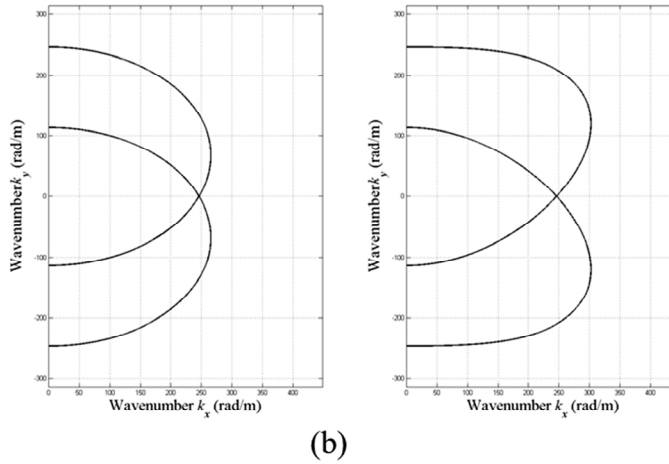


Figure 5.1 (a) The proposed anisotropic metamaterial unit cell and its EFC. (b)

EFCs of effective medium having $C_{12} = 0.1994 \times 10^{10}$ Pa or $C_{12} = 0.8994 \times 10^{10}$

Pa.

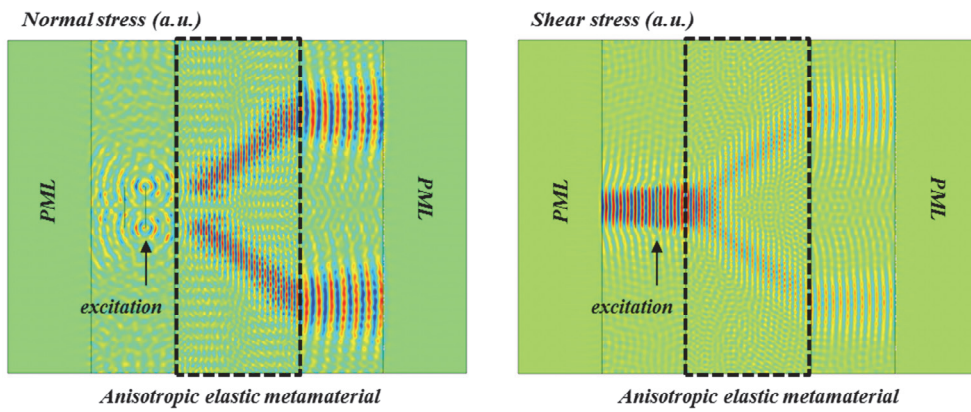


Figure 5.2 Normal and shear stress field distribution when the 90 kHz SH_0 wave incidents on the effective medium whose C_{12} has the value of 0.5994×10^{10} Pa.

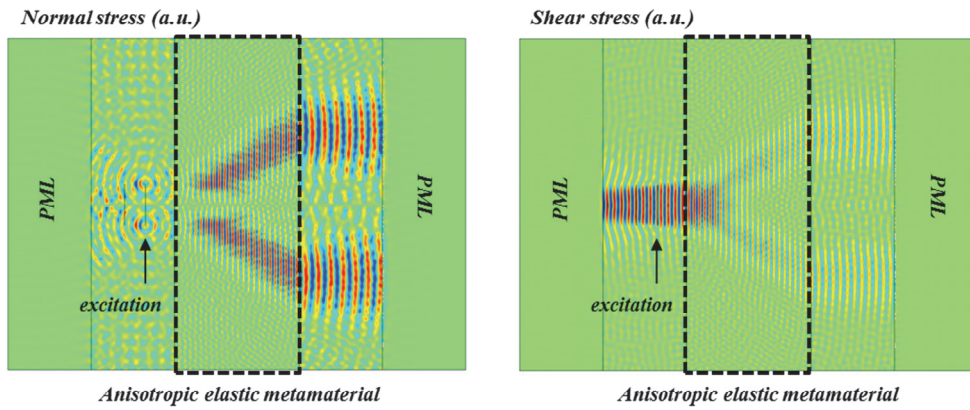


Figure 5.3 Normal and shear stress field distribution when the 90 kHz SH_0 wave incidents on the effective medium whose C_{12} has the value of 0.1994×10^{10} Pa.

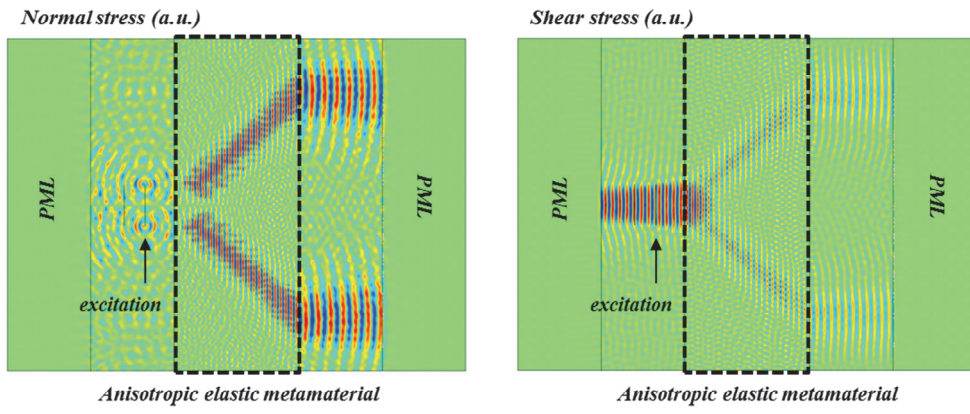


Figure 5.4 Normal and shear stress field distribution when the 90 kHz SH_0 wave incidents on the effective medium whose C_{12} has the value of 0.8994×10^{10} Pa.

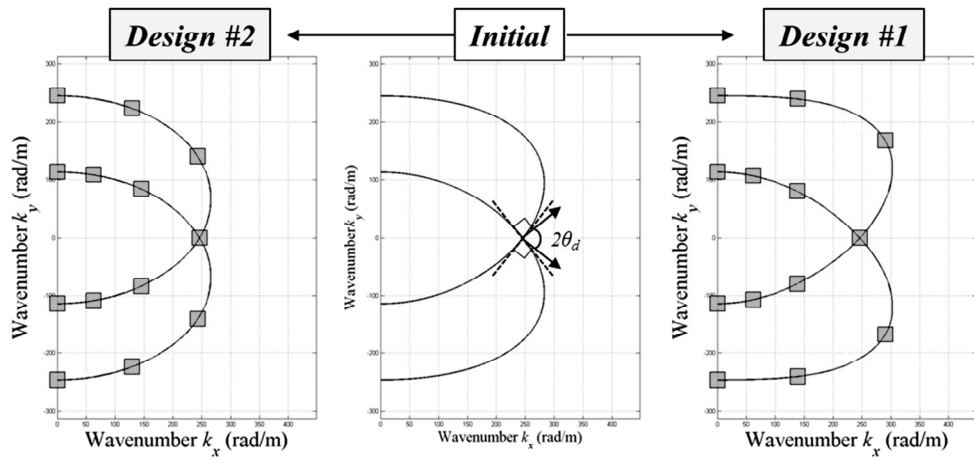


Figure 5.5 Design proposals for topology optimization: Design #1 is for the case that the deflection angle is 43.7° , and Design #2 is for the case that the deflection angle is 31.1° .

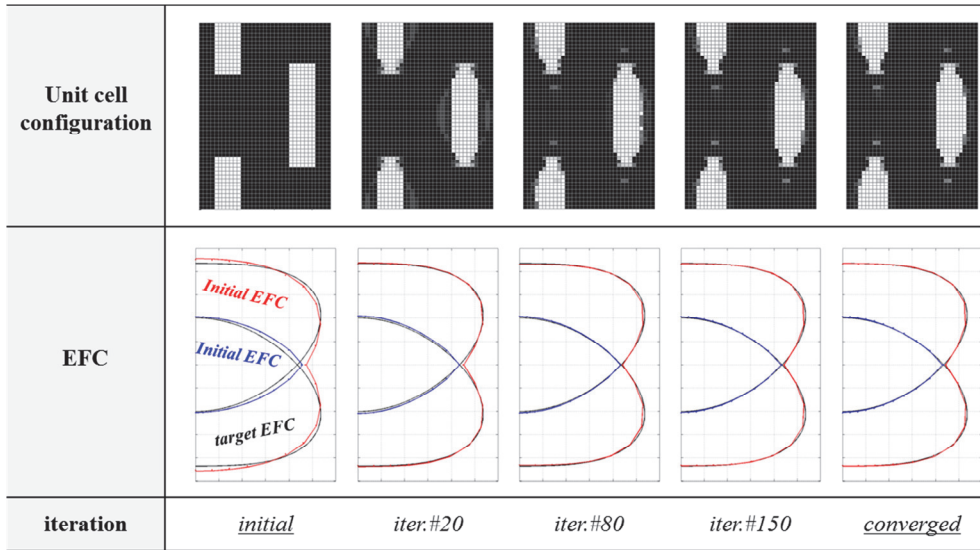


Figure 5.6 Topology optimization results of design #1. The unit cell configuration and EFC at 0, 20, 80, 150 and final iterations.

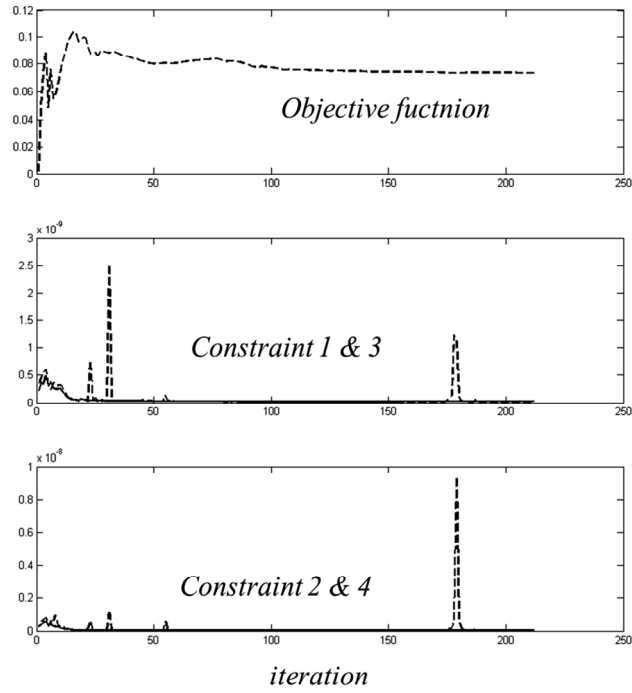


Figure 5.7 Iteration history of the objective function and four constraints for the design #1.

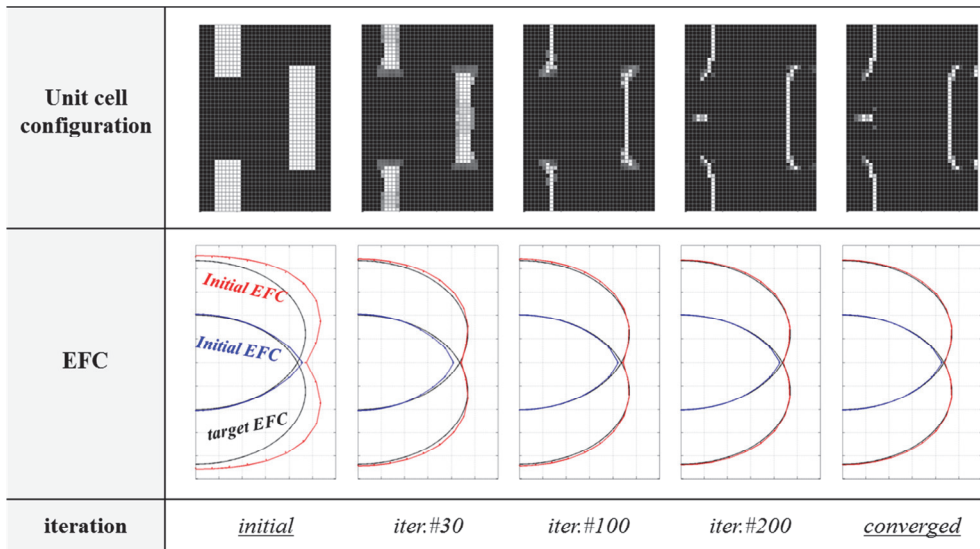


Figure 5.8 Topology optimization results of design #2. The unit cell configuration and EFC at 0, 30, 100, 200 and final iterations.

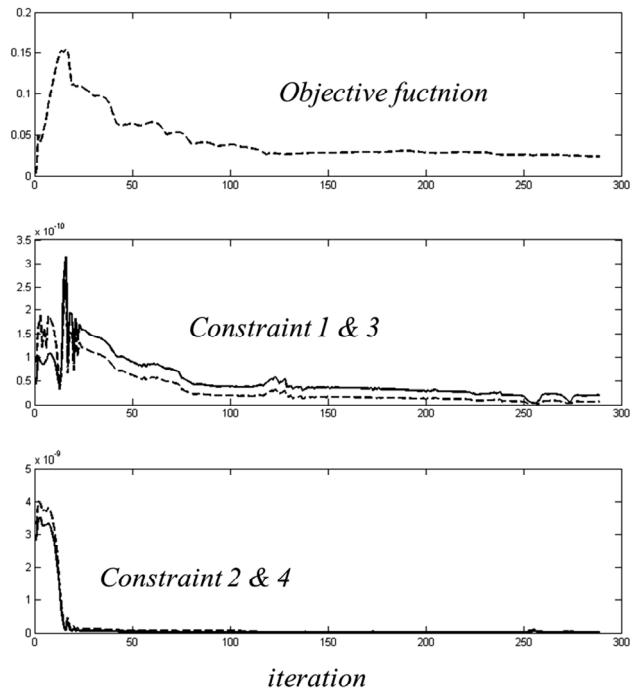


Figure 5.9 Iteration history of the objective function and four constraints for the design #2.

CHAPTER 6

CONCLUSIONS

An elastic anisotropic metamaterial is designed to produce the conical refraction. Elastic waves can be deflected into upward and downward directions inside the engineered metamaterial. The proposed system has an ability that deflects normally incident elastic waves rather than propagating in the incident direction.

In the thesis, three main objectives are categorized.

At first, we realize the elastic metamaterial plate demonstrating the conical refraction by using only aluminum, an isotropic metallic medium. Thus, it is highly applicable in many industrial devices and systems. The performance of conical refraction is verified with numerical simulations and experiments. Because the proposed metamaterial is composed of non-resonant type unit cells, it has very wide operational frequency range. The unit cell is elaborately designed to satisfy

the aimed anisotropy. This anisotropy can be fulfilled with a special relation between components of the effective property. To do so, a slit-inserted unit cell is suggested. The microfabricated elastic metamaterial hereby successfully shows the conical refraction.

Secondly, the manufactured elastic metamaterial is innovative in translocating mechanical stress waves. Among two newly generated paths inside the metamaterial, only one of them can be allowed to propagate elastic waves. When the wave exits the metamaterial slab, it propagates in the incident direction, the direction perpendicular to the slab. Thus, the mechanical stress wave initially propagating at a center of a plate before entering the metamaterial can behave as if being a teleportation after passing through the metamaterial. This translocation performance can be exploited for developing nondestructive testing, structural health monitoring and ultrasonic imaging technique.

Lastly, we use the topology optimization method to improve the directional tunability of the engineered metamaterial. The previously designed metamaterial can conically deflect elastic waves with a determined angle. On the other hand, the new metamaterial unit cells are introduced showing the deflection angles much wider or narrow than the previous case. The formulations for topology optimization are explained and well-applied to optimize the configuration. The objective function and constraints make an equi-frequency contour to follow the target shape.

A design domain is repeatedly updated by an optimization algorithm with mathematical procedures. There are two design results showing various deflection angles obtained by topology optimization.

The engineered metamaterial in the thesis is proposed for the first time, and can be actively utilized because of the good manufacturability and qualified performance. We have planned to conduct further studies to improve the ability of the anisotropic metamaterial and keep trying to find a way how to apply the system into current key industries.

APPENDIX A

SUPERCELL ANALYSIS IN TOPOLOGY

OPTIMIZATION OF PERIODIC STRUCTURES

A.1 Overview

Supercells formed by integer multiples of an original unit cell along its lattice axes are common, but there are also important situations requiring supercells formed by non-integer multiples of an original unit cell and its rotation with respect to its lattice axes. In these cases, not only dispersion branch folding, but also branch overlapping not found in common supercells, take place, which complicates the correct interpretation of band structures. In Appendix, we consider 45° -rotated augmented supercells and analyze why and how branch folding and overlapping take place. For the analysis, the relation between the first Brillouin zone of an original cell and that of the corresponding 45° -rotated augmented supercell is

investigated. The usefulness of the findings of this supercell-based dispersion analysis is demonstrated in unit cell design problems. Specifically, we show how to interpret correctly the dispersion curves of phononic crystals made of unit cells optimized by bandgap maximizing topology optimization when the optimized unit cells turn out to be 45° -rotated augmented supercells. Conversely, throughout design optimization iterations, the original period of a unit cell that is initially set at the beginning of design optimization can be maintained if branch overlapping is forced not to occur.

Appendix is organized as follows. In Appendix A.2, we reveal how the dispersion curves plotted with respect to the supercell match those plotted with respect to the original unit cell. In doing so, we also show that non-propagating branches appear in a certain wavevector region. Furthermore, we show how branch overlapping takes place in the supercell-based dispersion curves. Once the characteristics and origins of the dispersion curves plotted with respect to the supercell are analyzed, wave propagation in a PC structure can be correctly interpreted. In Appendix A.3, we show how the findings in Appendix A.2 can be utilized in practical phononic crystal design problems, especially for bandgap maximizing topology optimization problems. Through these problems, it can be demonstrated that the correct analysis of the dispersion curve in a 45° -rotated augmented supercell is important not only in the interpretation of optimized results but also in keeping the initially-set periodicity throughout optimization iterations.

A.2 Dispersion analysis in the 45°-rotated augmented supercell

When parameter studies involve the periods of Phononic Crystal (PC) unit cells, dispersion analysis with the supercell approach can be effective. A two-dimensional supercell is typically an augmented unit cell consisting of $n \times m$ ($n, m =$ positive integer) times the original unit cell. In this case, the directions of lattice axes are assumed to be unaltered. Earlier studies explain how to interpret the dispersion curves plotted by the supercell approach [85, 86]. If unit cell axes are also allowed or made to rotate as a result of parameter changes (in two or higher-dimensional cases only), the required supercell is not only augmented and but also rotated. Because of the axis rotation, the dispersion curves plotted with respect to an augmented, rotated supercell will look quite different from and become much more complicated than those plotted with respect to an augmented supercell without rotation.

As an example of the dispersion curve plotted with a rotated augmented supercell, let us consider Fig. A.1. Fig. A.1(a) shows a two-dimensional PC consisting of square unit cells with inclusions. As a design problem, one can consider altering band structures by changing the size of inclusions. Specifically, the square unit cell is to be optimized in which defined by the square dotted line in Fig. A.1(a). The 4 corner quadrants can vary in size (radius) while the central circular inclusion

remains unchanged. If the radius of the 4 quadrants becomes equal to the radius of the central circular inclusion, Fig. A.1(b) turns out to be the correct unit cell for the corresponding dispersion analysis. In this case, the unit cell shown in Fig. A.1(c) can be viewed as a 45°-rotated augmented supercell compared with the true unit cell in Figs. A.1(b). As a result, the dispersion curves plotted in Fig. A.1(c) become quite complicated and have overlapping branches over a range of wavevectors. In addition, it has been reported in practical engineering PC design studies that a 45°-rotated augmented supercell could be obtained as the results of optimization [78-80]. However, the analysis of the dispersion curve in a rotated augmented supercell requires further exploration. Our aim is to fully analyze the dispersion curve in a 45°-rotated augmented square supercell.

Fig. A.1(a) shows a two-dimensional PC, the unit cell of which is a square unit cell \mathbf{C} of size $d_u = d / \sqrt{2}$, and the lattice vectors $(\mathbf{e}_1, \mathbf{e}_2)$. The dispersion curves for the PC, analyzed with respect to \mathbf{C} , are shown in Fig. A.1(b) and were obtained by the finite element method for two-dimensional in-plane waves consisting of longitudinal-dominant and shear-dominant motions. For instance, the lowest and the second lowest branches appearing along $\Gamma - X$ (see the definition of these symbols in Fig. A.2(b)) denote the shear-dominant (“*SH-dominant*”) and longitudinal-dominant (“*L-dominant*”) wave modes, respectively. The PC in Fig. A.1(a) is made of an aluminum ($E = 70 \text{ GPa}$, $\nu = 0.34$, $\rho = 2,700 \text{ kg/m}^3$)

host and circular tungsten ($E = 360 \text{ GPa}$, $\nu = 0.27$, $\rho = 17,800 \text{ kg/m}^3$) inclusions of radius $0.3d$. Here, Young's modulus and Poisson's ratio are denoted by E and ν , respectively. For subsequent numerical analyses, $d = 0.02 \text{ m}$ is used.

As we attempt to analyze the dispersion curve of the same PC with respect to a 45° -rotated augmented supercell $\mathbf{C}_{\text{s-}45^\circ}$ of $d_s = d$, lattice vectors \mathbf{e}_{1S} and \mathbf{e}_{2S} ($|\mathbf{e}_{1S}| = |\mathbf{e}_{2S}| = d_s$) are introduced. If the Cartesian axes are assumed to be aligned with \mathbf{e}_{1S} and \mathbf{e}_{2S} , then $\mathbf{e}_{1S} = (d, 0)$, $\mathbf{e}_{2S} = (0, d)$, $\mathbf{e}_1 = (d, d)/2$, and $\mathbf{e}_2 = (-d, d)/2$. Fig. A.1(c) shows the dispersion curves analyzed with respect to the supercell $\mathbf{C}_{\text{s-}45^\circ}$. These curves appear quite complicated in comparison with those shown in Fig. A.1(b), analyzed with respect to \mathbf{C} .

To analyze the dispersion curves in the wavevector spaces corresponding to \mathbf{C} and $\mathbf{C}_{\text{s-}45^\circ}$, the reciprocal lattice vectors for \mathbf{C} and $\mathbf{C}_{\text{s-}45^\circ}$ are introduced in Fig. A.2(a): $\mathbf{b}_1 = 2\pi/d(1, 1)$, $\mathbf{b}_2 = 2\pi/d(-1, 1)$ for \mathbf{C} , $\mathbf{b}_{1S} = 2\pi/d(1, 0)$, and $\mathbf{b}_{2S} = 2\pi/d(0, 1)$ for $\mathbf{C}_{\text{s-}45^\circ}$. The 1st BZs corresponding to \mathbf{C} and $\mathbf{C}_{\text{s-}45^\circ}$ are plotted in Fig. A.2(b) with the reciprocal lattice vectors illustrated. Note that the 1st BZ of \mathbf{C} completely encloses the 1st BZ of $\mathbf{C}_{\text{s-}45^\circ}$. However, the orientations of

\mathbf{b}_{1S} and \mathbf{b}_{2S} are different from those of \mathbf{b}_1 and \mathbf{b}_2 . Therefore, the dispersion curves plotted with respect to the supercell \mathbf{C}_{S-45° require careful interpretations different from those for a one-dimensional supercell or two-dimensional augmented supercell without unit cell rotation. Such complexity in interpreting the dispersion curves with respect to \mathbf{C}_{S-45° comes from the cell rotation. We pay special attention to the effects of the cell rotation and give correct interpretations of the dispersion curves in Fig. A.1(c) with a reference to those in Fig. A.1(b).

To begin with, we first examine zone folding in order to interpret the dispersion curve plotted with respect to \mathbf{C}_{S-45° . Fig. A.3 graphically explains how the 1st BZ of \mathbf{C} (denoted \mathbf{Z}) is folded onto the 1st BZ of \mathbf{C}_{S-45° (denoted \mathbf{Z}_{S-45°). For the subsequent analysis, we introduce the notation (Γ, X, M) for \mathbf{Z} and (Γ_S, X_S, M_S) for \mathbf{Z}_{S-45° . Referring to Fig. A.3, the MX line in \mathbf{Z} is shown to be folded inside \mathbf{Z}_{S-45° and juxtaposed onto the $\Gamma_S M_S$ line. Along the ΓM line in \mathbf{Z} , the line segment $X_S M$ is folded inside \mathbf{Z}_{S-45° and juxtaposed onto the $X_S \Gamma$ line.

During the folding process, the $X_S M_S$ line serves as a folding line. Because we are mainly concerned with the dispersion curves along the $\Gamma_S - X_S - M_S - \Gamma_S$

path, the analysis of the folding mechanisms given above will be sufficient. Nevertheless, a complete picture of the folding mechanism of \mathbf{Z} onto $\mathbf{Z}_{\mathbf{S}-45^\circ}$ is illustrated in Fig. A.3. In summary,

$$\Gamma\text{X line of } \mathbf{Z} : \text{ same as } \Gamma_{\mathbf{S}}\text{M}_{\mathbf{S}} \text{ line of } \mathbf{Z}_{\mathbf{S}-45^\circ} . \quad (\text{A.1})$$

$$\text{MX line of } \mathbf{Z} : \text{ folded onto } \Gamma_{\mathbf{S}}\text{M}_{\mathbf{S}} \text{ line of } \mathbf{Z}_{\mathbf{S}-45^\circ} . \quad (\text{A.2})$$

$$\Gamma\text{X}_{\mathbf{S}} \text{ line of } \mathbf{Z} : \text{ same as } \Gamma_{\mathbf{S}}\text{X}_{\mathbf{S}} \text{ line of } \mathbf{Z}_{\mathbf{S}-45^\circ} . \quad (\text{A.3})$$

$$\text{X}_{\mathbf{S}}\text{M line of } \mathbf{Z} : \text{ folded onto } \text{X}_{\mathbf{S}}\Gamma_{\mathbf{S}} \text{ line of } \mathbf{Z}_{\mathbf{S}-45^\circ} . \quad (\text{A.4})$$

$$\text{X}_{\mathbf{S}}\text{M}_{\mathbf{S}} \text{ line of } \mathbf{Z}_{\mathbf{S}-45^\circ} : \text{ **folding line** } . \quad (\text{A.5})$$

From the summary statements (A.1) and (A.2), the following conclusions are drawn. First, the dispersion curves appearing for wavevectors lying along the $\Gamma - \text{X}$ and $\text{M} - \text{X}$ lines of \mathbf{Z} appear for wavevectors lying along $\Gamma_{\mathbf{S}} - \text{M}_{\mathbf{S}}$ of $\mathbf{Z}_{\mathbf{S}-45^\circ}$. This is illustrated in Fig. A.4. Similarly, Fig. A.5 illustrates how the dispersion curve for wavevectors along the $\text{X}_{\mathbf{S}} - \text{M}$ line of \mathbf{Z} appears for wavevectors lying along the $\Gamma_{\mathbf{S}} - \text{X}_{\mathbf{S}}$ line of $\mathbf{Z}_{\mathbf{S}-45^\circ}$. Finally, we can see that the overlapping of the dispersion curves for wavevectors lying along the $\text{X}_{\mathbf{S}} - \text{M}_{\mathbf{S}}$ line is due to statement (A.5). This is illustrated by the overlapping of dispersion curves along $\Gamma_{\mathbf{S}} - \text{M}_{\mathbf{S}}$ in Fig. A.4 and $\Gamma_{\mathbf{S}} - \text{X}_{\mathbf{S}}$ in Fig. A.5 at $\text{M}_{\mathbf{S}}$ and $\text{X}_{\mathbf{S}}$,

respectively.

Based on the analysis of the dispersion curves in the 1st BZ Z_{S-45° of the 45°-rotated augmented supercell, a peculiar phenomenon is revealed: the dispersion curves always overlap along the $X_S - M_S$ line. Referring to the supercell shown in Fig. A.1(c), overlapping will occur if the radius of the circular inclusion is exactly the same as the radius of four equal quadrants located in the corners. If the radius of the quadrants is varied to tailor the dispersion curves of the resulting PC made of square unit cells of period d , branch overlapping can occur along $X_S - M_S$. In fact, this overlapping phenomenon can be used as an indicator to identify an abrupt change in periodicity in the process of unit cell configuration optimization. In the next section, we demonstrate how this finding can be used in design optimization.

We also emphasize the importance of correct interpretation of the dispersion curves in $\Gamma_S - M_S$. A correct interpretation is crucial to tell if a wave mode belonging to a certain branch can be a non-propagating mode. To this end, consider wave simulations in a PC, shown in Fig. A.6. Waves are excited in the PC along the ξ direction, i.e. along the $\Gamma_S - M_S$ direction at two different frequencies, 55 kHz and 75 kHz. In this case, the dispersion curves are analyzed in the rotated augmented supercell. From the dispersion curve in Fig. A.4(b) equivalent to Fig.

A.1(c) for the $\Gamma_S - M_S$ line, the two wave modes at 55 kHz are marked by **A** (longitudinal-dominant) and **B** (shear-dominant). Likewise, the two wave modes at 75 kHz are marked by **C** (longitudinal-dominant) and **D** (shear-dominant). Because the wave modes at **A**, **B** and **C** originally belong to the wave modes defined over the $\Gamma_S - M_S$ line equivalent to the $\Gamma - X$ line, they can all be excited if proper wave motions are prescribed. On the other hand, the wave mode at **D** originates from the wave mode at **D'** belonging to a wave mode defined over the $M - X$ line. Therefore, the mode at **D** cannot be excited.

These arguments can be confirmed by numerical simulations shown in Figs. A.6(b) and A.6(c). COMSOL Multiphysics was used for the simulations. As illustrated in these figures, the excited wave at 55 kHz having longitudinal-dominant wave motion can propagate through the PC owing to the longitudinal wave mode at **A**. Similarly, the shear-dominant wave can propagate through the PC owing to the shear wave mode at **B**. However, in case of shear wave excitation at 75 kHz, the PC stops its propagation because the wave mode at **D** originates from the wave mode at **D'** having a wavevector along the $M - X$ line.

A.3 Application in topology optimization of phononic crystals

To illustrate why analysis of the 45°-rotated augmented supercell is critical in engineering PCs, we consider the topology optimization of PC unit cells for bandgap maximization. In these problems, optimized results may not maintain the original period initially set up at the beginning of optimization, i.e. the optimized results are indeed designed in a 45°-rotated augmented supercell different from the original unit cell. Using the analysis given in Appendix A.2, therefore, we should be able to preserve the original periodicity condition throughout optimization iterations and correctly interpret the optimized results.

Because similar bandgap maximization problems were previously studied [78-80], optimization histories and numerical issues such as solution convergence are not investigated in this Appendix. We simply present the optimized result as shown in Fig. A.7(b). Comparing bandgap sizes before and after optimization in Fig. A.7, a considerable increase in size is observed after optimization was completed. The issue is that the optimized configuration turns out to be based on the 45°-rotated unit cell having a reduced period of $d/\sqrt{2}$, marked as C^{after} in Fig. A.7(b). The unit cell $C^{initial}$ initially chosen at the beginning of the optimization should be viewed as a 45°-rotated supercell, marked by $C_{S-45^\circ}^{after}$ for the optimized configuration in Fig. A.7(b). If we take $C^{after}|_{\text{Fig. A.7(b)}} = C|_{\text{Fig. A.1}}$ and

$C_{S-45^\circ}^{after} \Big|_{\text{Fig. A.7(b)}} = C_{S-45^\circ} \Big|_{\text{Fig. A.1}}$, then the findings of Appendix A.2 such as branch overlapping, the appearance of a non-propagating mode, etc., are directly applicable to the results shown in Fig. A.7(b). For instance, the dispersion curve of the optimized unit cell along the $M_S - \Gamma_S$ line is interpreted as the superposition of two dispersion curves along the $X - \Gamma$ and $X - M$ lines for C^{after} (see Fig. A.7(c)).

While the optimized results in Fig. A.7(b) can be interpreted correctly by the analysis given in Appendix A.2, it is also useful to perform optimization with the original periodicity unaltered. If the period is reduced, a different optimal solution could be found. Therefore, the selection of an initial period for design may become less meaningful. For this reason, a method to preserve the original periodicity throughout optimization iterations is presented in the subsequent discussions.

In developing a method to preserve the original periodicity, it is recalled that branch overlapping takes place if the period of an optimized PC is altered to form a 45°-rotated augmented supercell. Fig. A.7(b) also indicates that branch overlapping occurs along the $X_S - M_S$ region. Therefore, branch overlapping can be viewed as an indicator of altered periodicity.

Our proposition for preserving the original periodicity is to use the following

measure, $G = \sum_{\mathbf{k}=X_S}^{k=M_S} \omega(\mathbf{k}, 2) - \sum_{\mathbf{k}=X_S}^{k=M_S} \omega(\mathbf{k}, 1)$. The measure G signifies an area between the 1st and 2nd branches in the $X_S - M_S$ region. Using the proposed G , one can add the following constraint equation to the formulation given by Section 5.2 to maintain the original periodicity:

$$\text{Constraint 3: } G_{iteration} / G_{initial} \geq \alpha, \quad (\text{A.6})$$

where $G_{initial}$ is the value of G for the initial PC, $G_{iteration}$ is the value of G evaluated at every iteration step, and α is a pre-selected positive constant introduced to control the gap between the lowest two branches in the $X_S - M_S$ region. The effects of α on optimized results may be examined numerically. While the use of equation (A.6) does not complicate the optimization formulation, it can effectively maintain the original periodicity.

To verify the effectiveness of the periodicity-preserving methodology, let us revisit the bandgap maximization for the PC shown in Fig. A.7(a). The optimized unit cell without the periodicity-control strategy was shown to have an altered periodicity as in Fig. A.7(b). On the other hand, the optimized unit cell configurations obtained with the additional constraint of equation (A.6) maintains the original periodicity without branch overlapping in the $X_S - M_S$ region, as shown in Fig. A.8.

Certainly, the optimized unit cells are affected by the value of α ; the larger α is, the smaller the bandgap size between the 2nd and 3rd branches becomes. Because the mechanism of the change in periodicity is investigated in Appendix A.2, the use of equation (A.6) is found to be effective.

Fig. A.9 compares iteration histories for the cases with and without the periodicity controlling scheme. To indicate the occurrence of branch overlapping during the optimization procedure, we plot $G_{iteration} / G_{initial}$ in the figures. While $G_{iteration} / G_{initial}$ approaches zero when equation (A.6) is not used, $G_{iteration} / G_{initial}$ remains larger than zero if the periodicity control scheme is employed.

A.4 Summary

When the dispersion relations for phononic crystals made of original unit cells \mathbf{C} are analyzed with respect to a 45°-rotated augmented supercell \mathbf{C}_{S-45° , they become quite complicated due to branch folding and overlapping. The complexity is found to result from the 45° rotation and the branch folding and overlapping mechanisms were fully investigated in this Appendix. By identifying the sequential folding process of \mathbf{Z} onto \mathbf{Z}_{S-45° , it was possible to identify which parts of the dispersion curves plotted with respect to the $\Gamma - X - M - \Gamma$ path of \mathbf{Z} become those plotted with respect to the path of $\Gamma_S - X_S - M_S - \Gamma_S$ of \mathbf{Z}_{S-45° . After the folding and overlapping phenomena were investigated, it was demonstrated how to utilize the findings from the investigation in the topology optimization problems of phononic crystals. The first application was in the interpretation of the dispersion curves calculated with respect to \mathbf{C}_{S-45° , although the initial unit cell \mathbf{C} was selected for the optimization set-up. The second application was in maintaining the original unit cell \mathbf{C} throughout optimization iterations. Although the present case study was concerned with bandgap maximization, the interpretation of the dispersion curves in \mathbf{C}_{S-45° and the suggested periodicity-preserving formulation can be also used in other types of optimization problems involving phononic crystals. Furthermore, by extending the analysis method developed for 45°-rotated supercells, the other symmetry types of supercells can be equally treated.

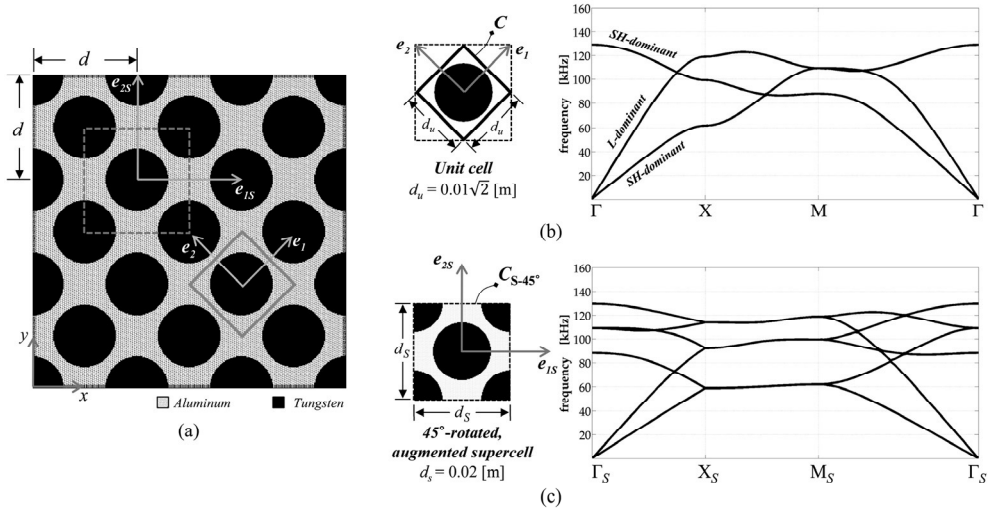


Figure A.1 (a) The two-dimensional phononic crystal consisting of an aluminum host and tungsten inclusions. (b) The original unit cell C and the dispersion curves with respect to C . (c) The 45° -rotated augmented supercell C_{S-45° and the dispersion curves with respect to C_{S-45° .

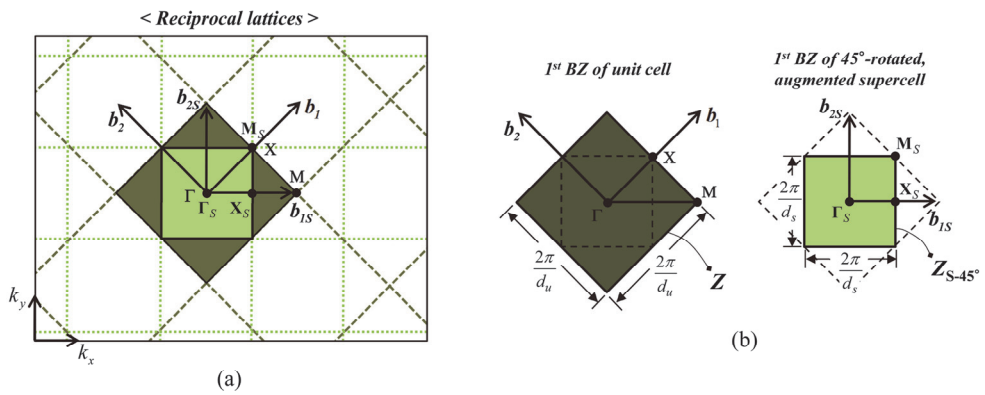


Figure A.2 (a) The reciprocal lattices and (b) the 1st Brillouin Zones (BZs) corresponding to the original unit cell C and the 45°-rotated augmented supercell C_{S-45° . The 1st BZs are marked as Z of C and Z_{S-45° of C_{S-45° .

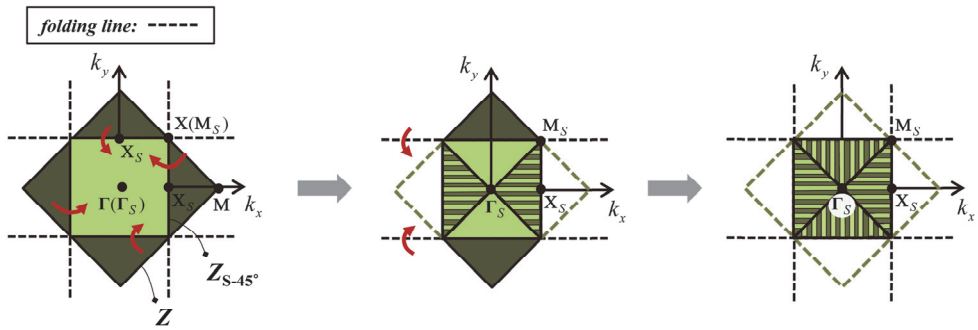


Figure A.3 The illustration of a folding mechanism of Z_{S-45° onto Z .

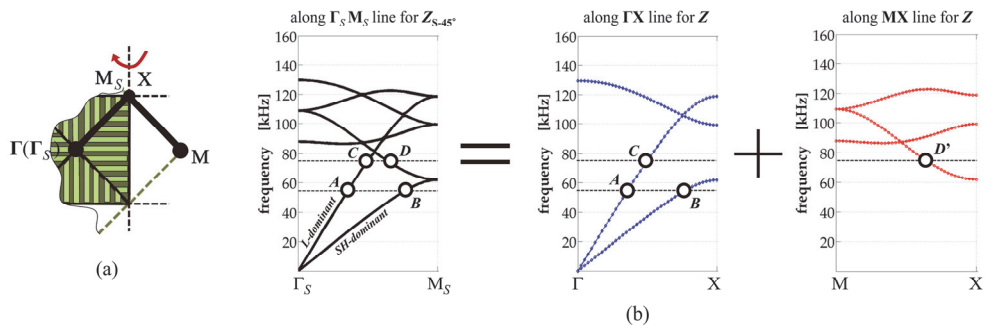


Figure A.4 (a) The illustration of a folding process, especially when the MX line of Z is folded onto the $\Gamma_S M_S$ line of Z_{S-45° . (b) Comparison of the dispersion curves along the $\Gamma_S M_S$ line for Z_{S-45° and the ΓX & MX lines for Z .

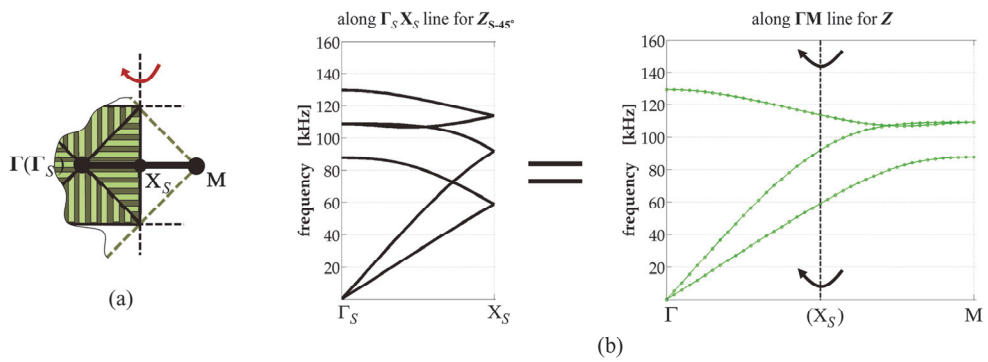


Figure A.5 (a) The illustration of a folding process, especially when that the ΓM line of Z is folded onto the $\Gamma_S X_S$ line of Z_{s-45° . (b) Comparison of the dispersion curves along the $\Gamma_S X_S$ line for Z_{s-45° and the ΓM line for Z .

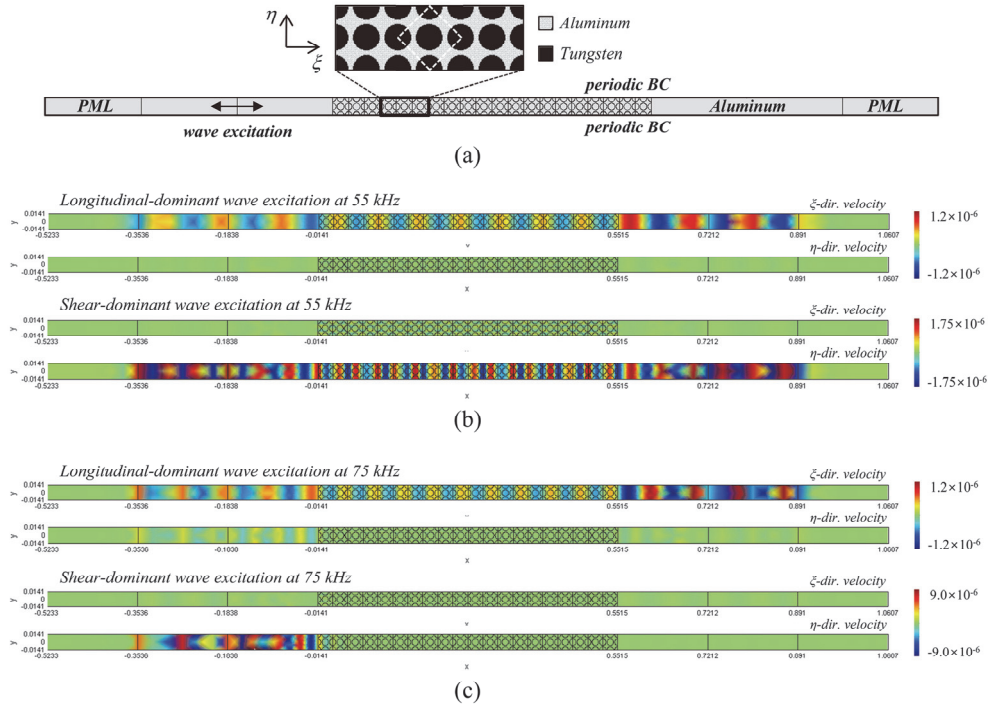


Figure A.6 The numerical simulation to verify whether the modes at *A*, *B*, *C* and *D* in Fig. A.4(b) can propagate or not through a two-dimensional PC analyzed with respect to the 45°-rotated augmented supercell. (a) Simulation model. The velocity-field plots at the (b) 55 kHz and (c) 75 kHz excitation.

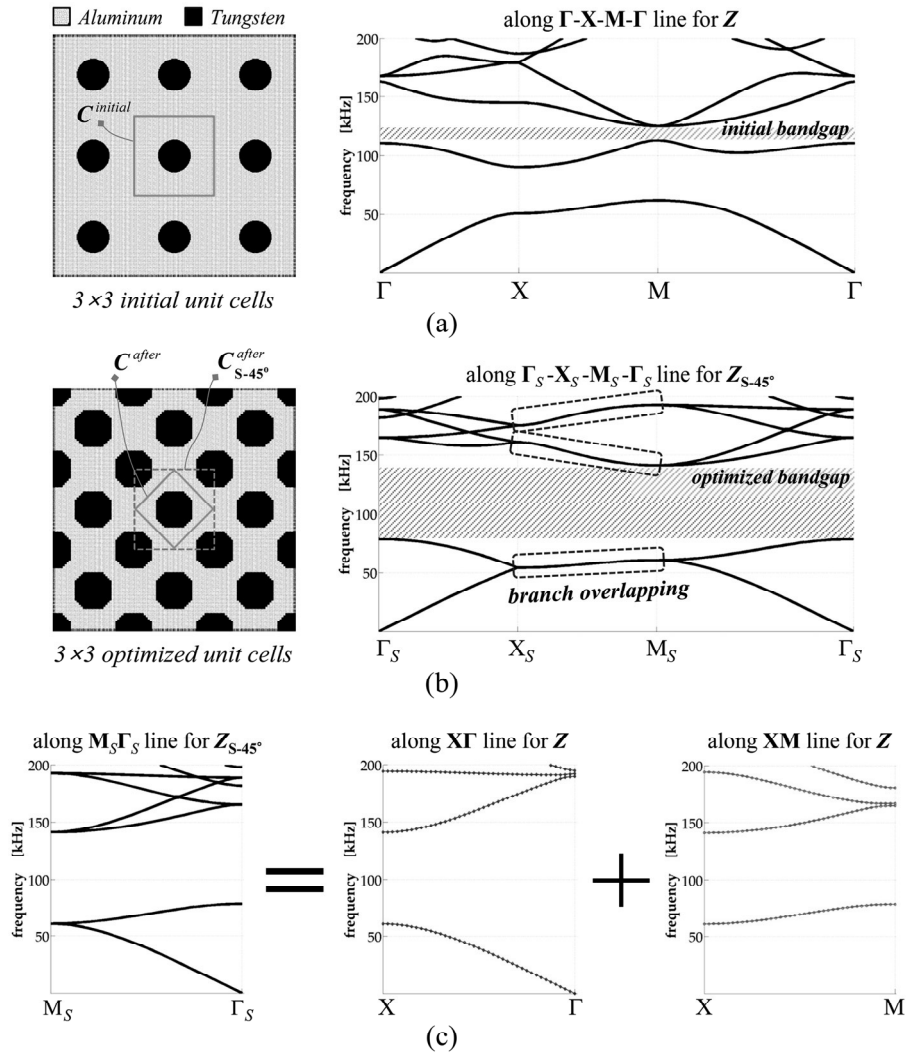


Figure A.7 Topology optimization of a two-dimensional PC for bandgap maximization. (a) Initial and (b) optimal configurations and the corresponding dispersion curves. (c) Comparison of the dispersion curves along the $M_S\Gamma_S$ line for $Z_{S,45^\circ}$ and the $X\Gamma$ & XM lines for Z .

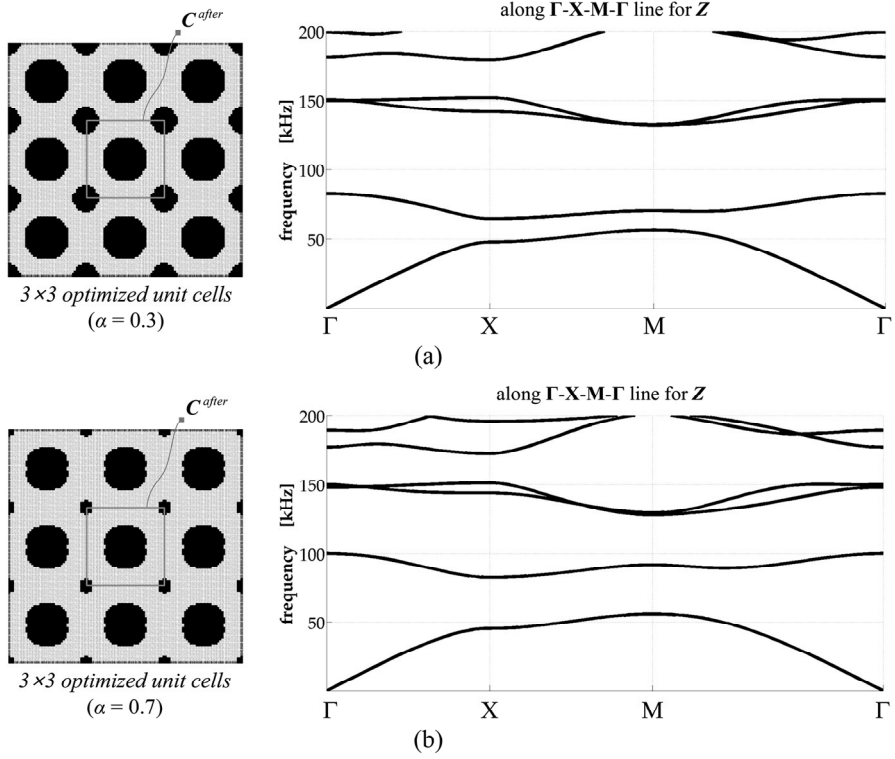
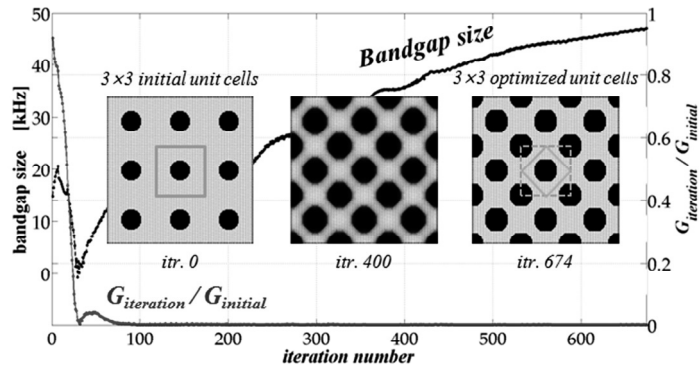


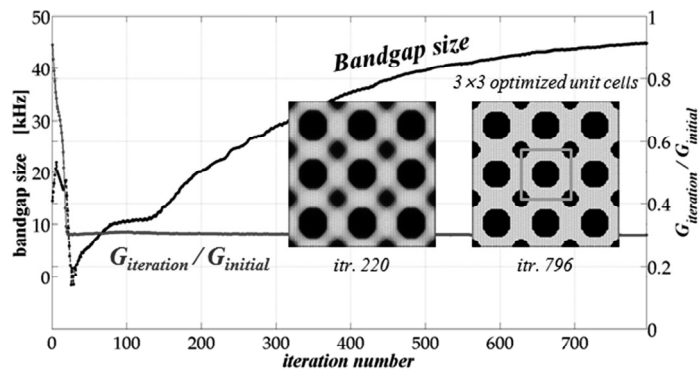
Figure A.8 The optimized configuration obtained by the periodicity-controlling bandgap-maximizing topology optimization with (a) $\alpha = 0.3$ and (b) $\alpha = 0.7$.

✓ *Iteration history for the case of wo/ periodicity-preserving methodology*



(a)

✓ *Iteration history for the case of w/ periodicity-preserving methodology*



(b)

Figure A.9 The iteration histories for the bandgap maximizing topology optimization (a) without and (b) with the periodicity-preserving methodology maintaining the original unit cell configuration for the case of $\alpha = 0.3$.

REFERENCES

- [1] J.O.Vasseur, P.A. Deymier, B. Chenni, B. Djafari-Rouhani, L. Dobrzynski, D. Prevost, Experimental and theoretical evidence for the existence of absolute acoustic band gaps in two-dimensional solid phononic crystals, *Phys. Rev. Lett.* 86 (2001) 3012.
- [2] E. Kim, J. Yang, Wave propagation in single column woodpile phononic crystals: Formation of tunable band gaps, *J. Mech. Phys. Solids.* 71 (2014) 33-45.
- [3] B.K. Henderson, K.I. Maslov, V.K. Kinra, Experimental investigation of acoustic band structures in tetragonal periodic particulate composite structures, *J. Mech. Phys. Solids.* 49 (2001) 2369-2383.
- [4] M.K. Lee, P.S. Ma, I.K. Lee, H.W. Kim, Y.Y. Kim, Negative refraction experiments with guided shear-horizontal waves in thin phononic crystal plates, *Appl. Phys. Lett.* 98 (2011) 011909.
- [5] S. Yang, J.H. Page, Z. Liu, M.L. Cowan, C.T. Chan, P. Sheng, Focusing of sound in a 3D phononic crystal, *Phys. Rev. Lett.* 93 (2004) 024301.
- [6] H. Chandra, P.A. Deymier, J.O. Vasseur, Elastic wave propagation along waveguides in three-dimensional phononic crystals, *Phys. Rev. B* 70 (2004) 054302.
- [7] Y. Pennec, B. Djafari-Rouhani, J.O. Vasseur, A. Khelif, P.A. Deymier, Tunable filtering and demultiplexing in phononic crystals with hollow cylinders, *Phys.*

- Rev. E 69 (2004) 046608.
- [8] J.H. Oh, Y.J. Kim, Y.Y. Kim, Wave attenuation and dissipation mechanisms in viscoelastic phononic crystals, *J. Appl. Phys.* 113 (2013) 106101.
- [9] T. Ma, T. Chen, X. Wang, Y. Li, P. Wang, Band structures of bilayer radial phononic crystal plate with crystal gliding, *J. Appl. Phys.* 116 (2014) 104505.
- [10] L. Jing, J.H. Wu, D. Guan, N. Gao, Multilayer-split-tube resonators with low-frequency band gaps in phononic crystals, *J. Appl. Phys.* 116 (2014) 103514.
- [11] R. Pourabolghasem, A. Khelif, S. Mohammadi, A.A. Eftekhar, A. Adibi, Physics of band-gap formation and its evolution in the pillar-based phononic crystal structures, *J. Appl. Phys.* 116 (2014) 013514.
- [12] P. Huang, Y. Yao, F. Wu, X. Zhang, Numerical study of Lamb waves band structure in one-dimensional phononic crystal slabs with the anti-symmetric boundary structure, *J. Appl. Phys.* 115 (2014) 063510.
- [13] Z. Hou, B.M. Assouar, Opening a band gap in the free phononic crystal thin plate with or without a mirror plane, *J. Phys. D: Appl. Phys.* 41 (2008) 215102.
- [14] J.C. Hsu, Local resonances-induced low-frequency band gaps in two-dimensional phononic crystal slabs with periodic stepped resonators, *J. Phys. D: Appl. Phys.* 44 (2011) 055401.
- [15] C. Goffaux, J.P. Vigneron, Theoretical study of a tunable phononic band gap system, *Phys. Rev. B* 64 (2001) 075118.
- [16] T. Trifonov, L.F. Marsal, A. Rodriguez, J. Pallares, R. Alcubilla, Effects of symmetry reduction in two-dimensional square and triangular lattices, *Phys.*

- Rev. B 69 (2004) 235112.
- [17] J. Li, C. Chan, Double-negative acoustic metamaterial, *Phys. Rev. E* 70 (2004) 055602.
- [18] D.R. Smith, W.J. Padilla, D. Vier, S.C. Nemat-Nasser, S. Schultz, Composite medium with simultaneously negative permeability and permittivity, *Phys. Rev. Lett.* 84 (2000) 4184.
- [19] Y. Ding, Z. Liu, C. Qiu, J. Shi, Metamaterial with simultaneously negative bulk modulus and mass density, *Phys. Rev. Lett.* 99 (2007) 093904.
- [20] H.J. Lee, H.W. Kim, Y.Y. Kim, Far-field subwavelength imaging for ultrasonic elastic waves in a plate using an elastic hyperlens, *Appl. Phys. Lett.* 98 (2011) 241912.
- [21] J. Li, L. Fok, X. Yin, G. Bartal, X. Zhang, Experimental demonstration of an acoustic magnifying hyperlens, *Nat. Mater.* 8 (2009) 931-934.
- [22] S.A. Cummer, D. Schurig, One path to acoustic cloaking, *New J. Phys.* 9 (2007) 45.
- [23] Y. Chen, H. Liu, M. Reilly, H. Bae, M. Yu, Enhanced acoustic sensing through wave compression and pressure amplification in anisotropic metamaterials, *Nat. Commun.* 5 (2014) 5247.
- [24] J.L. Rose, *Ultrasonic waves in solid media* (Cambridge university press, 2004).
- [25] B.A. Auld, *Acoustic fields and waves in solids* (Wiley-Interscience, 1973).
- [26] A.N. Norris, Acoustic axes in elasticity, *Wave Motion* 40 (2004) 315-328.
- [27] V. Vavryčuk, Inversion for weak triclinic anisotropy from acoustic axes, *Wave*

- Motion 50 (2013) 1271-1282.
- [28] V. Vavryčuk, Ray tracing in anisotropic media with singularities, *Geophys. J. Int.* 145 (2001) 265-276.
- [29] A. Yariv, P. Yeh, *Optical waves in crystals* (Wiley-Interscience, 1984).
- [30] R.G. Payton, Wave propagation in a restricted transversely isotropic elastic solid whose slowness surface contains conical points, *Q. J. Mech. Appl. Math.* 45 (1992) 183-197.
- [31] J. de Klerk, M.J.P. Musgrave, Internal conical refraction of transverse elastic waves in a cubic crystal, *Proc. Phys. Soc. B* 68 (1955) 81.
- [32] H. McSkimin, W. Bond, Conical refraction of transverse ultrasonic waves in quartz, *J. Acoust. Soc. Am.* 39 (1966) 499-505.
- [33] T. Srinivasan, G. Lakshmi, Internal conical refraction of elastic waves in tetragonal crystals, *J. Phys. D: Appl. Phys.* 6 (1973) 305.
- [34] M. Berry, Conical diffraction asymptotics: fine structure of Poggendorff rings and axial spike, *J. Opt. A: Pure Appl. Opt.* 6 (2004) 289.
- [35] M. Berry, M. Jeffrey, J. Lunney, Conical diffraction: observations and theory, *Proc. R. Soc. A* 462 (2006) 1629-1642.
- [36] C. Phelan, K. Ballantine, P. Eastham, J. Donegan, J. Lunney, Conical diffraction of a Gaussian beam with a two crystal cascade, *Opt. Express* 20 (2012) 13201-13207.
- [37] K. Ballantine, J. Donegan, P. Eastham, Conical diffraction and the dispersion surface of hyperbolic metamaterials, *Phys. Rev. A* 90 (2014) 013803.

- [38] R.L. Chern, P.H. Chang, Wave propagation in pseudo-chiral media: generalized Fresnel equations, *J. Opt. Soc. Am. B* 30 (2013) 552-558.
- [39] P.H. Chang, C.Y. Kuo, R.L. Chern, Wave splitting and double-slit like interference by a pseudo-chiral metamaterial slab, *J. Phys. D: Appl. Phys.* 48 (2015) 295103.
- [40] Q. Guo, W. Gao, J. Chen, Y. Liu, S. Zhang, Line degeneracy and strong spin-orbit coupling of light with bulk bianisotropic metamaterials, *Phys. Rev. Lett.* 115 (2015) 067402.
- [41] M.J. Lowe, D.N. Alleyne, P. Cawley, Defect detection in pipes using guided waves, *Ultrasonics* 36 (1998) 147-154.
- [42] H.W. Kim, Y.E. Kwon, S.H. Cho, Y.Y. Kim, Shear-horizontal wave-based pipe damage inspection by arrays of segmented magnetostrictive patches, *IEEE Trans. Ultrason. Ferroelectr. Freq. Control* 58 (2011) 2689-2698.
- [43] F. Yan, R.L. Royer, J.L. Rose, Ultrasonic guided wave imaging techniques in structural health monitoring, *J. Intell. Mater. Syst. Struct.* 21 (2010) 377-384.
- [44] A. Velichko, P.D. Wilcox, Guided wave arrays for high resolution inspection, *J. Acoust. Soc. Am.* 123 (2008) 186-196.
- [45] J.J. Chen, B. Bonello, Z.L. Hou, Plate-mode waves in phononic crystal thin slabs: mode conversion, *Phys. Rev. E* 78 (2008) 036609.
- [46] Y.K. Ahn, J.H. Oh, P.S. Ma, Y.Y. Kim, Dispersion analysis with 45°-rotated augmented supercells and applications in phononic crystal design, *Wave Motion* 61 (2016) 63-72.

- [47] L. Brillouin, Wave propagation in periodic structures (Dover, 1953).
- [48] C. Kittel, Introduction to solid state physics (Wiley, 2005).
- [49] H.J. Lee, Effective-property characterization of elastic metamaterials for advanced wave tailoring, Ph.D. thesis, Seoul National University (2014).
- [50] Y.Y. Kim, Y.E. Kwon, Review of magnetostrictive patch transducers and applications in ultrasonic nondestructive testing of waveguides, *Ultrasonics* 62 (2015) 3-19.
- [51] J.K. Lee, H.W. Kim, Y.Y. Kim, Omnidirectional Lamb waves by axisymmetrically-configured magnetostrictive patch transducer, *IEEE Trans. Ultrason. Ferroelectr. Freq. Control* 60 (2013) 1928-1934.
- [52] H.J. Lee, J.K. Lee, Y.Y. Kim, Elastic metamaterial-based impedance-varying phononic bandgap structures for bandpass filters, *J. Sound Vib.* 353 (2015) 58-74.
- [53] M.H. Lu, C. Zhang, L. Feng, J. Zhao, Y.F. Chen, Y.W. Mao, J. Zi, Y.Y. Zhu, S.N. Zhu, N.B. Ming, Negative birefracton of acoustic waves in a sonic crystal. *Nat. Mater.* 6 (2007) 744-748.
- [54] R. Gaji, R. Meisels, F. Kuchar, K. Hingerl, Refraction and rightness in photonic crystals, *Opt. Express* 13 (2005) 8596-8605.
- [55] H. Lee, J.H. Oh, Y.Y. Kim, Multiple beam splitting in elastic phononic crystal plates, *Ultrasonics* 56 (2015) 178-182.
- [56] V.G. Veselago, The electrodynamics of substances with simultaneously negative values of ϵ and μ , *Sovi. Phys. Usp.* 10 (1968) 509.

- [57] A. Sukhovich, L. Jing, J.H. Page, Negative refraction and focusing of ultrasound in two-dimensional phononic crystals, *Phys. Rev. B* 77 (2008) 014301.
- [58] P. Parimi, W. Lu, P. Vodo, J. Sokoloff, J. Derov, S. Sridhar, Negative refraction and left-handed electromagnetism in microwave photonic crystals, *Phys. Rev. Lett.* 92 (2004) 127401.
- [59] R. Zhu, X. Liu, G. Hu, C. Sun, G. Huang, Negative refraction of elastic waves at the deep-subwavelength scale in a single-phase metamaterial, *Nat. Commun.* 5 (2014) 5510.
- [60] Y. Xie, W. Wang, H. Chen, A. Konneker, B.I. Popa, S.A. Cummer, Wavefront modulation and subwavelength diffractive acoustics with an acoustic metasurface, *Nat. Commun.* 5 (2014) 5553.
- [61] C.J. Rupp, A. Evgrafov, K. Maute, M.L. Dunn, Design of phononic materials/structures for surface wave devices using topology optimization, *Struct. Multidisc. Optim.* 34 (2007) 111-121.
- [62] P.I. Borel, A. Harpøth, L.H. Frandsen, M. Kristensen, P. Shi, J.S. Jensen, O. Sigmund, Topology optimization and fabrication of photonic crystal structures, *Opt. Express* 12 (2004) 1996-01.
- [63] J.S. Jensen, O. Sigmund, Topology optimization of photonic crystal structures: a high-bandwidth low-loss T-junction waveguide, *J. Opt. Soc. Am. B* 22 (2005) 1191-98.
- [64] Y. Watanabe, N. Ikeda, Y. Takata, Y. Kitagawa, N. Ozaki, Y. Sugimoto, K.

- Asakawa, Topology optimization of a wavelength-selective Y-junction for 2D photonic crystal waveguides, *J. Phys. D: Appl. Phys.* 41 (2008) 175109.
- [65] W.R. Frei, D.A. Tortorelli, H.T. Johnson, Topology optimization of a photonic crystal waveguide termination to maximize directional emission, *Appl. Phys. Lett.* 86 (2005) 111114.
- [66] Y. Watanabe, N. Ikeda, Y. Sugimoto, Y. Takata, Y. Kitagawa, Topology optimization of waveguide bends with wide, flat bandwidth in air-bridge-type photonic crystal slabs, *J. Appl. Phys.* 101 (2007) 113108.
- [67] R. Matzen, J.S. Jensen, O. Sigmund, Topology optimization for transient response of photonic crystal structures, *J. Opt. Soc. Am. B* 27 (2010) 2040-50.
- [68] F. Wang, J.S. Jensen, O. Sigmund, Robust topology optimization of photonic crystal waveguides with tailored dispersion properties, *J. Opt. Soc. Am. B* 28 (2011) 387-97.
- [69] Y. Watanabe, N. Ikeda, Y. Takata, Y. Kitagawa, N. Ozaki, Y. Sugimoto, K. Asakawa, Wideband operation of 2D photonic crystal directional coupler with topology optimized waveguide bends, *J. Nonlinear Opt. Phys. Mater.* 19 (2010) 543-50.
- [70] L.H. Frandsen, A. Harpøth, P.I. Borel, M. Kristensen, J.S. Jensen, O. Sigmund, Broadband photonic crystal waveguide 60° bend obtained utilizing topology optimization, *Opt. Express* 12 (2004) 5916-21.
- [71] J. Du, N. Olhoff, Topological design of freely vibrating continuum structures for maximum values of simple and multiple eigenfrequencies and frequency

- gaps, *Struct. Multidisc. Optim.* 34 (2007) 91-110.
- [72] O. Sigmund, J.S. Jensen, Systematic design of phononic band-gap materials and structures by topology optimization, *Philos. Trans. R. Soc. London, Ser. A* 361 (2003) 1001-1019.
- [73] S. Halkjær, O. Sigmund, J.S. Jensen, Maximizing band gaps in plate structures, *Struct. Multidisc. Optim.* 32 (2006) 263-75.
- [74] S.J. Cox, D.C. Dobson, Band structure optimization of two-dimensional photonic crystals in H-polarization, *J. Comput. Phys.* 158 (2000) 214-24.
- [75] M.I. Hussein, K. Hamza, G.M. Hulbert, K. Saitou, Optimal synthesis of 2D phononic crystals for broadband frequency isolation, *Waves Random Complex Medium* 17 (2007) 491-510.
- [76] G.A. Gazonas, D.S. Weile, R. Wildman, A. Mohan, Genetic algorithm optimization of photonic bandgap structures, *Int. J. Solids Struct.* 43 (2006) 5851-66.
- [77] S.J. Cox, D.C. Dobson, Maximizing band gaps in two-dimensional photonic crystals, *SIAM J. Appl. Math.* 59 (1999) 2108-20.
- [78] C.Y. Kao, S. Osher, E. Yablonovitch, Maximizing band gaps in two-dimensional photonic crystals by using level set methods, *Appl. Phys. B* 81 (2005) 235-244.
- [79] O.R. Bilal, M.I. Hussein, Ultrawide phononic band gap for combined in-plane and out-of-plane waves, *Phys. Rev. E* 84 (2011) 065701.
- [80] H.W. Dong, X.X. Su, Y.S. Wang, C. Zhang, Topological optimization of two-

- dimensional phononic crystals based on the finite element method and genetic algorithm, *Struct. Multidiscip. Optim.* 50 (2014) 593-604.
- [81] P.S. Ma, H.J. Lee, Y.Y. Kim, Dispersion suppression of guided elastic waves by anisotropic metamaterial, *J. Acoust. Soc. Am.* 138 (2015) EL77.
- [82] M.P. Bendsøe, O. Sigmund, *Topology optimization: theory, methods and applications* (Springer, 2003).
- [83] M.P. Bendsøe, N. Olhoff, J.E. Taylor, A Variational Formulation for Multicriteria Structural Optimization, *J. Struct. Mech.* 11 (1983) 523-544.
- [84] K. Svanberg, The method of moving asymptotes - a new method for structural optimization, *Int. J. Numer. Methods Eng.* 24 (1987) 359-373.
- [85] C.W. Neff, T. Yamashita, C.J. Summers, Observation of Brillouin zone folding in photonic crystal slab waveguides possessing a superlattice pattern, *Appl. Phys. Lett.* 90 (2007) 021102.
- [86] W. Ku, T. Berlijn, C.C. Lee, Unfolding first-principles band structures, *Phys. Rev. Lett.* 104 (2010) 216401.

ABSTRACT (KOREAN)

비등방성 메타물질을 이용한 탄성과

원추 굴절

안 영 관

서울대학교 대학원

기계항공공학부

원추 굴절(Conical refraction)은 2축성 결정(biaxial crystal) 성질의 특별한 비등방성 물질에서만 나타날 수 있는 파동의 진행방향을 획기적으로 조절할 수 있는 현상이다. 전자기 및 광학 분야의 장비에서 유용하게 사용될 수 있는 개념이지만, 탄성 구조체를 따라 전파하는 진동파를 다루는 초음파 분야에서는 그 연구가 미진할 뿐만 아니라 그 활용방안 역시 찾지 못하고 있는 실정이다.

여기에서 우리는 원추 굴절 성질을 지니는 탄성 메타물질 평판을 최초로 제안하여, 기계적 파동(mechanical wave)이 마치 그 전파하는 과정에 있어서 공간이동 되는 것과 같이, 파동의 공간상의 전파위치를 옮겨주는 탄성 메타물질을 실체화하였다. 공학적으로 설계된 메타물질은

탄성과동을 공간이동 시키는데 있어 매우 혁신적이다. 제안된 메타물질은 근래 산업에서 가장 중요하게 활용되는 물질인 알루미늄을 기저(base)로 하여 슬릿 slit)들이 삽입된 다공성 구조 형태로 구성되어 매우 제작가능성이 높다. 본 연구에서 우리는 수치적 시뮬레이션과 실험을 통해 메타물질의 작동성능을 완벽하게 검증하였을 뿐만 아니라, 메타물질의 단위구조(unit cell)를 비공진 구조(non-resonant structure)로 구성하여 광대역의 작동주파수 대역을 가지도록 설계하였다. 더불어 파동이 메타물질을 따라 전파할 때 원추 굴절에 의해 두 가지의 진행 경로를 가질 수 있는데, 이들 중 오직 한 방향으로만 선택적으로 파동을 전달하는 방법 역시 설명하고 검증하였다. 또한 위상최적설계 기법(topology optimization)을 사용하여 다양한 편향 각도(deflection angle)를 갖는 메타물질의 단위구조를 새롭게 설계하였다. 최적설계된 구조를 이용하면, 메타물질의 작동성능이 방향 조정성(directional tunability) 측면에서 향상될 수 있다. 우리는 본 연구에서 제안한 메타물질 시스템을 비파괴 검사(non-destructive testing), 초음파 이미징(ultrasound imaging) 분야와 더불어, 새로운 방식의 클로킹(cloaking)으로 응용할 수 있을 것으로 기대하고 있다.

주요어: 메타물질, 원추 굴절, 비등방성, 탄성파, 위상최적설계

학번: 2010-20692

ACKNOWLEDGEMENTS

This research was supported by the National Research Foundation of Korea (NRF) grant No. 2014M3A6B3063711, No. 2015021967 and No. 2015049675 funded by the Korean Ministry of Science, ICT & Future Planning and contracted through the Institute of Advanced Machinery and Design at the Seoul National University.